Development of Cobalt-Doped Nickel Hydroxide Sol-Gel Catalysts for Enhanced Electro-Oxidation of Urea

by

Stephen William Tatarchuk

A thesis

presented to the University of Waterloo

in fulfillment of the

thesis requirement for the degree of

Master of Science

in

Chemistry

Waterloo, Ontario, Canada, 2021

Author's Declaration

This thesis consists of material all of which I authored or co-authored: see Statement of Contributions included in the thesis. This is a true copy of the thesis, including any required final revisions, as accepted by my examiners.

I understand that my thesis may be made electronically available to the public.

Statement of contributions

This thesis is based on the original article that has been published in a peer-reviewed journal.

Scientific Journal: Chemosphere

Article Title: Inductive Effects in Cobalt-Doped Nickel Hydroxide Electronic Structure Facilitating Urea Electrooxidation

Authors: Stephen W. Tatarchuk, Rachelle M. Choueiri, Xenia V. Medvedeva, Leanne D. Chen, and Anna Klinkova

Citation: Chemosphere 279, 2021, 130550.

This manuscript was written by Stephen W. Tatarchuk with critical comments and revisions by Dr. Anna Klinkova and corresponding collaborators. The research contributions of Stephen W. Tatarchuk to this project included original ideas, designing and carrying out all the experiments, performing computational studies, data analysis, data visualization, and data interpretation. The research contributions of Stephen W. Tatarchuk to this project included original ideas, designing and carrying out all the experiments, performing computational studies, data analysis, data visualization, and data interpretation. The additional content in Chapters 1 and 2 not included in this manuscript was written by Stephen William Tatarchuk under the supervision of Dr. Anna Klinkova.

Abstract

Electrochemical oxidation of urea provides an approach to prevent excess urea emissions into the environment while generating value by capturing chemical energy from waste. Unfortunately, the source of high catalytic activity in state-of-the-art doped nickel catalysts for urea oxidation reaction (UOR) activity remains poorly understood, hindering the rational design of new catalyst materials. In particular, the exact role of cobalt as a dopant in $Ni(OH)_2$ to maximize the intrinsic activity towards UOR remains unclear. This thesis explores how tuning the Ni:Co ratio in a modified propylene oxide synthesis of $Ni_{1-x}Co_x(OH)_2$ xerogel catalysts alters both structural and electronic states which allows one to tune the number and intrinsic activity of redox-active surface sites towards UOR. For the $Ni_{1-x}Co_x(OH)_2$ catalysts studied, $Ni_{90}Co_{10}(OH)_2$ achieves the largest geometric current density due to the increase of available surface sites and that intrinsic activity towards UOR is maximized with $Ni_{20}Co_{80}(OH)_2$. Through density functional theory calculations, we show that the introduction of Co alters the Ni 3d electronic state density distribution to lower the minimum energy required to oxidize Ni and influence potential surface adsorbate interactions.

Acknowledgements

I would like to thank my supervisor Prof. Anna Klinkova for her guidance, support, and patience throughout my M.Sc. program. She gave me the opportunity to explore and learn a wide set of skills, which helped me determine what type of career I want to pursue.

I would like to thank my Committee member Prof. Leanne D. Chen and Prof. Rodney Smith for their guidance, advice, and productive conversations during my M.Sc. program. In particular, I would like to thank Prof. Leanne D. Chen for teaching me how to perform and interpret density functional theory calculations that were used in this thesis. I would like to thank Prof. Rodney Smith for his advice related to solid-state material characterization, electrochemistry of layered hydroxide electrodes, and performing Raman spectroscopy measurements that appear in this thesis.

I would like to thank Dr. Jury Medvedev for the time he spent training me how to perform electrochemical experiments, providing advice about making figures more visible, proofreading, providing constructive criticism of my ideas, helping me troubleshoot experimental problems, and moral support during difficult times. I would like to thank Dr. Rachelle Choueiri for the time she spent proofreading, troubleshooting experimental problems, helping me drastically improve the quality of my writing, productive conversations about computational modelling, providing moral support and her contribution towards the manuscript that was adapted in this thesis. I would like to thank Xenia Medvedeva for the time she spent providing experimental insight, providing advice about making figures more visible, proofreading, providing constructive criticism of my ideas, helping me troubleshoot experimental problems, providing moral support

during difficult times, and her contribution towards the manuscript that was adapted in this thesis. I would like to thank Feng Li for his constant encouragement and support throughout my M.Sc. program in addition to his help training me how to use access and use the Compute Canada supercomputer Cluster. and his continued encouragement throughout my program. In addition, I would like to thank any unmentioned current and past members of the Klinkova lab for being a great group of people to work with. I would also like to thank the members of the Smith lab for their help and advice throughout my M.Sc. program.

I would like to give a huge thanks to my life partner, Raven Boulet for all of her consistent support, encouragement, patience, and understanding when my workloads became quite high. I would also like to thank my family and friends for the support and encouragement throughout my M.Sc. program. In particular, I would like to thank my mother (Alayna Tatarchuk) and father (Andrew Tatarchuk) for their support and guidance leading up to and during my M.Sc. program.

Finally, would like to thank Prof. Linda Nazar at the University of Waterloo for providing access to X-ray diffraction instrumentation, Prof. Brian Kendall and Sarah McCaugherty in the Metal Isotope Geochemistry Laboratory at the University of Waterloo for performing ICP-MS analysis, Peter Brodersen at the Ontario Center for the Characterization of Advanced Materials (OCCAM) for performing X-ray photoelectron spectroscopy analysis, Jason Tam and Mengsha Li at OCCAM for HR-STEM imaging, Ilya Gourevich at the Centre for Nanostructure Imaging for performing SEM-EDX imaging, and Compute Canada for generously providing supercomputing resources.

Table of Contents

List of Figures

List of Tables

List of abbreviations

CDD	Charge density difference
CIF	Crystallographic information file
CIREALS	Complete integration method in real space
CV	Cyclic voltammetry
DFT	Density functional theory
DOS	Density of state
ECSA	Electrochemically active surface area
EDX	Energy-dispersive X-ray spectroscopy
FTIR	Fourier-transform infrared spectroscopy
GCD	Geometric current density
GGA+U	Generalized gradient approximation with Hubbard correction potential
ICP-MS	Inductively coupled plasma mass spectrometry
OER	Oxygen evolution reaction
PBE	Perdew-Burke-Ernzerhof
PDOS	Projected density of states
PO	Propylene oxide
PTFE	Polytetrafluoroethylene
PXRD	Powder X-ray diffraction
RASS	Redox-active surface sites
RHE	Reversible hydrogen electrode
SEM	Scanning electron microscopy
SHE	Standard hydrogen electrode
TEM	Transmission electron microscopy
U	Hubbard potential
UOR	Urea oxidation reaction
UV-Vis	Ultraviolet-visible spectroscopy
VASP	Vienna Abinitio Simulation Package
XRD	X-ray diffraction

Chapter 1

Background

1.1 Introduction

The ever-growing human population is closely connected to the increasing agricultural demands to produce nitrogen-based fertilizers that use either urea, ammonia/ammonium, or nitrate.[1,2] In particular, urea makes up ∼60% of the nitrogen-enriched fertilizer used worldwide since it is highly stable as a solid, less explosive than other N-sources, and can be produced on industrial scales cheaply.[1–3] As a result, the agricultural runoff from fields using these fertilizers remains one of the largest pathways through which nitrogen-containing wastewater is released to the environment.[4] In addition, the process itself of producing urea-based fertilizers generates large amounts of wastewater enriched with urea which requires downstream purification.[3] If left untreated, these nitrogenous pollutants decompose into nitrogen oxides which play a major role in causing respiratory diseases, cancer (via ozone

production), acid rain, and smog.[5–8] Urea decomposition results in the additional hazard of producing cyanate salts, which even at low concentrations make water unsuitable for human consumption.[9,10] An indirect impact on human society is that increasing concentrations of urea and ammonia in aquatic environments enhance cyanobacteria algae blooms, which lead to the destruction of fragile ecosystems.[1,11,12] Inevitably, as our population continues to grow, the demand to develop a more economical and sustainable nitrogenous wastewater treatment process becomes more pressing.

Traditional wastewater treatment methods to remove urea such as high pressure-temperature hydrolysis, biological decomposition, and decomposition by strong oxidants, provide sustainable solutions for closing the nitrogen cycle, but fail to extract value from this energy-rich compound.[13] Electrochemical oxidation of urea is an attractive candidate to complement or even replace current urea-removal methods as it enables the capture of the chemical energy stored in the bonds of urea and is facilitated by inexpensive catalyst materials.[14–19] In this regard, urea oxidation reaction (UOR) continues to attract considerable attention as an alternative to direct water oxidation as an anodic reaction in the electrochemical generation of hydrogen and CO_2 electrolysis to value-added products because of the lower voltage required to drive the reaction as well as the aforementioned abundance of environment-polluting urea available in wastewater streams.[20–23]

1.2 Electrooxidation of Urea

The first approach of electrochemical strategy for urea oxidation reaction (UOR) was the electrochemical generation of highly reactive chemical Cl radials *in-situ*, which spontaneously oxidize urea into smaller molecules.[24,25] These methods require high applied potentials (>1.34V vs standard hydrogen electrode (SHE)) to produce non-toxic products CO_2 and N_2 and produced toxic by-products (chlorinated amines and carbon monoxide).[24,25] Thus, this approach may not be a viable alternative for treating urea wastewater. Furthermore, one must be aware of it as a potential competing reaction if Cl^- is present for the other electrochemical approaches discussed below.

In the absence of Cl^-, electrochemically generated OH^- radicals would oxidize urea into non-toxic products via half-cell reaction (1.1).[13] In particular, Pt electrodes have been studied extensively due to their traditional role in electrochemistry.[13] Unfortunately, only at low currents at voltages between 0.75-0.9 V vs the reversible hydrogen electrode (RHE) the only observed products observed are N_2 and CO_2.[26] Above 0.9 V vs RHE, other products (NO, NO_2, N_2O, $NO_3^-[N_2O_2]^{2-}$, CNO^-, and CO) have been observed for UOR on Pt by on-line mass spectroscopy and *in-situ* Fourier transform infrared spectroscopy (FTIR).[26,27] Unfortunately, no follow-up studies were conducted to further investigate the mechanistic pathways required to produce the above by-products from urea on Pt. While other electrode materials (such as boron-doped diamonds, Ti, BiO_x, and IrO_2) have been explored for UOR, Ni-based materials were pursued to the largest extent due to the enzymatic role of Ni atoms in urease to decompose urea in nature.[13,18]

$$CO(NH_2)_2(aq) + 6OH^-(aq) \rightarrow N_2(g) + 5H_2O(l) + CO_2(g) + 6e^- \quad (1.1)$$

Thus far, Ni(II-IV)-based materials such as oxides, hydroxides, sulfides, and others have shown the best catalytic performance towards UOR compared to other Ni-based materials due to the *in-situ* generation of reactive nickel sites that act as oxidants towards urea as seen in Figure 1.1 below.[14,28–30] However, the activity of these materials is known to degrade over time due to the generation of carbonate at the surface throughout a reaction.[31–33] To reduce changes in the surface and further improve the intrinsic activity of the catalyst towards UOR, researchers have begun to investigate the performance of binary and ternary multimetal electrocatalysts, with a particular interest in Ni hydroxide based structures.[16–19] The next section will examine current trends in UOR electrocatalysts in the literature which aim at addressing the above issues.

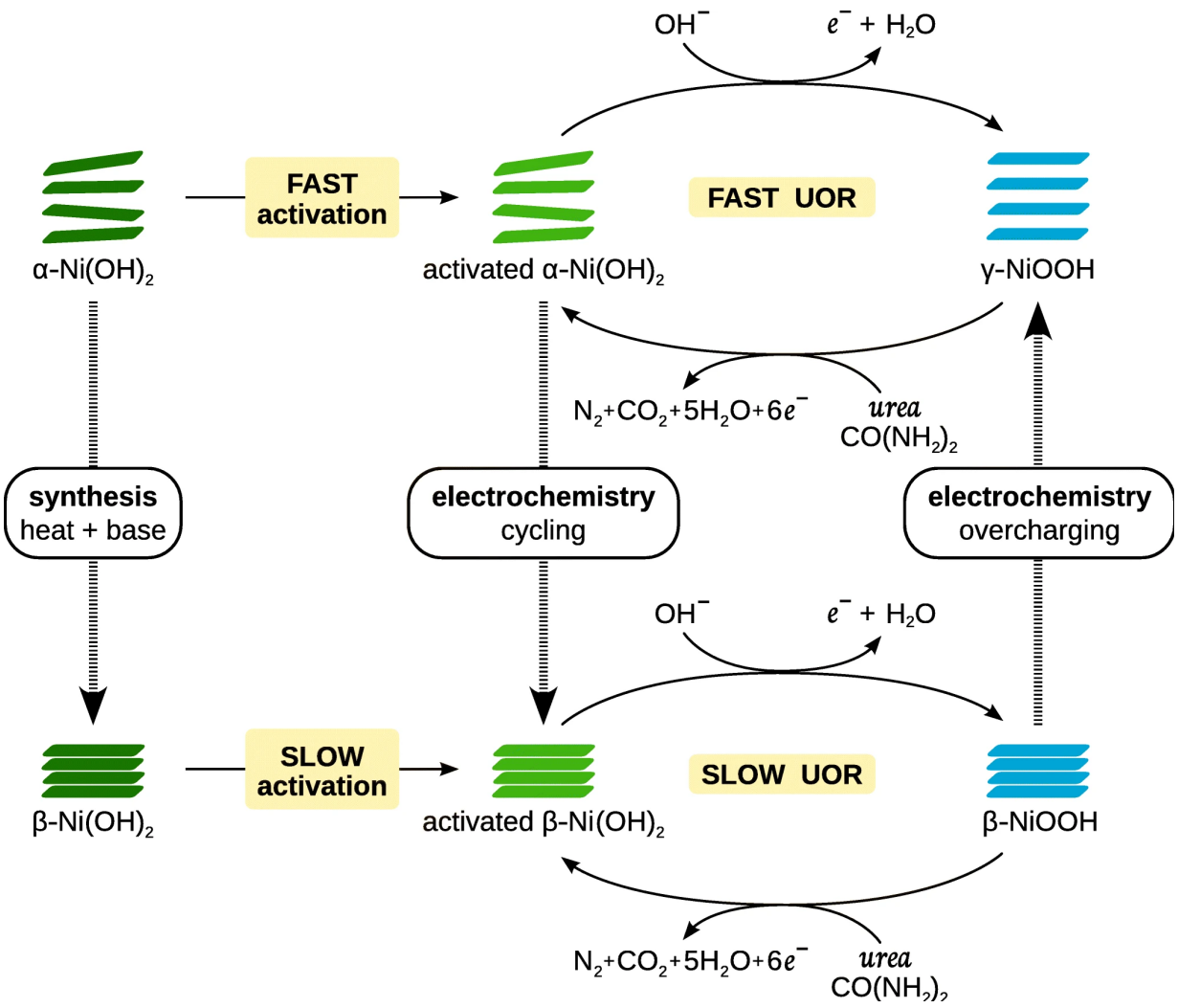

Figure 1.1: The Bode-Botte scheme of $Ni(OH)_2$/NiOOH phase transitions during activation, cycling, and UOR. Reproduced from ref. [30] with permission.

1.3 Strategies to Increase Intrinsic Activity and Stability

While a plethora of empirical evidence demonstrates that combining Ni with other transition metals can lead to improved catalytic activity and stability under UOR conditions, not all reported Ni-based catalysts have an equal UOR performance or stability.[13–19] This variation is largely caused by how the structural, chemical, and electronic properties of a catalyst change with the introduction of certain dopants.[14,19] While, a number of other factors can influence the catalyst activity and stability (e.g. temperature modulation, use of electrolyte additives, electrode preparation, and the use of nanostructured catalysts to increase surface area), the greatest influence is caused by the material composition (Table A.1, A.2, and A.3).[13–19] Thus, increasing our understanding of how metal dopants change Ni-based catalysts for UOR is an attractive way to improve the affordability and sustainability of removing nitrogenous contaminants from water.[17,34–36]

Among the binary transition metal catalysts studied for UOR, mixtures of Ni and Co with non-zero valences have attracted attention due to their increased current densities, reduced onset potentials, and prolonged stability relative to other Ni(*II*, *III*, and *IV*) based systems mixed with a secondary metal.[18,19,37,38] While the optimal composition in $Ni_{1-x}Co_x(OH)_2$ catalysts is reported as $Ni_{90}Co_{10}(OH)_2$ or $Ni_{80}Co_{20}(OH)_2$ depending on compositions studied, the nature of the enhancement and the cause for its maximization between 10-20% Co incorporation still remains unclear (see Table A.2 in appendix A for a literature summary of $Ni_{1-x}Co_x(OH)_2$ based catalysts for UOR). Several studies have concluded that increasing electrical conductivity due to Co incorporation or changes in the

electrochemically active surface area (ECSA) are not the origin of enhanced UOR.[39–41] In addition, it is known that adding Co can increase the number of Ni(IV) surface sites (postulated to be the most active toward UOR).[22,42,43] The number of Ni(IV) sites is expected to be maximized with a Co incorporation for either $Ni_{60}Co_{40}(OH)_2$ or $Ni_{50}Co_{50}(OH)_2$, which conflicts with the trend discussed above for the best performing $Ni_{1-x}Co_x(OH)_2$ UOR catalyst.[38,41–43] Thus, the origin of UOR enhancement is thought to be caused by Co-induced changes to the electronic structure of Ni however, more in-depth studies are needed to verify this hypothesis.[44–46]

1.4 *Ab Initio* Prediction of Electrooxidation Catalyst Performance

Density functional theory (DFT) is a method used in computational chemistry to calculate properties of atoms, molecules, and solid-state structures from first principles based on quantum mechanics. Thus far, there has been a limited number of UOR or UOR related DFT calculations published in the literature. The following section will highlight key examples from the literature to highlight how DFT calculation has led to further insights on UOR with Ni-based catalyst.

The first density functional theory (DFT) calculations on UOR were performed to calculate the free energies for three proposed mechanistic pathways for UOR on a single NiOOH center.[47] While many of the assumptions such as using a single molecule to represent the surface of a solid-state material will lead to inaccuracies in the predicted thermodynamic values, this work successfully predicted that the desorption of CO_2 was the rate-limiting step for UOR on NiOOH.[47] The same finding was reproduced nearly 10 years later using a periodic supercell of NiOOH crystal lattice using a more sophisticated calculation framework (as seen in Figure 1.2).[22] Here, the mechanistic pathway was elaborated further by considering two possible surface sites that may exist during the reaction (NiOOH and deprotonated NiOOH denoted as NiOO).[22] The authors of this work showed that both surfaces will stabilize different reaction intermediates reaction addition to having a different overall net free energy required to oxidize urea into N_2, CO_2, and H_2O.[22] These results suggest that the UOR reaction pathway will have a lower net free energy on NiOO surface sites compared to the NiOOH surface sites due to the transfer

of a lattice oxygen atom from the NiOO surface to for CO_2 before the N_2 desorption step. These calculations were validated experimentally with Ni^{3+} (NiOOH rich) and Ni^{4+} (NiOO rich) $Ni(OH)_2$ catalysts derived from different synthetic methods to evaluate the percentage of lattice oxygen atoms that were exchanged during UOR in $H_2^{18}O$ electrolytes by secondary-ion mass spectrometry. The observed electrochemical response between the two materials showed that the surface with a higher percent of exchanged lattice oxygen atoms achieves higher current densities for UOR than the surface with less lattice oxygen exchange. Furthermore, *in-situ* FTIR measurements during UOR at 1.35V vs RHE showed the accumulation of C=O vibrations belonging to the adsorbed CO for the NiOOH rich catalyst, while the NiOO rich catalyst did not show this vibration. Thus, through computational modelling, the authors not only predicted which of the two surfaces studied will have a higher catalytic activity towards UOR, but could predict the underlying cause of this observation which was in agreement with experiments.

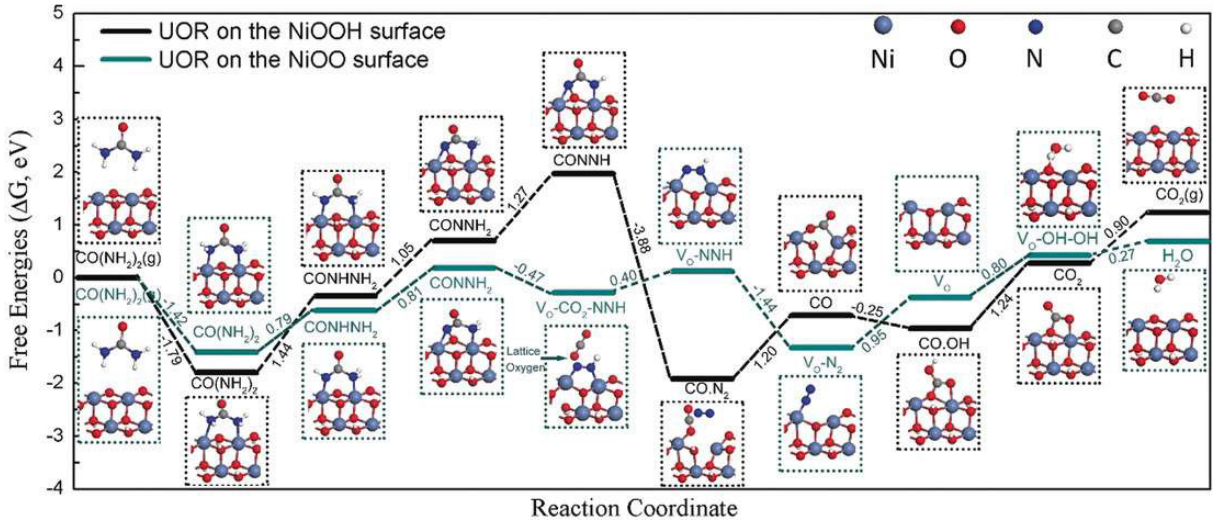

Figure 1.2: The Gibbs free energy (ΔG) profiles calculated at the standard conditions and the simplified surface structures of the various reaction species along the reaction pathways of UOR on the NiOO and NiOOH surfaces. Reproduced from ref. [22] with permission.

Aside from examining different surfaces that may exist on $Ni(OH)_2$ catalyst during UOR, one can apply DFT calculations to understand the role of other transition metals in Ni-based catalysts towards improved intrinsic activity and stability. For example, Ni-Mo oxide catalysts were demonstrated experimentally to achieve high current densities due to the presence of oxygen vacancies.[48] To understand how oxygen vacancies influence the UOR process, the authors performed DFT calculations on the density of states (DOS) and urea adsorption energy calculations. Figure 1.3a shows the adsorption energy for urea was reduced at an oxygen vacancy site, suggesting that oxygen vacancies stabilize urea as opposed to the pristine surface. Figure 1.3b-c contrasts the change electronic states of the Ni-Mo oxide catalyst in the presence of oxygen vacancy. These results show a downward shift of the Ni, Mo, and O states an oxygen vacancy-rich catalysts which the authors

indicate would cause a higher charge carrier density and conductivity which could increase Faradaic currents towards UOR. Furthermore, the downshift in these states could be the source of improved urea adsorption observed in Figure 1.3a, but further calculations would be required to validate this hypothesis. This work demonstrates how DFT can be applied to help one better understand the origin of increased intrinsic activity in transition metal modified Ni-based catalyst structures.

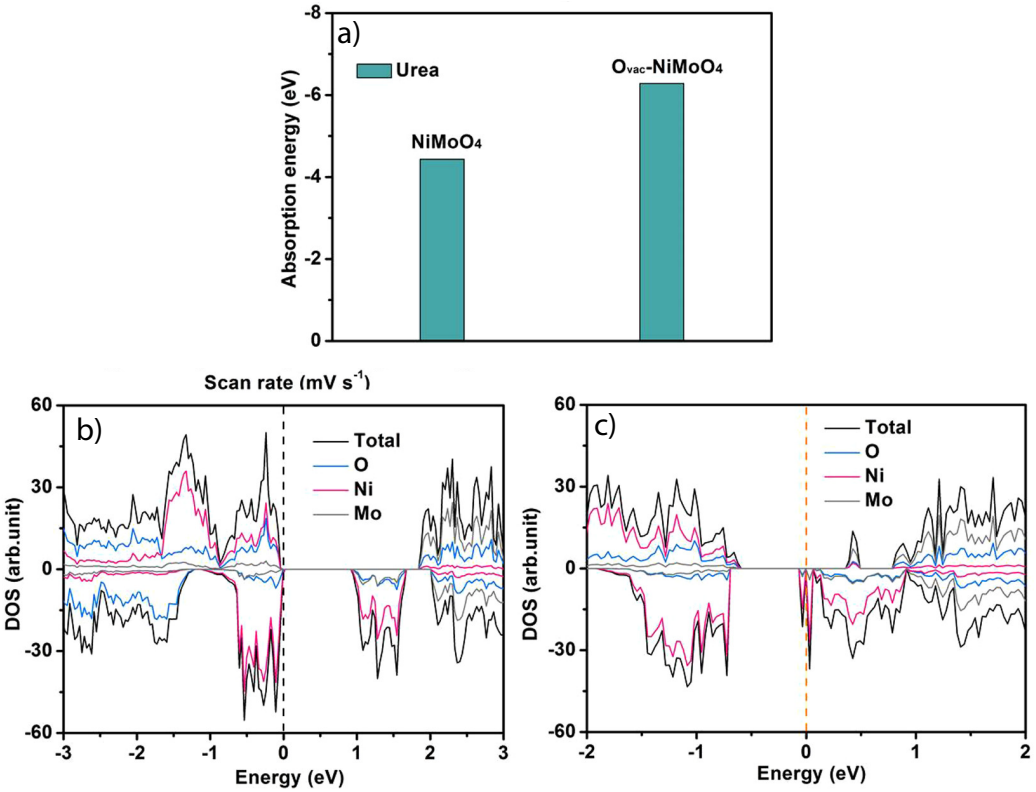

Figure 1.3: a) Adsorption energy of urea molecules on the p-$NiMoO_4$ and r-$NiMoO_4$ samples. Calculated density of states (DOS) of b) pristine $NiMoO_4$ and c) oxygen-defect $NiMoO_4$ samples. Figure adapted from ref. [48] with permission.

1.5 Scope of Thesis

This thesis describes a rational dopant selection process for UOR catalyst design for electrochemical wastewater treatment by investigating how the electrochemical, electronic, and structural properties of $Ni_{1-x}Co_x(OH)_2$ change with increasing Co fractions to understand the origin of increased catalytic activity at specific compositions. **Chapter 1** provided the motivation of this thesis. **Chapter 2** describes the experimental and theoretical methods used in the following chapters. **Chapter 3** focuses on the characterization of sol-gel derived cobalt-nickel xerogel catalysts. **Chapter 4** reports the evaluation of UOR performance for the catalysts described in the previous chapter. **Chapter 5** discusses *ab initio* modeling of cobalt doped nickel hydroxide electronic structure in the context of the electrochemical results presented in chapter 5.

Chapter 2

Methodology

2.1 Synthesis

2.1.1 Synthesis of $Ni_{1-x}Co_x(OH)_{2-y}Cl_y$

The synthesis of $Ni_{1-x}Co_x(OH)_{2-y}Cl_y$ was adapted from elsewhere with modifications to improve reaction mixing and temperature control.[29,49] To begin, a total of 0.9 mmol of $Ni(II)Cl_2{\cdot}6H_2O$ (Sigma; 99.9% trace metals basis) and $Co(II)Cl_2{\cdot}6H_2O$ (Sigma; 98% ACS Grade) was added to centrifuge tubes and dissolved in 4.0 mL absolute ethanol (>99.9% ACS grade). The tubes were then sonicated for <10 s to ensure a homogenous distribution of metal ions was achieved followed by the fast addition of 1.4 mL of propylene oxide (Sigma; 99.5% GC basis) (PO). Immediately after PO addition, the tubes were capped and sealed with parafilm, then shaken using an Eppendorf Thermomixer C at 30°C at 450 RPM for 24 hours. Afterwards, each tube was filled with ∼11 mL anhydrous acetone

(Sigma; 99.9% HPLC Grade), then decanted to remove the supernatant which contained the majority of unreacted precursors. The tubes were then filled with anhydrous acetone and allowed to sit for 24 hours to undergo solvent exchange from the pores of the gel. After 24 hours, the supernatant was decanted and replaced; this process was repeated three more times for a total of five solvent exchange cycles. After the final solvent exchange, the tubes were decanted and dried using a rotary evaporator at 30°C under a vacuum of ∼730 mm Hg for 8 hours to form a xerogel. The xerogels were then ground into a powder and placed under vacuum at 25°C for 60 hours to remove residual solvent.

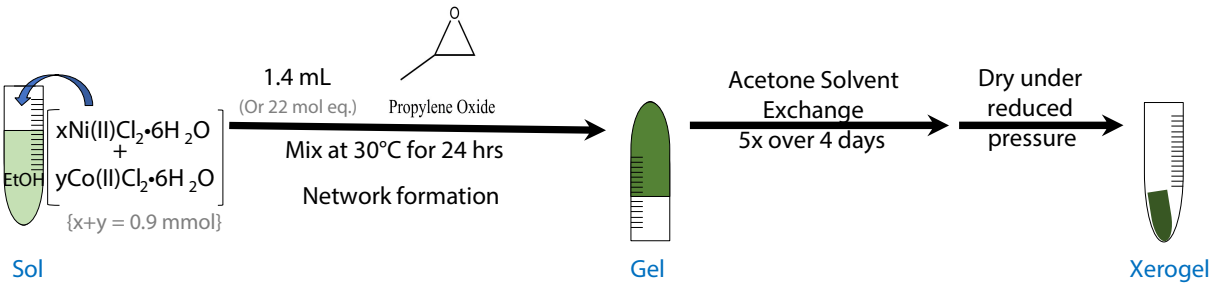

Figure 2.1: Scheme of sol-gel synthesis.

2.2 Catalyst Characterization

2.2.1 ICP-MS Measurements

Powdered catalysts (29-30 mg) were digested in 20 mL 2% HNO_3 for 72 hours in glass scintillation vials. Two successive 10x dilutions were then performed to get a final total Co+Ni concentration of approximately 100 ppm. Samples were submitted to the Metal Isotope Geochemistry Laboratory in the Earth Science department at the University of Waterloo for inductively coupled plasma mass spectrometry (ICP-MS) measurements. Class A volumetric glassware was used for preparing solutions used in this analysis. A 200 μL autopipette was calibrated and used for diluting the digestate. All glassware and pipette tips were soaked in 2% HNO_3 prior to rinsing with MilliQ water before use.

2.2.2 SEM-EDX sample measurements

Catalyst inks were made by mixing 2 mg of catalyst material with 1 mg Vulcan Carbon Black (FuelCellStore), 400 μL absolute ethanol (>99.9% ACS grade) and 100 μL MilliQ water (18.2 Ω). Ink mixtures were sonicated for 1 hour after which the catalyst ink was drop cast onto Toray 60 Carbon paper (FuelCellStore); that volume of ink deposited was adjusted to get 0.226 mg cm^{-2} on each sample. Energy-dispersive X-ray spectroscopy (EDX) analysis including elemental mapping was performed on FEI Quanta FEG 250 environmental scanning electron microscope (SEM).

2.2.3 SEM and TEM sample imaging

For high magnification imaging, catalyst inks were made by mixing catalysts with MilliQ water in a 4:3 (mg:mL) ratio and sonicated for 10 minutes. Ink droplets were dropcast onto Cu/C transmission electron microscopy (TEM) grids and imaged on a Hitachi HF3300 microscope. Low magnification imaging was performed using an FEI Quanta FEG 250 environmental SEM.

2.2.4 PXRD sample preparation

Powder X-ray diffraction (PXRD) measurements were conducted at room temperature on a PANalytical Empyrean diffractometer with Cu-Kα radiation equipped with a PIXcel bidimensional detector. Powdered samples were measured on a zero-background substrate using a Bragg-Brentano geometry. Phase pattern simulations were done by modifying the c axis of crystallographic information files (CIFs) (β-$Ni(OH)_2$: ICSD-161894, β-$Co(OH)_2$: ICSD-26763) to match the experimental interlamellar spacing. The modified CIFs were used in the complete integration method in real space (CIREALS) method described elsewhere reproduced the experimental peak positions and relative order of intensity for both pure Ni and Co phases.[50]

2.2.5 UV-Vis measurements

The absorbance spectra of powdered catalyst samples were measured by reflectance UV-Vis using a R200-Angle Ocean Optics Reflection probe at a distance of $\sim$3 cm with

a deuterium-halogen light source (DH-2000-BAL) and Ocean Optics Flame Miniature Spectrometer. The background reflectance spectrum for all measurements was taken from a polished slab of polytetrafluoroethylene (PTFE).

2.2.6 Raman Spectroscopy Measurements

Raman spectroscopy was conducted with a Renishaw inVia Raman microscope. All spectra were acquired using a 532 nm laser filtered to 10% laser power with neutral density filters. Each spectrum had an acquisition time of 300 seconds, except 100% Co which required 150 seconds due to laser damage. Spectra were analyzed in Renishaw WiRE V5.3 software to perform polynomial baseline subtractions and curve fitting.

2.2.7 X-ray photoelectron measurements

X-ray photoelectron spectroscopy (XPS) was performed using the ThermoFisher Scientific K-Alpha X-ray photoelectron spectrometer. Samples were prepared by activating anodes as described below, followed by immediately rinsing with MilliQ water and drying under a stream of Ar. The as-prepared samples were stored under Ar prior to the analysis.

2.3 Electrochemical Assessment

2.3.1 Anode Preparation

Catalyst inks were made by mixing 2 mg of catalyst material with 1 mg Vulcan Carbon Black (FuelCellStore) then adding 390 μL absolute ethanol (99.9% ACS grade) and 100 μL MilliQ water (18.2 Ω). The mixture was sonicated briefly (<3 s) to disperse the powder in the solvent, before the addition of 10 μL of Nafion D-520 dispersion (Alfa Aesar; 42118). Ink mixtures were sonicated for 1 hour, after which five layers of catalysts ink was drop cast onto a 0.58$\pm$0.04 cm^2 piece of Toray 60 Carbon paper (FuelCellStore) such that the total volume of ink deposited was adjusted to get 0.226 mg cm^{-2} on each anode.

2.3.2 Evaluation of UOR activity

The activity of catalysts towards UOR was evaluated in 1 M aqueous KOH (Sigma; 85% ACS Grade) electrolyte containing 0.33 M urea (Sigma; 99.5% ReagentPlus) in deionized water (18.2 Ω). The electrolyte was purged with Ar prior to use. All electrochemical measurements took place in an undivided three-electrode cell with a double junction Ag/AgCl (3.5 M KCl) reference electrode and Pt mesh counter electrode. Catalysts were first activated in 50 mL 1 M KOH by cyclic voltammetry (CV) cycles scanning from -0.4 to 0.8 V vs Ag/AgCl at 100 mV/s for 50 scans using a potentiostat (Biologic SP-300). This was followed by CV cycles within the same range at 20 mV/s for 20 scans to achieve a steady state. CV was used to assess the activity differences between activated catalysts with different Ni:Co ratios in 50 mL 1 M KOH and 50 mL 1 M KOH + 0.33 M urea by

scanning from -0.4 to 0.8 V vs Ag/AgCl at 20 mV/s for 10 scans. Potentials were converted to V vs RHE using equation (2.1) below and assuming that the bulk pH was the same as the local pH at the electrode.

$$E_{RHE} = E_{Ag/AgCl,3.5MKCl} + 0.059pH + E^{\circ}{}_{Ag/AgCl,3.5MKCl} \tag{2.1}$$

2.3.3 Current density normalization

Current densities were normalized by both the geometric surface area of the catalyst film and the number of redox-active surface sites (RASS). The RASS was determined by performing a linear integration of a baseline subtracted current in the redox-active region. The Butler-Volmer equation (2.2) was used to fit the raw current data between 1.23-1.64 V vs RHE to subtract the theoretical oxygen evolution reaction (OER) current from the redox-active region.[51]

$$i = i_{\circ}\left(exp\left(\frac{(1-\alpha)\,zF\eta}{RT}\right) - exp\left(\frac{\alpha zF\eta}{RT}\right)\right) \tag{2.2}$$

Where i is the observed current, $i_{\circ}$ is the exchange current, α is the charge transfer coefficient, z is the number of electrons transferred, η is the overpotential, R is the universal gas constant, F is Faraday's constant, and T is temperature. The remaining OER current (1.64-1.831 V vs RHE) were then fitted to 9^{th} order polynomials to construct a baseline. The raw current was then subtracted from the fitted baseline in the corresponding potential region (Figure 2.2).

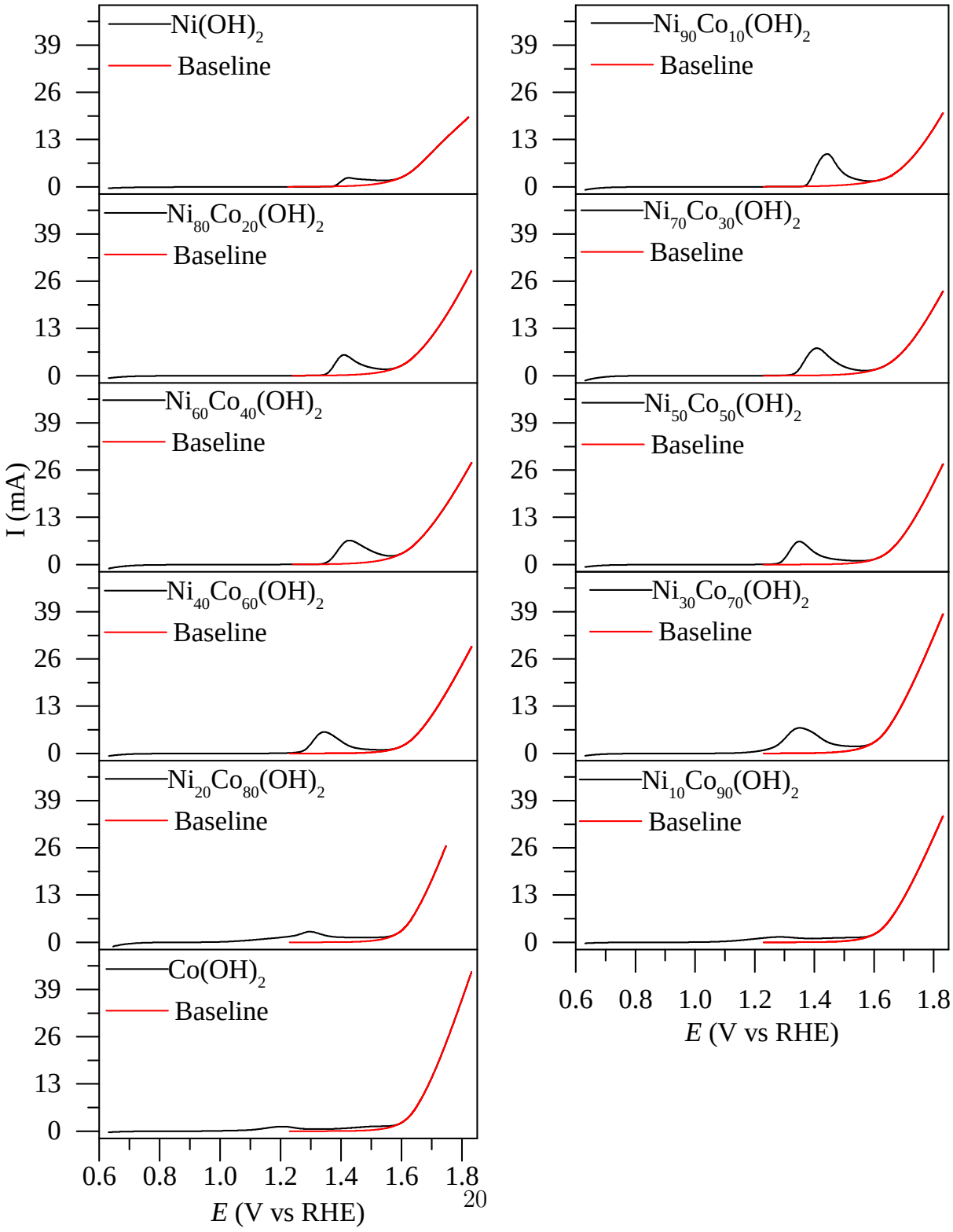

Figure 2.2: Fitted baselines with raw currents (mA) for $Ni_{1-x}Co_x(OH)_2$ catalysts.

2.3.4 Determination of Number of Redox-Active Sites Assumptions

To convert the charge from the integrated redox region into the number of RASS, the entire region was assumed to be associated with a $1e^-$ transfer process, as reported recently in work by Anantharaj et al.[52] One should note that Co is redox-active in a similar region as Ni and can potentially act as an active site for OER. In addition to Co having an inductive effect on neighbouring Ni sites, Ni could also have an inductive effect of the Co sites shifting the Co redox potentials to more positive values, thereby making any attempt of deconvoluting the true Ni and Co redox peaks with confidence difficult. The intrinsic activity of each composition was normalized by combining two classical electrochemistry approaches that were described recently in the context of doped $Ni(OH)_2$ materials.[51,52] First, baselines were constructed to capture the capacitance current and OER current by combining a polynomial fit with the Butler-Volmer equation such that, once subtracted from the raw current, the remainder only shows the faradaic current related to Ni and Co redox reactions seen in reactions (2.3), (2.4), and (2.5). Since a redox peak for Co(III) to Co(IV) was observed in Figure 2.2, we examined how increasing the total number of electrons transferred gradually from 1 to 2 based on the Ni:Co ratio to see how it would alter the data (Figure 2.3). Here, it is clear that the overall trend in the data is not altered by changing the number of electrons transferred. It is important to note here that the scaling relationship will overestimate the number of electrons transferred at low Co concentrations since the literature suggests that Co in $Ni(OH)_2$ is redox inactive at low concentrations.[43]

$$Ni(OH)_2 + OH^- \rightarrow NiOOH + H_2O + e^- \tag{2.3}$$

$$Co(OH)_2 + OH^- \rightarrow CoOOH + H_2O + e^- \tag{2.4}$$

$$CoOOH + OH^- \rightarrow CoO_2 + H_2O + e^- \tag{2.5}$$

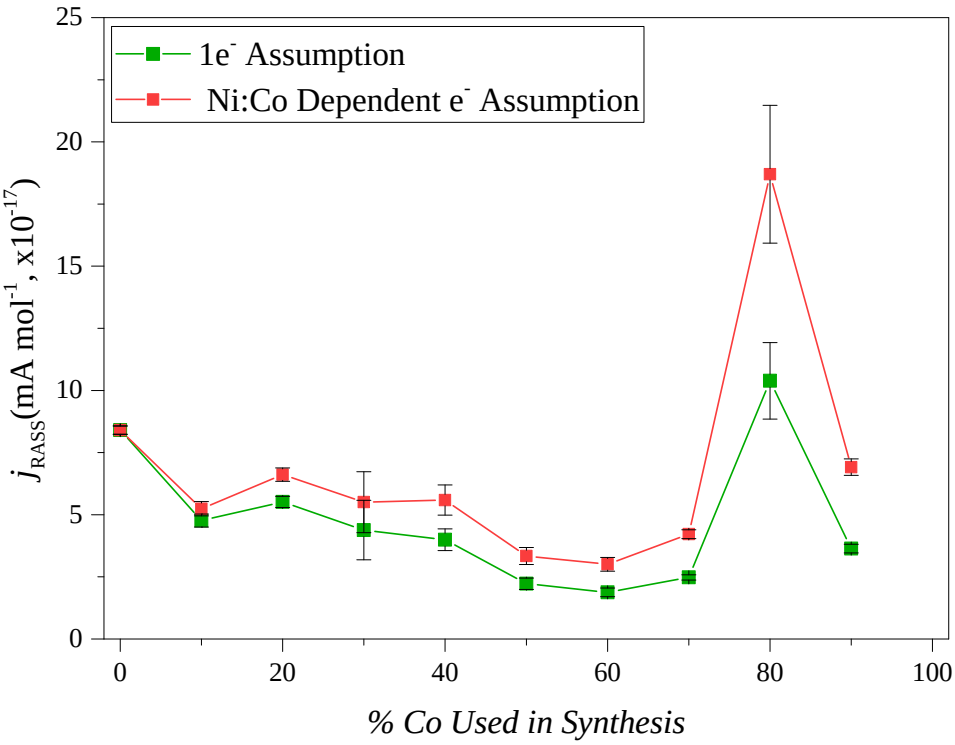

Figure 2.3: Change in maximum current density per number of RASS of UOR peak with increasing Co concentration in $Ni_{1-x}Co_x(OH)_2$ catalysts using different assumptions about the total number of electrons transferred.

2.4 Theoretical Methods

2.4.1 DFT Calculations

Density Functional Theory (DFT) calculations were conducted using the Vienna Ab-initio Simulation Package (VASP) with the aid of the Python-based Atomic Simulation Environment (ASE).[53–57] To account for the self-repulsion of elections in the d-orbitals that has been previously reported to result in spurious occupation and bandgap prediction, the generalized gradient approximation with Hubbard correction potential (GGA+U) method was used with the BEEF-vdW exchange-correlation functional.[58–60] Spin-polarization calculations were carried out in the antiferromagnetic configuration with initialized magnetic moments of 1.6 μB and 2.2 μB for Ni and Co atoms, respectively, which allowed the calculations to converge to final magnetic moments similar to experimental values (discussed in Chapter 5). The β-$Ni(OH)_2$ bulk unit cell (mp-27912 primitive cell structure) was relaxed until the atomic forces were minimized to be less than 0.05 eV/Å using an energy cut-off of 800 eV and sampled with a Monkhorst-Pack k-point mesh of (16x16x8); this cell relaxation was carried out twice consecutively to remove Pulay stress from the final optimized structure. The optimized bulk cell was then propagated into a (2x2x4) supercell with a vacuum length of 15 Å between repeating layers in the z-direction. Interactions between periodic images were decoupled in the z-direction with a dipole correction.[61] For geometry optimizations, the bottom two layers of the supercell had their positions constrained (as seen in Figure 2.4) and the rest of the cell was relaxed with an energy cut-off of 500 eV and sampled with a Monkhorst-Pack k-point mesh of (4x4x1).

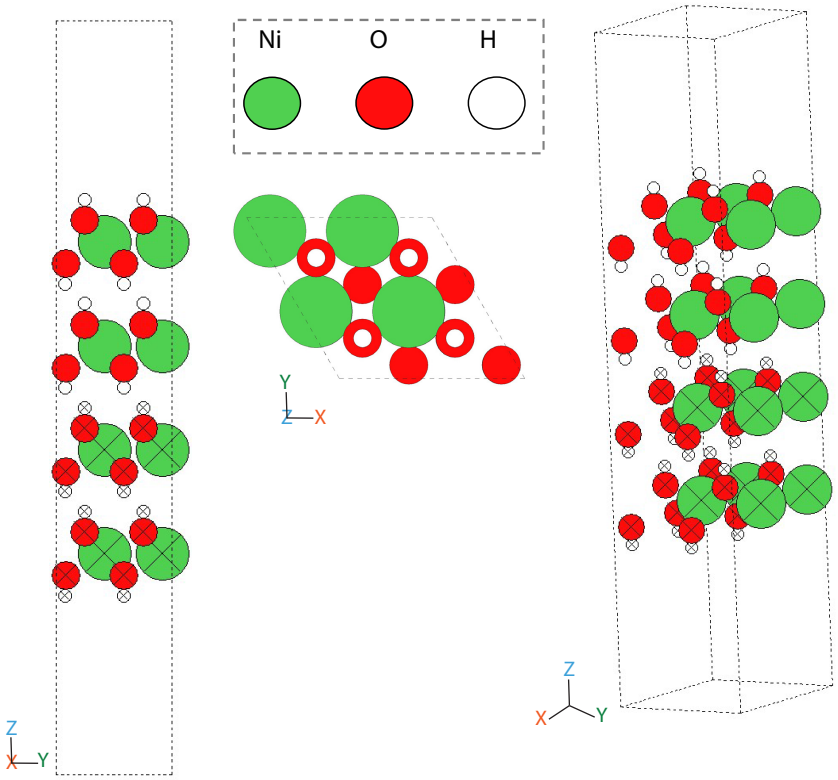

Figure 2.4: Structure of β-Ni$(OH)_2$ model used in a)side perspective and b)top-down perspective. Constrained atoms are denoted by X.

2.4.2 Determination of Hubbard Potentials

Due to the large variation of U potentials for Ni and Co oxides and oxyhydroxides, along with the lack of reported U potentials for Ni and Co in the β-M$(OH)_2$ lattice (Ni$(OH)_2$: mp-27912; Co$(OH)_2$: mp-24105), this thesis systematically determined the correct potentials by evaluating two of the most common methods: 1) Linear response theory and 2) optimizing with different values of U and comparing results to known experimental parameters (discussed in Chapter 5). All linear response theory calculations

were performed based on the script posted in the VASP manual.[62,63]

Table 2.1: Literature Reported values of U for Ni(II/III) in Ni oxides/hydroxides/oxyhydroxides

Method Used to Determine U	System	U (eV)	References
Linear Response Theory PBE (QE)	NiOOH Ni(*III*)	5.5	[64]
Linear Response Theory PBE (VASP)	NiO Ni(*II*)	3.8	[65]
Reaction enthalpy as function of U PBE (VASP)	NiO Ni(*II*)	6.4	[66]
Ab initio values obtained for average of several metals in metal oxides by Linear Response Theory (PBE)	N/A	4	[67]
Selected Based on NiOOH DFT+U reports	β-Ni$(OH)_2$ Ni(*II*)	5.5	[68]

2.4.3 PDOS and Charge Density Difference Calculations

To calculate the projected density of states and the charge density difference, the optimized (2x2x4) supercells first underwent a self-consistent calculation with an energy cut-off of 500 eV and sampled with a Monkhorst-Pack k-point mesh of (4x4x1), to get an approximation of the starting wavefunctions and charge density for use in subsequent calculations. Following this, a non-self-consistent calculation starting from the previous wavefunctions and charge densities sampled with a Monkhorst-Pack k-point mesh of (9x9x1) was conducted. To obtain the projected density of states, VASPKIT was used to parse the calculated data.[69] The charge density differences of Co doped surfaces were generated in VESTA based on equation (2.6) below.[70]

$$\Delta\rho_{dopedsurface} = \rho_{dopedsupercell} - \rho_{isolateddopantatom(s)} + \rho_{isolatedNiatom(s)indopantsite(s)} - \rho_{undopedsupercell} \tag{2.6}$$

Chapter 3

Characterization of Sol-gel derived Cobalt-Nickel Xerogels

3.1 Elemental Analysis

Inspired by recent reports of UOR catalysts with high activity and the known ability to achieve homogenous doping, the epoxide sol-gel synthesis was optimized to controllably produce $Ni_{1-x}Co_x(OH)_{2-y}Cl_y$ catalysts with specific Ni:Co ratios.[22,49,71] ln order to verify that the element distribution is uniform, select Ni:Co sol-gel catalysts were imaged by SEM with spatial EDX mapping. As is evident from Figure 3.1a and Figures A.1-A.5 the mixing of metal cations across the surface was homogeneous. Figure 3.1b shows that the experimentally determined atomic ratio of Ni:Co by both EDX and ICP-MS was in good agreement, which suggests that the Ni:Co ratio in the bulk lattice was the same

as the surface in addition to being the same as the ratio of metal precursors used in synthesis (see Figures A.1-A.6 in appendix A for additional EDX data). Selected area EDX spectra show that the Cl content rises with increasing Co incorporation, suggesting different stoichiometric ratios between the pure Ni and Co phases. To better understand the atomic structure of the Ni and Co phases and their evolution with changing Ni:Co ratio, a combination of PXRD, UV-Vis Spectroscopy, Raman Spectroscopy, and XPS were used to extract structural and electronic changes.

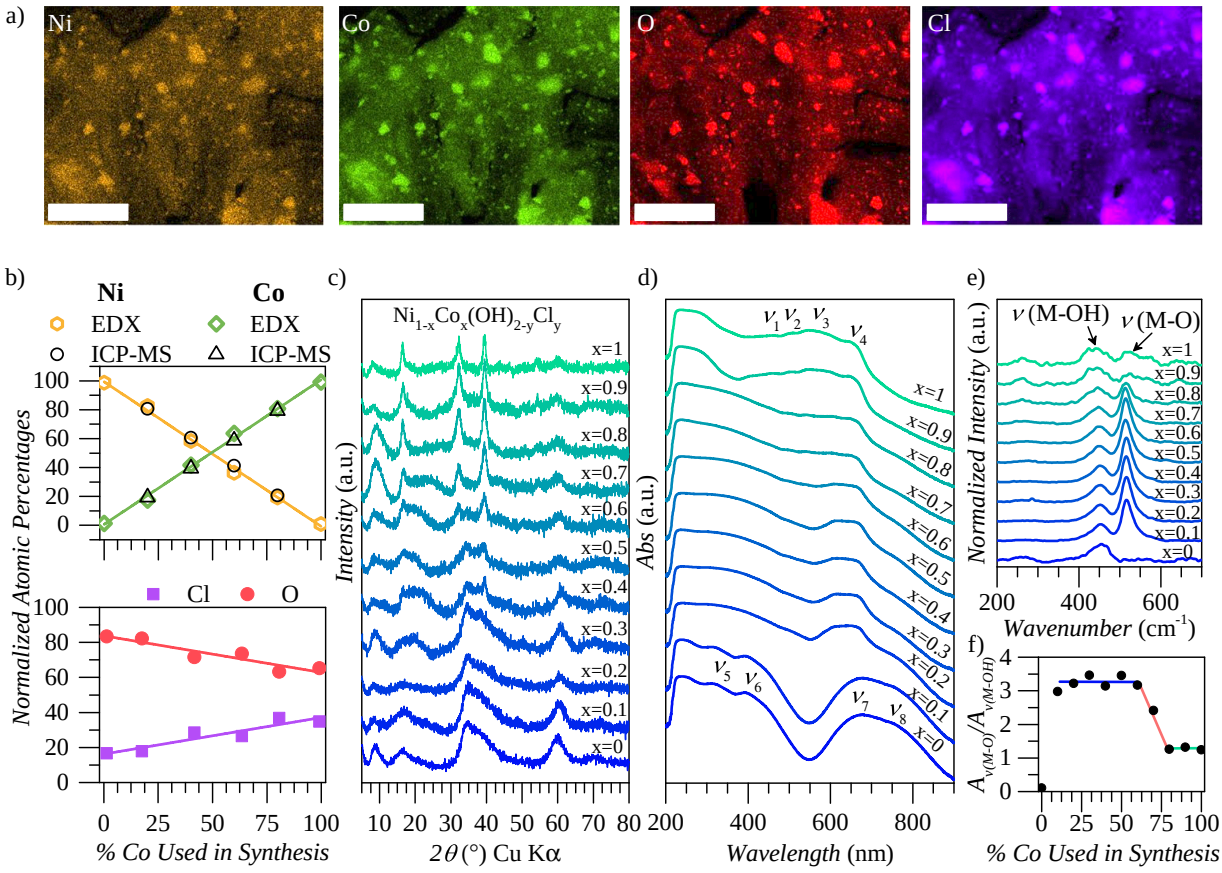

Figure 3.1: a) SEM-EDX spatial mapping of $Ni_{20}Co_{80}(OH)_2$ on carbon fiber paper. Scale bars are 20 μm. b) Change in atomic percentages of Ni, Co, Cl, and O measured by selected area EDX with additional ICP-MS measurements for Ni and Co. Ni-Co and Cl-O atomic percentages were normalized by either M/Ni+Co or X/Cl+O. c) PXRD of $Ni_{1-x}Co_x(OH)_2$ catalysts on a zero-background substrate. d) Normalized absorbance UV-Vis spectra of $Ni_{1-x}Co_x(OH)_2$ catalyst powders. e) Raman spectra of M-OH and M-O vibrations in $Ni_{1-x}Co_x(OH)_2$ catalysts. f) Raman spectroscopy correlation between ν(M-OH) and ν(M-O) peak areas from (f).

3.2 PXRD

The PXRD patterns in Figure 3.1c show a gradual transition between the pure Ni phase (x=0) and pure Co phase (x=1), both of which appear to be the α– polymorphs of $Ni(OH)_2$ and $Co(OH)_2$ and match the results obtained from other Ni or Co epoxide sol-gel protocols, calculated PXRD patterns (Figure 3.2), and PXRD patterns reported in the literature.[72–74]

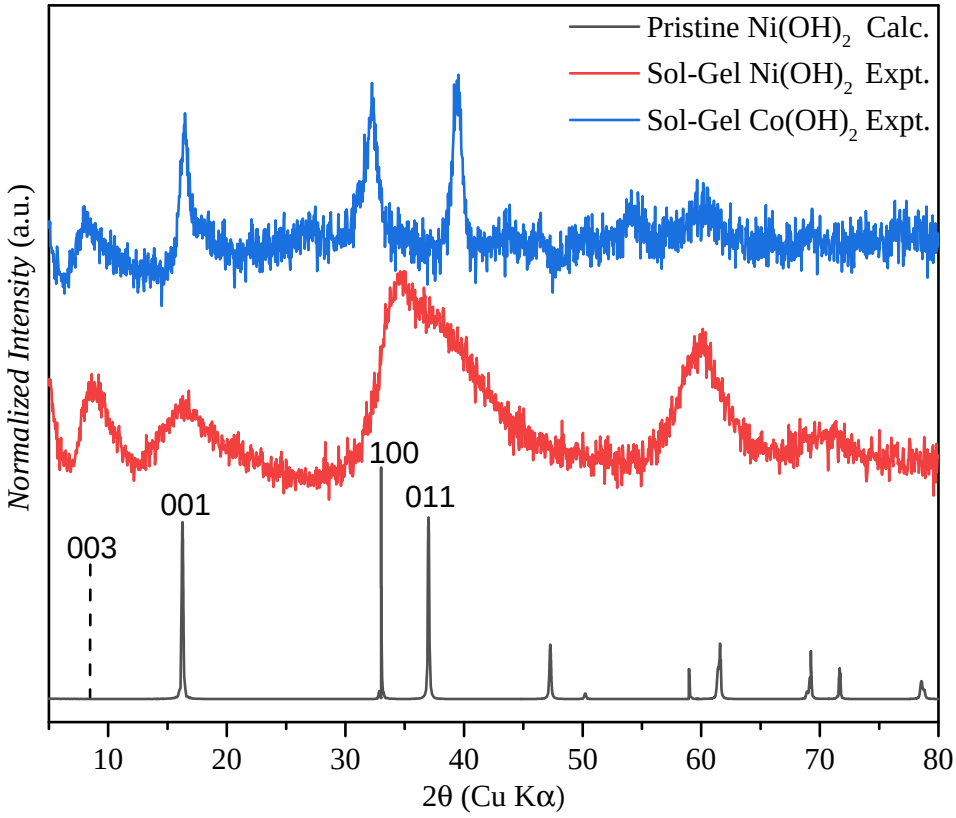

Figure 3.2: Calculated PXRD Pattern with CIREALS. The dashed line denotes the 003 peak from the experimental measurements that was absent in the simple calculation of the pristine $Ni(OH)_2$ structure.

Qualitatively, in Figure 3.1c the peak widths became narrower with increasing Co incorporation. This trend can be attributed to increased crystallinity of $Ni_{1-x}Co_x(OH)_{2-y}Cl_y$ with increasing Co content, which was confirmed by high magnification TEM imaging (Figure 3.3). While all studied compositions showed uniform surface coverage based on conventional SEM analysis (Figure 3.4), high magnification TEM and SEM analysis revealed an increase in the number and size of observable crystallite domains and an associated change in nanoscale surface roughness. This trend in the morphology is in agreement with the commonly observed increase in the ECSA and single crystal size in $Ni_{1-x}Co_x(OH)_2$ with increasing Co content.[39,40]

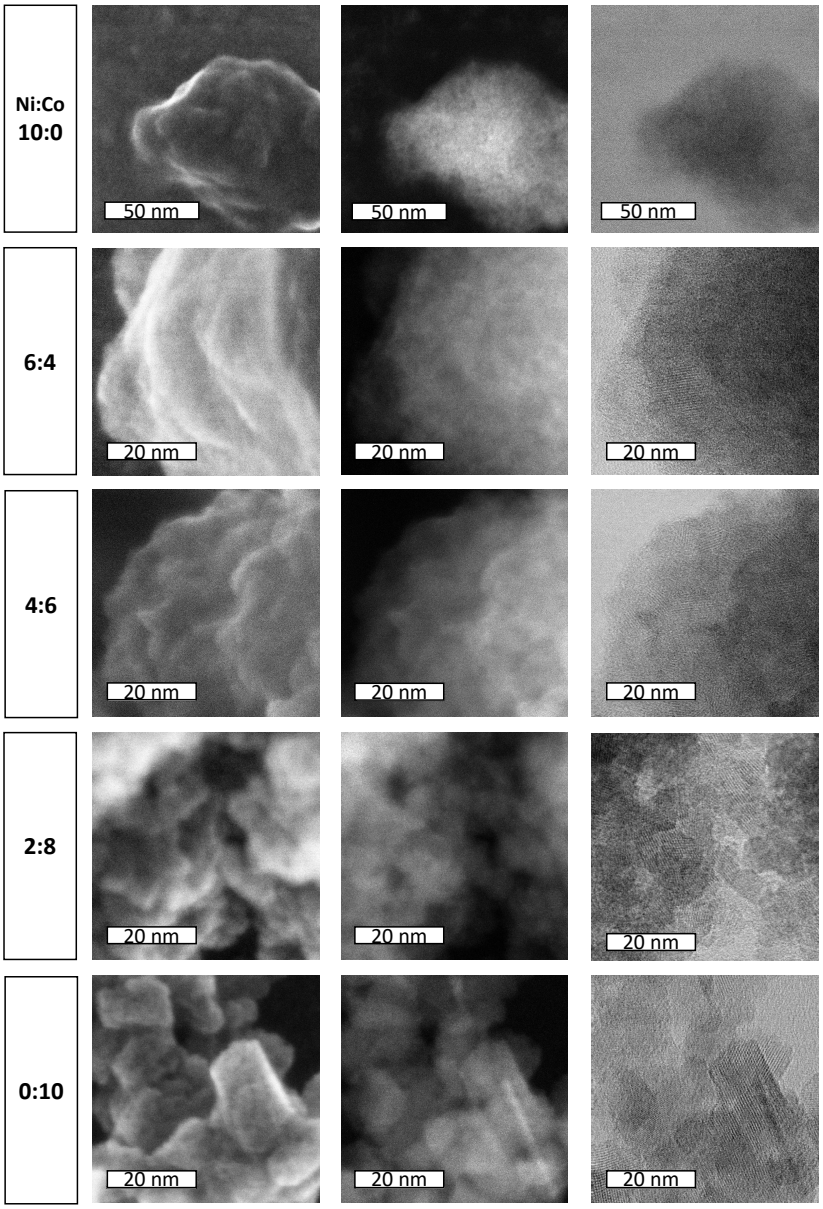

Figure 3.3: High magnification SEM images (first and second column), and TEM images (third column) of $Ni_{1-x}Co_x(OH)_{2-y}Cl_y$ dispersed on Cu/C TEM grids.

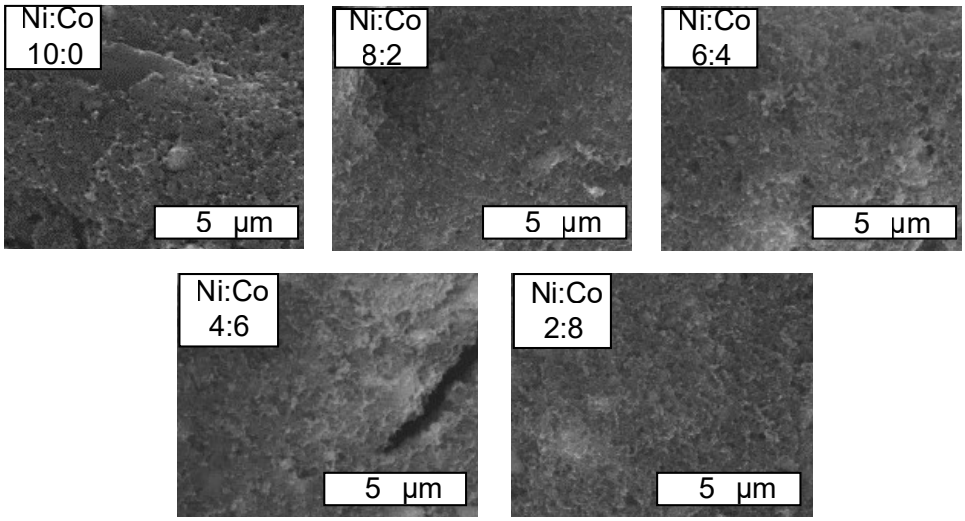

Figure 3.4: Low magnification SEM images of $Ni_{1-x}Co_x(OH)_{2-y}Cl_y$ dispersed on carbon fibres.

3.3 UV-Vis

From the UV-Vis absorption spectra in Figure 3.1d, a gradual transition between the pure Ni and Co phases can be observed. In particular, the pure Ni phase in this work (x=0) has transitions assigned to Ni^{2+} in an octahedral environment [393 nm $^3T_{1g}(P) \leftarrow^3 A_{2g}(F)$; 678 nm $^1E_g(G) \leftarrow^3 A_{2g}(F)$ and a shoulder between 719-760 nm $^1E_g(D) \leftarrow^3 A_{2g}(F)$] which have been previously reported for $Ni(OH)_2$.[75,76] In addition to this, the transition at 310 nm suggests the presence of Ni^{3+} based on reports of a Ni(*III*) transition in Ni_2O_3 and Ni(*III*) complexes being in a similar range.[75,77] The $Co(OH)_2$ phase shows the presence of Co^{2+} transitions in octahedral [462 nm $^4T_{1g}(P) \leftarrow^4 T_{1g}(F)$; 510 nm $^4A_{2g}(F) \leftarrow^4 T_{1g}(F)$ and tetrahedral 546 nm $^4T_1(P) \leftarrow^4 A_2(F)$; 641 nm $^4T_2(F) \leftarrow^4 A_2(F)$] environments.[76,78–81] The

presence of the tetrahedral Co environment in a layered hydroxide structure was previously demonstrated to occur in the presence of hydroxide substitution with chloride using both PXRD Rietveld refinements and X-ray absorption spectroscopy.[81] These results lead to the hypothesis that the linear correlation between Co and Cl concentrations observed in the elemental analysis is caused by the formation of tetrahedral Co sites in the crystal lattice.

3.4 Raman Spectroscopy

Raman spectroscopy measurements (Figure 3.1e) show that the pure nickel hydroxide phase has a peak at 455 cm^{-1} wavenumbers which were assigned to the Ni-OH lattice vibration (ν(M-OH) in Figure 1e). Since this peak is in the range of reported experimental peak assignments for α- and β-$Ni(OH)_2$ vibrational modes [α- peak 451-464 cm^{-1}; β-peak 445-453 cm^{-1}], one cannot confidently assign this peak to the Ni-OH lattice vibration from either of these two polymorphs.[74,82] The introduction of 10% Co led to the emergence of a new peak at 517 cm^{-1} (ν(M-O) in Figure 3.1e), which could originate from proton vacancies analogous to NiOOH regions within the bulk of the crystal lattice, as was previously reported for $Ni_{1-x}Co_x(OH)_2$ with Co concentrations as low as 1%.[83,84] The analysis of the ratio between the peak areas for ν(M-O) and ν(M-OH) modes (Figure 3.1f) revealed three regions across the composition range in these materials: 1) M-OOH rich region (blue line), 2) transition region (red line), and 3) M-OOH deficient region (green line). The transition region correlates with the key changes in the PXRD patterns and UV-Vis spectra correlates and confirms the change in the number of M-OOH sites in the structure of $Ni_{x-1}Co_x(OH)_{2-y}Cl_y$.

3.5 XPS

The calculated binding energies showed that the Ni 2p and Co 2p peaks are reduced with an increasing fraction of Co incorporated in the catalyst (Figure 3.5). The change of binding energies for the Ni $2p_{1/2}$ and $2p_{3/2}$ states typically observed in XPS for Ni oxides and hydroxides were previously attributed to the nature of the ligand coordinated to Ni.[85] The reduction in binding energy is believed to originate from an increase of kinetic energy of the outgoing photoelectrons caused by the localization of unoccupied orbitals right above the Fermi level in a potential well.[85] In other words, the more unoccupied states become localized in the potential well, the larger the reduction in the binding energy of the Ni 2p peaks one would expect to see. It is worth noting that the Co 2p peaks are moving towards the pure Co phase sample positions, while the Ni 2p peaks are moving below the pure Ni phase (Figure 3.5). This trend suggests that increasing the Co concentration increases the number of electrons that are localized at the Ni centers in these catalysts. During electrolysis, the valance states of catalysts of this type tend to increase, based on the reported in situ studies.[51,86,87]

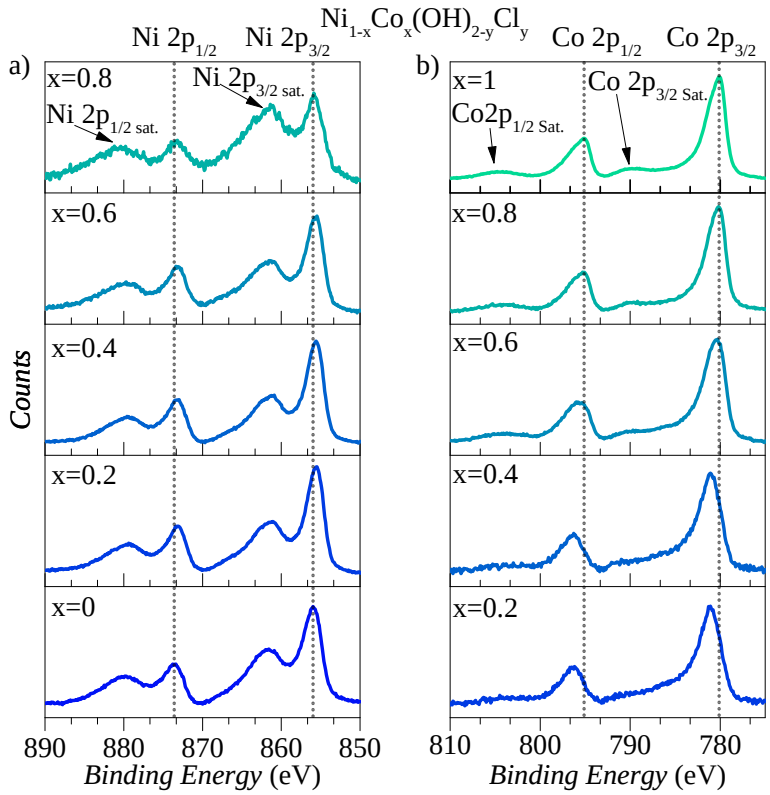

Figure 3.5: a) Ni 2p and (b) Cl 2p XPS spectra of $Ni_{1-x}Co_x(OH)_2$ catalysts on carbon fibres after electrochemical activation.

3.6 Summary of Chapter 3

Through the combination of a large number of characterization techniques the change in elemental composition, elemental distribution on the surface, crystal structure, surface chemistry, electronic structure, and morphology of Co doped $Ni(OH)_{2-y}Cl_y$ xerogels derived from a propylene oxide-based sol-gel synthesis with increasing Co incorporation was evaluated.

SEM imaging with spatial EDX mapping analysis of the distribution of Ni, Co, O, and

Cl on the surface of the prepared catalysts showed that mixing of elements across the surface was homogeneous. The atomic ratio of Ni:Co was demonstrated by both EDX and ICP-MS, showing that the bulk Ni:Co ratio was the same as the surface. A combination of PXRD, UV-Vis spectroscopy, and Raman spectroscopy was used to show how the synthesized materiel was in a layered hydroxide lattice with a sheet structure that was isostructural to brucite and confirmed that metal oxides did not exist in the bulk lattice. Furthermore, high magnification TEM and SEM imaging showed that the change in peak widths observed in the PXRD patterns with changing the Co fraction was due to an increase in the number and size of observation crystallite domains and an associated change in nanoscale surface roughness. Through UV-Vis spectroscopy, electronic transitions that indicate the presence of a tetrahedral Co environment were observed in a layered hydroxide structure, leading to the hypothesis to occur due to the substitution of lattice hydroxide with chloride. Raman spectroscopy measurement provided further details on the change in surface chemistry, demonstrating the presence of M-OOH sites in the lattice and the composition range that is rich and deficient in these vacancies. Finally, XPS showed that as the amount of Co used in the catalyst was increased, that both Co and Ni are reduced in oxidation state which suggests that the pure Ni catalyst contained a mixture of higher valance states (*III* and/or *IV*.

While these methods describe how the catalyst changes before any electrochemical reaction, one must note that during electrolysis additional changes to the crystal structure, morphology, surface chemistry, valance states of catalysts can occur based on the reported *in-situ* studies.[51,86,87]

Chapter 4

Evaluation of Cobalt-Doped Nickel Hydroxide Performance for Urea Electrooxidation

4.1 Determining Capacitance and OER Current for Baseline Subtraction of Anodic Redox Peaks.

The influence of Co on the electrochemical behaviour of the synthesized catalysts was probed by performing CV scans at 20 mV/s on activated materials (as discussed in Chapter 2) in 1 M KOH. Since UOR is reported to occur on oxidized $Ni(OH)_2$, only the anodic traces are shown of all CV measurements in Figure 4.2 below; see Figure A.ll in appendix A for full CV scans. The electrochemical activation procedure performed prior to electrochemical

characterization removed all Cl from the surface of the electrode as was confirmed by XPS analysis of the anodes before and after activation (Figure 4.1).

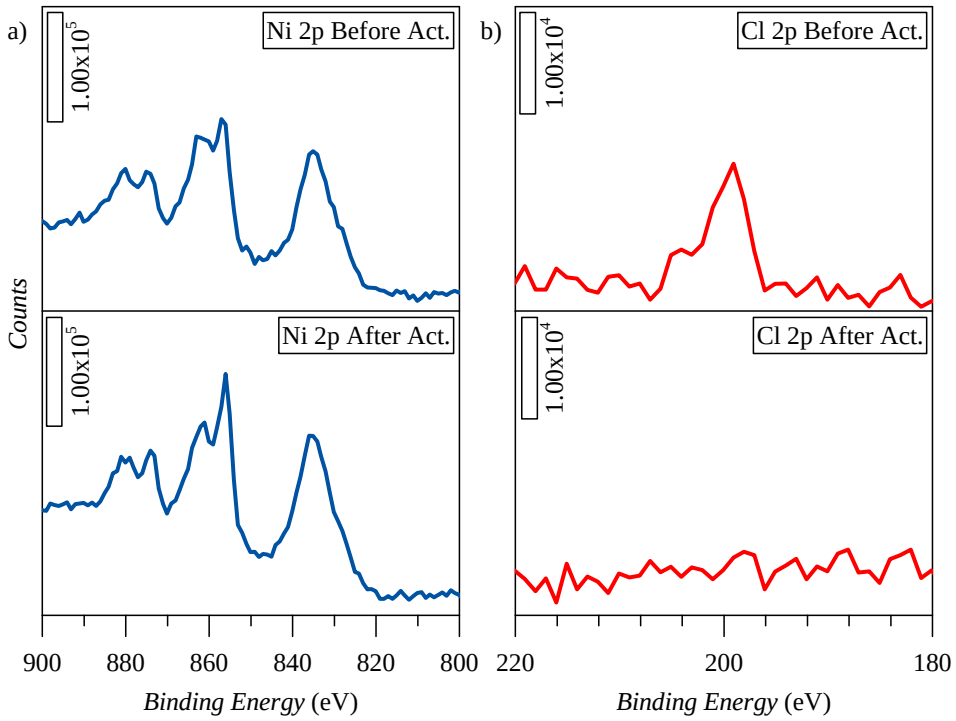

Figure 4.1: a) Ni 2p and (b) Co 2p XPS spectra of $Ni_{1-x}Co_x(OH)_2$ catalysts on carbon fibres after electrochemical activation.

4.2 Evaluation of UOR activity

From increasing the Co content in the catalyst material, there was a clear change in CV peak position, width, and geometric current density (GCD) that was associated with the redox reactions for Ni and Co in alkaline electrolytes (Figure 4.2a).[28,86] The redox-active potential range increases with increasing Co incorporation along with a decrease in the

integrated area (Figure 2.2). With the normalized baseline and the OER-deconvoluted current in Figure 4.2c, the peak current per RASS is maximized at $Ni_{60}Co_{40}(OH)_2$ suggesting that the intrinsic activity per active site towards oxidizing Ni is maximized here. When comparing how the number of RASS per geometric surface area change with composition (Figure 4.2f), one can see that as the amount of Co increased, the number of RASS decreased in a semi-linear fashion until the inflection at $Ni_{40}Co_{60}(OH)_2$. The deviation from the qualitatively linear trend coincides with the trends discussed in Chapter 3 observed by PXRD, UV-Vis spectroscopy, Raman spectroscopy, SEM, and TEM (Figures 3.1c-e, 3.3, and 3.4) and the change in the emergence of a second redox peak (Figure 4.2c). Hence, the observed inflection point in Figure 4.2d clearly shows the beginning of the transition region where both the structure and electrochemical behaviour show more $Co(OH)_2$ characteristics. It is important to note that the RASS per geometric surface area is not the physical surface area of the electrode, but rather an approximation of the number of Ni and Co sites that will participate in a redox reaction.

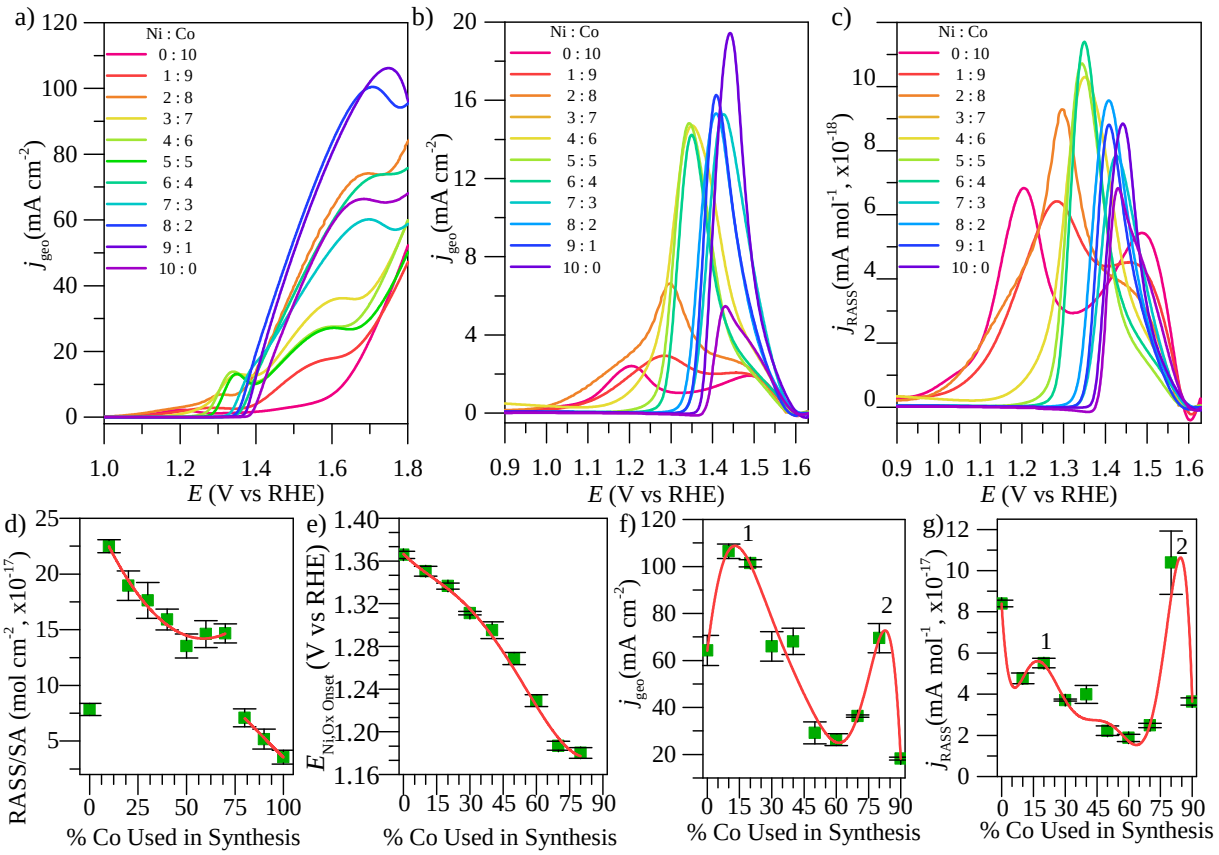

Figure 4.2: a) Anodic CV sweeps of activated $Ni_{1-x}Co_x(OH)_2$ catalysts in 1 M KOH with 0.33 M urea at 20 mV/s normalized by the geometric surface area. b) Anodic CV sweeps of activated $Ni_{1-x}Co_x(OH)_2$ catalysts in 1 M KOH at 20 mV/s normalized by the geometric surface area with OER current subtracted. c) Anodic CV sweeps of activated Ni1-xCox(OH)2 catalysts in 1 M KOH at 20 mV/s normalized by the number of RASS with OER current subtracted. d) Change in the number of RASS normalized by surface area with increasing Co concentration in $Ni_{1-x}Co_x(OH)_2$ catalysts. e) Change in Ni oxidation onset potential with increasing Co concentration in $Ni_{1-x}Co_x(OH)_2$ catalysts. f) Change in maximum GCD of UOR peak with increasing Co concentration in $Ni_{1-x}Co_x(OH)_2$ catalysts. g) Change in maximum current density per number of RASS of UOR peak with increasing Co concentration in $Ni_{1-x}Co_x(OH)_2$ catalysts.

To understand the UOR performance of different activated $Ni_{1-x}Co_x(OH)_2$ catalysts, CV experiments as described in Chapter 2 as was conducted. Figure 4.2a shows how the GCD differs as a function of Co composition in the catalyst. The highest geometric current density was achieved with $Ni_{90}Co_{10}(OH)_2$, similar to what has been previously reported for $Ni_{1-x}Co_x(OH)_2$ hydroxide catalysts for UOR (see Tables A.1, A.2, and A.3 in appendix A).[38] Furthermore, the UOR response for the $Co(OH)_2$ phase was similar to Zhang et al. which shows an increase in current in the presence of urea before the OER onset.[22] To analyze how the Co composition influenced UOR activity, the geometric and RASS-normalized peak current densities (Figures 4.2f-g) were plotted. In the GCD trend (Figure 4.2f), there are two clear peaks (denoted as 1 for $Ni_{80}Co_{20}(OH)_2$ and 2 for $Ni_{20}Co_{80}(OH)_2$ in the figure) that have larger GCDs than $Ni(OH)_2$, with a valley at $Ni_{40}Co_{60}(OH)_2$, the transition point mentioned above. Interestingly, when normalized by RASS (Figure 4.2g), peak 1 becomes smaller for pure $Ni(OH)_2$ while peak 2 relatively increases. This change in the trend suggests that peak 1 originates from maximizing the number of RASS participating in the reaction, while peak 2 is caused by maximization of the intrinsic activity of the catalyst towards UOR.

4.3 Evaluation of Electrode Stability

By examining the change in RASS before and after evaluating UOR activity the stability of materials as a function of Co incorporation was evaluated (Figure 4.3). To calculate the percent difference in RASS, baseline fitting as described in the previous section was used on CV scans of each electrode before and after the UOR CV scans. The RASS after the

reaction was then subtracted from the RASS before and divided by the RASS before to show the percent difference between the two measurements. The RASS was determined for unused catalysts and catalysts subjected to 20 CV cycles in the presence of urea to assess catalyst stability. The addition of Co improves the stability of the catalyst somewhat as the decrease in RASS is minimal after 20 CV cycles (*ca.* 11% decrease in RASS) relative to $Ni(OH)_2$ (*ca.* 36% loss of RASS). Increasing Co content does not appear to increase stability.

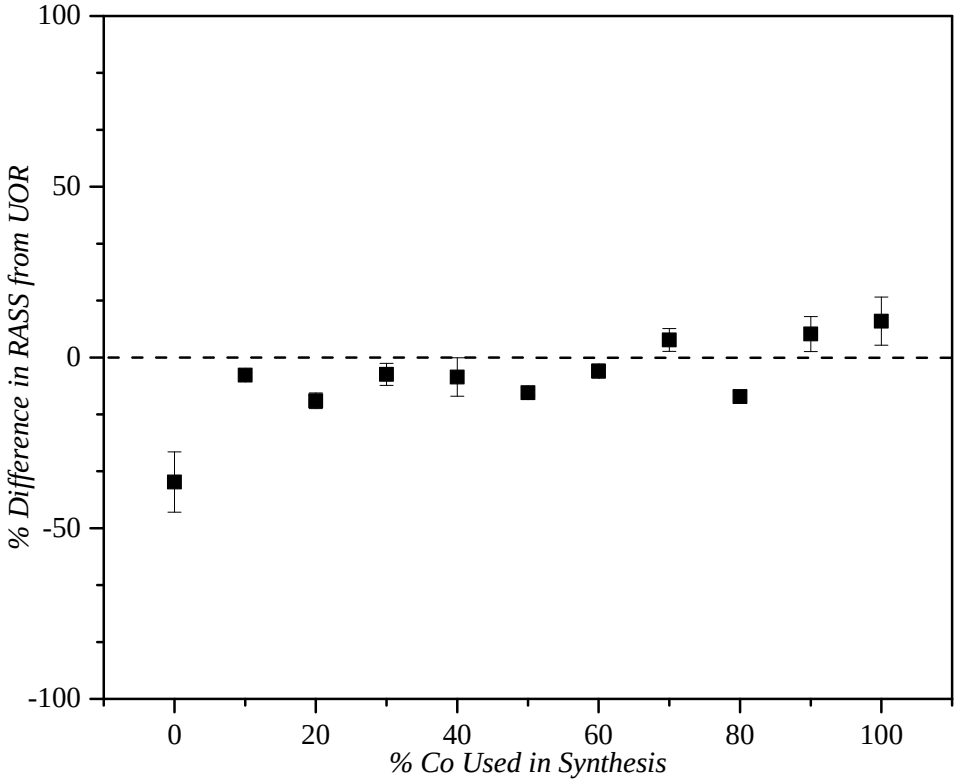

Figure 4.3: Evaluation in percent difference of the number of RASS in $Ni_{1-x}Co_x(OH)_2$ catalysts after 20 CV cycles at 20 mV/s in 1 M KOH+0.33 M urea.

4.4 Evidence Towards Inductive Effect

From further analysis of the redox activity in KOH, it becomes clear that the Ni onset potential shifts towards lower potentials with increasing Co incorporation as predicted by the inductive effect (Figure 4.2e). In the context of this work, the inductive effect occurs by introducing a weaker Lewis acid than the parent metal, i.e. Co(II) in a Ni(II) matrix, which pushes electron density towards the parent metal and shifts the antibonding states toward the Fermi level, resulting in a decrease in the redox potential of Ni.[88] This decrease in redox potentials is well known to reduce the intrinsic OER activity of Ni surface sites.[88] Hence, this evidence supports the notion that Co modulates the electronic states in $Ni(OH)_2$. Furthermore, it was suggested that Co shifts the electronic states of Ni by changing the energy of the O 2p states that bond with the Ni 3d states. This specific electronic state modulation route has not been explicitly demonstrated in the $Ni_{1-x}Co_x(OH)_2$ system.

4.5 Summary of Chapter 4

$Ni_{1-x}Co_x(OH)_{2-y}Cl_y$ xerogel catalysts were screened for UOR activity. Herein, an in-depth analysis of cyclic voltammetry measurements revised how the number of RASS per surface area will decrease with increasing the Co fraction used in the synthesis. The geometric current density for UOR was maximized for $Ni_{90}Co_{10}(OH)_2$ due to the optimization of the number of redox-active surface sites that could participate in the reaction. Interestingly, the current density per the number of redox-active sites was maximized for $Ni_{20}Co_{80}(OH)_2$, demonstrating that intrinsic activity of the redox-active

surface sites can be increased through the addition of Co. Furthermore, the observed reduction in onset potential for $Ni(OH)_2$ oxidation with increasing Co doping suggests that the electronic structure of Ni is being altered.

Chapter 5

Ab Initio model of Cobalt-Doped Nickel Hydroxide Electronic Structure

5.1 Defining DFT modeling

In general, numerous reports indicate that changing the electronic structure of Ni is the most promising strategy for maximizing the intrinsic activity of UOR.[17] To investigate how Co will change the electronic states in the $Ni_{1-x}Co_x(OH)_2$ catalysts and subsequently deduce how this may influence intrinsic activity towards UOR, DFT calculations was performed for structures with increasing Co doping. It has been established that the degree of modification of the electronic structure depends on the way the dopant is incorporated

into the catalyst and the concentration of the dopant.[71,89] While cation substitution can induce several forms of structural disorder in α- or β- polymorphs of $Ni(OH)_2$ (point defects, stacking faults, intercalation of foreign ions between layers, and different degrees of hydration, and α/β- interstratification to name a few), it is not necessary to model them to observe the effects Co atoms have on the electronic states in $Ni_{1-x}Co_x(OH)_2$ catalysts.[74] $Ni(OH)_2$ was chosen as the base material in the model presented in this thesis due to observations in this work and the literature that Co sites have very little activity towards UOR.[29,44] For both $Ni(OH)_2$ and $Co(OH)_2$, it is known that through both electrochemical activation and ageing in KOH electrolyte that intercalated ions (e.g. Cl^- in this work) and water are removed from between the layers, resulting in the materials transformation into the β- phase which is the most thermodynamically stable phase for both $Ni(OH)_2$ and $Co(OH)_2$.[29,90,91] Even though other different phases and materials such as α-$Ni(OH)_2$ and γ-NiOOH are known to form in situ, β-$Ni(OH)_2$ is likely the most dominant phase under experimental conditions due to chemical ageing prior to electrochemical testing. Thus, the system was modelled by studying the change in the electronic structure of β-$Ni(OH)_2$ with increasing concentration of Co in the top layer.

5.2 Determination of Hubbard Potentials

The initial magnetic moments in the models used in this thesis were set to be antiferromagnetic between neighbouring layers (along the c axis) based on neutron diffraction and magnetometer experiments reported in the literature.[92,93] To account for the self-repulsion of elections in the d-orbitals that have been previously reported to result

in inaccurate occupancies and band gaps, the generalized gradient approximation with a Hubbard correction potential (GGA+U) method was used with the BEEF-vdW exchange-correlation functional.[58–60] From an examination of the Hubbard potentials (U) determined in the literature, two key points can be observed. First, reports that determined U for Ni(*II*), did so for NiO or NiOOH using the Perdew-Burke-Ernzerhof (PBE) functional (See Table 2.1 in Chapter 2).[94] In addition, these reported values vary between 4-7 eV depending on the method used.[66,95–97] Since it is not clear which value should be used, the two most commonly used methods were compared to determine the Hubbard potential in semiconductor materials to ensure that the calculation of the electronic state was accurate.

The first method is linear response theory, which is based on determining how the number of electrons at the atom of interest changes between self-consistent and non-self-consistent calculations over a range of Hubbard potentials.[62] A series of calculations were carried out over a range of U values (-0.20 to +0.20 V) for the bulk β-$Ni(OH)_2$ unit cell, resulting in a predicted Hubbard potential of 4.64 eV (Figure 5.1.[63]

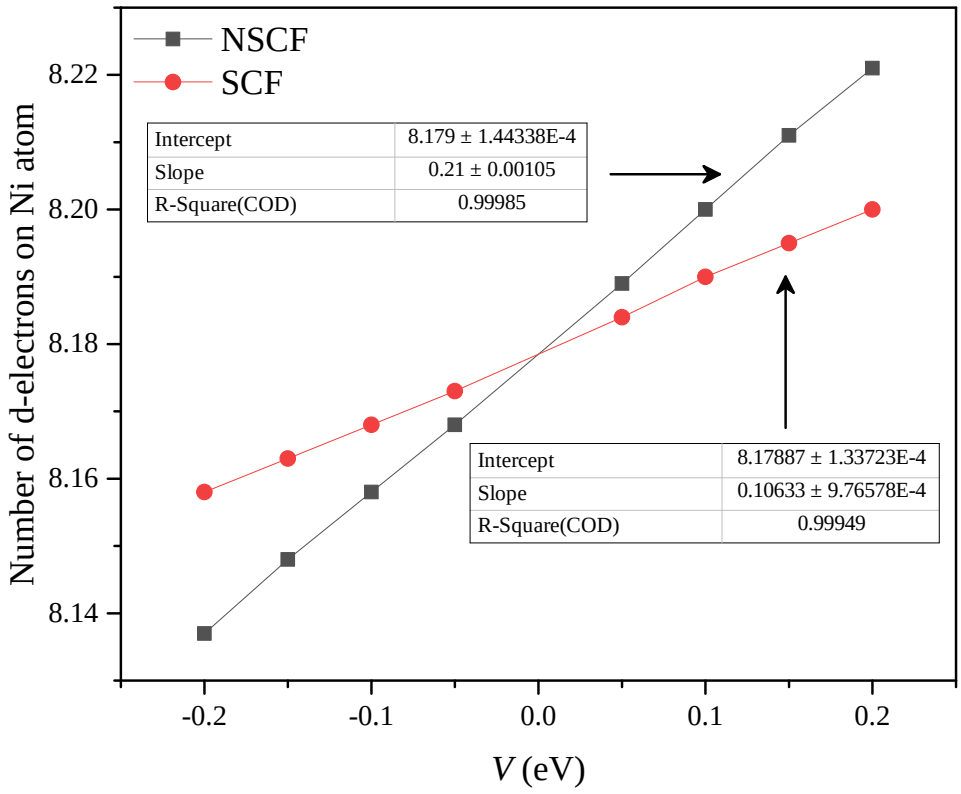

Figure 5.1: Linear response theory determination of U for β-Ni(OH)$_2$.

The second method was a series of calculations that consist of two-unit cell relaxations followed by one geometric relaxation (see Chapter 2 for details). Figure 5.3b shows how the bandgap of the material from the density of states, and the local magnetic moment of Ni changed as a function of U. With this approach, an optical bandgap and the local magnetic moment of Ni that was similar to the experimental measurements for β-Ni(OH)$_2$ (E$_g$=$\sim$3.0-3.5 eV; 2.0$\pm$0.2 μB) was achieved with a Hubbard potential of 5.5 eV (Figure 5.3b).[92,93] It is worth noting that the difference between using PBE and BEEF functionals

was contrasted for these calculations and found that they both follow a nearly identical linear trend. Following these results, U for Co(II) in the bulk β-Co(OH)$_2$ unit cell was determined by matching the bandgap to the experimental value of 2.85 eV (Figure 5.2).[98] For Co, the value of U was found to be 3.72 eV, which is within the range of reported values of Co(II) in Co oxides (3-8 eV).[66,99–101] From these results, Hubbard potentials of 5.5 eV and 3.72 eV were used for Ni(II) and Co(II) for all remaining calculations in this work.

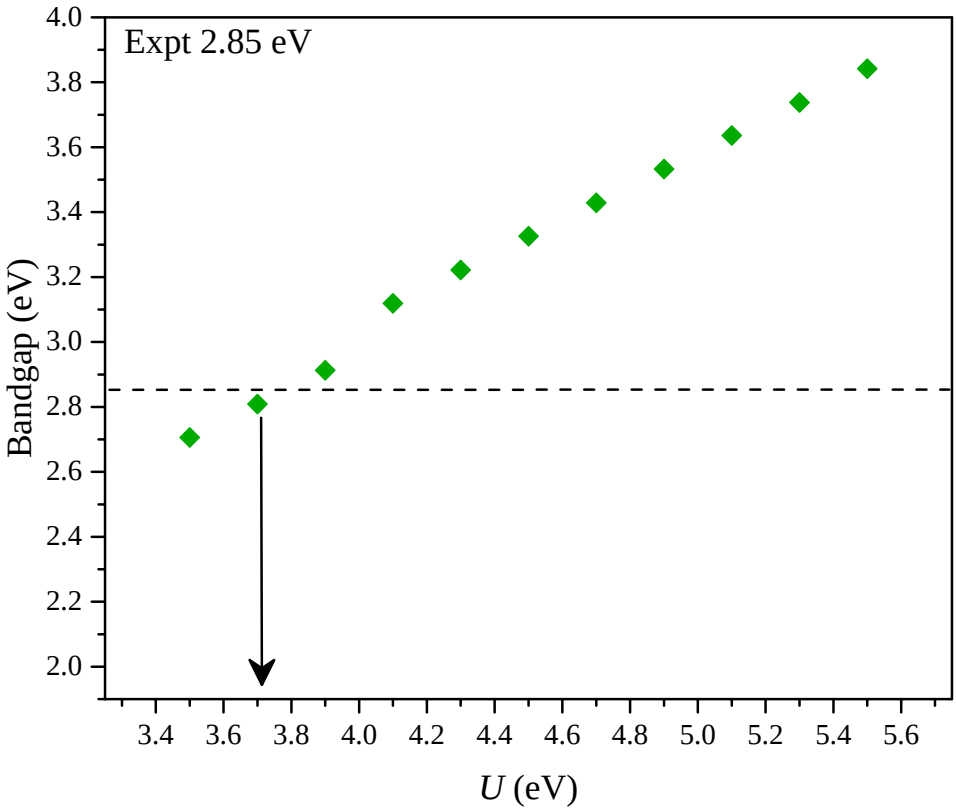

Figure 5.2: Determination of U in β-Co(OH)$_2$ by fitting to bandgap.

5.3 Charge Density Difference of Cobalt-Doped Nickel Hydroxide

To understand how increasing the Co fraction in $Ni_{1-x}Co_x(OH)_2$ catalysts would alter the electronic structure, the change in electron charge density from the pristine β-$Ni(OH)_2$ surface by doping the top monolayer in 25% increments was calculated (Figure 5.3a). Here, one can see that the charge density difference (CDD) surrounding the hydroxide moieties changes by decreasing the density along with the Co-OH bond. The excess charge density is then distributed between the neighbouring Ni atoms bound to the perturbed hydroxide. This observation coincides with the experimental result that shows the redox potential continuously shifting towards more negative values based on the inductive effect described above. Furthermore, as the concentration of Co in the monolayer increases, one can see that the charge accumulation becomes more aligned with the Ni-OH bond and that the charge density distribution surrounding the Ni atoms is perturbed.

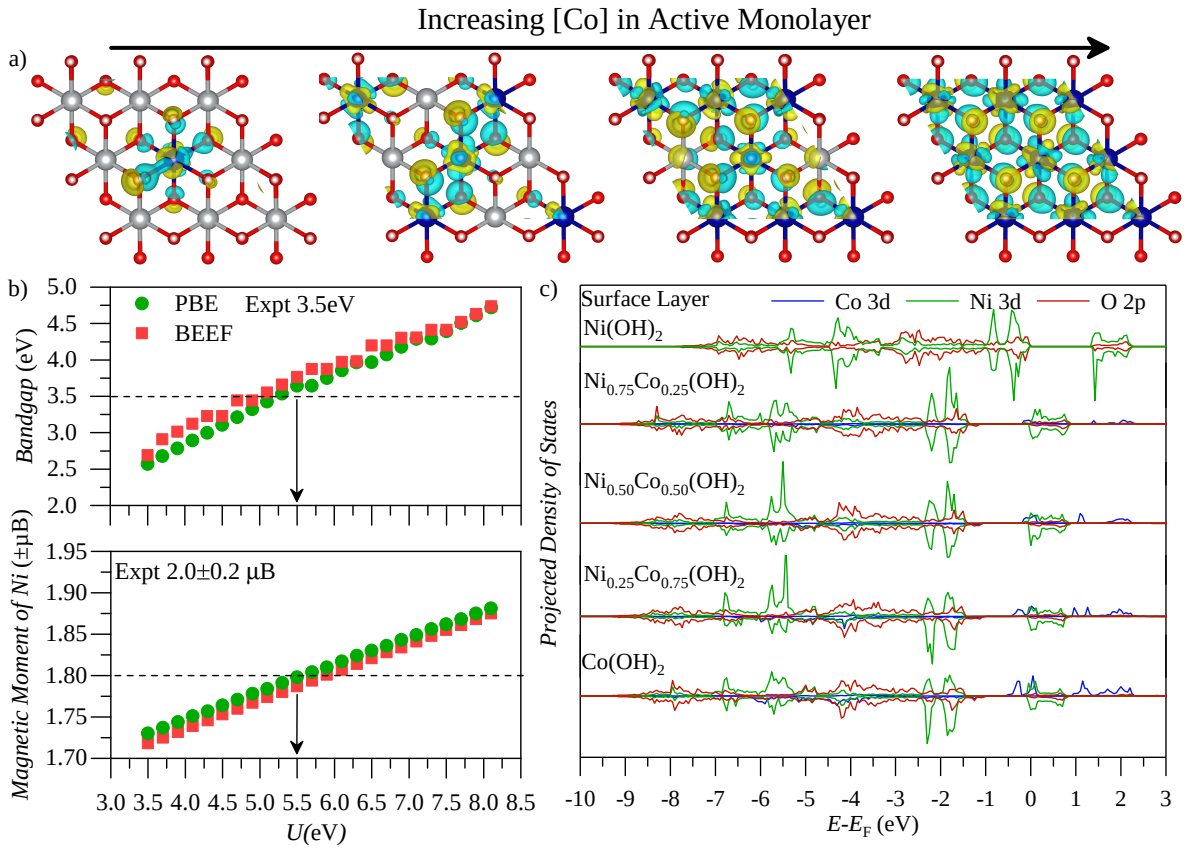

Figure 5.3: a) Charge density difference of Co doped surface from undoped surface. Yellow isosurfaces represent electron density depletion, while blue isosurfaces represent electron density accumulation. The sign of all charges used in calculations was positive. b) Changes in calculated bandgap and local magnetic moments of Ni in bulk β-$Ni(OH)_2$ with different Hubbard potentials applied to Ni c) Projected density of states showing the electronic state of 2x2x4 β-$Ni(OH)_2$ with increasing Co concentration in the surface layer of the supercell.

5.4 Projected Density of States of Cobalt-Doped Nickel Hydroxide

While the observations in the CDD maps confirm the inductive effect occurs, there still remains a lack of understanding of which electronic states are responsible for the observed changes. To address this, the projected density of states (PDOS) calculations were performed using the same structural models used in the CDD calculations, as seen in Figure 5.3c. It appears that the addition of Co to the surface layer alters the Ni 3d states in several different ways. First, the anti-bonding states are shifted down monotonically as Co doping increased, which would alter the adsorption energy of different reaction intermediates in addition to oxidizing Ni. Hence, these results explain the experimental trends observed for the change in valence states for the Ni 2p and Co 2p measurements in Figure 3.5.

Furthermore, one can observe large changes in the Ni 3d density distribution with increases in Co concentration through an orbital decomposition of the projected density of states (Figure 5.4). Each decomposed projected state density will continuously shift downwards with increasing Co content of the surface layer, with the largest shift in energy occurring at the transition from 0 to 25% Co. The maximum population of each state was found to change when transitioning from 25 to 75% Co. In particular, the density of the majority spin of the $3d_{x^2-y^2}$ and $3d_{xy}$ states at -1.80 eV was reduced, while the state population maxima for the majority spin at -5 to -6 eV were gradually increased in density (Figure 5.4). The $3d_{z^2}$ state has a similar decrease in population for the majority spin at -1.80 eV, but a larger increase in the majority spin between -5 to -6 eV. Additionally,

as the Co content in the surface layer increases there is an increase in the population of the minority spin at around -1.80 eV. The $3d_{xz}$ and $3d_{yz}$ orbital states, in contrast to the previously mentioned Ni 3d-states have the smallest overall change in population density when increasing the amount of Co in the surface layer, which is likely caused by the low occupation of these states in pure β-$Ni(OH)_2$. Therefore, one can conclude that while all five Ni 3d states experience a similar downward shift in energy, the change in population density distribution altered by increasing the amount of Co atoms in the surface layer is most significant for the Ni $3d_{x^2-y^2}$, $3d_{xy}$, and $3d_{z^2}$ states. The surface Co composition ratios where the population densities are maximized (25% Co for the $3d_{x^2-y^2}$ and $3d_{xy}$ states and 75% Co for the $3d_{z^2}$ state) coincides with the experimental trends observed in this work for the change in electrochemical intrinsic activity towards UOR. This confirms that while the UOR activity on Co sites is very low compared to Ni sites, one can tune the electronic structure of Ni sites to maximize the intrinsic site activity of the anode towards UOR.

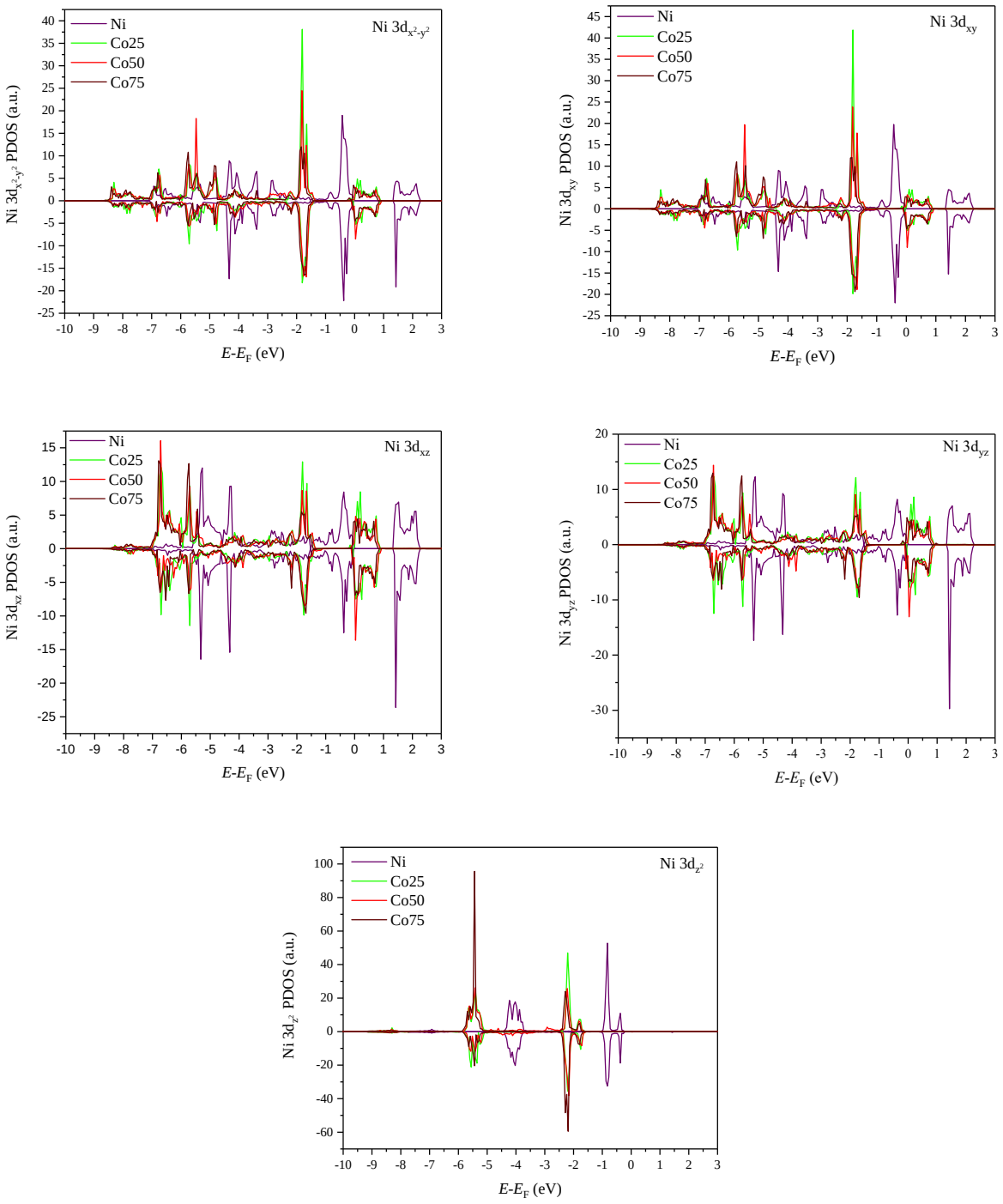

Figure 5.4: PDOS orbital decomposition for Ni 3d states in $Ni_{1-x}Co_x(OH)_2$

5.5 Trends in Converged Magnetic moment with Co Surface Layer Doping

From the PDOS calculations described above, a linear decrease was observed in the converged net magnetic moment of the (2x2x4) β-Ni$(OH)_2$ supercell (Figures 5.5). Further examination of the local magnetic moments of Ni and Co (Figure B.1-B.5 in appendix B) shows that increasing the Co content in the surface layer reduces the local Ni magnetic moments and increases the local Co magnetic moments. This may influence the adsorption and stability of certain reaction intermediates, however, further experimental and theoretical work is required to fully understand the influence magnetic moment may have on the UOR mechanistic pathway.[102–104]

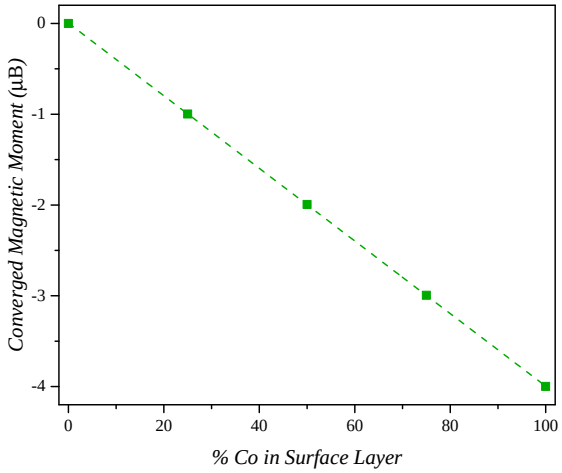

Figure 5.5: Change in calculated magnetic moment with increasing Co surface layer doping in (2x2x4) β-Ni$(OH)_2$ supercell

5.6 Summary of Chapter 5

To understand the role that Co doping may have on UOR, DFT calculations were performed by doping the surface of β-$Ni(OH)_2$ with Co atoms. The Hubbard potentials for Ni and Co in β-$Ni(OH)_2$ and β-$Co(OH)_2$ were systematically determined to best predict the electronic properties of β-$Ni_{1-x}(OH)_2$ catalysts. The charge density difference between undoped and surface doped (2x2x4) β-$Ni(OH)_2$ supercells showed that as Co fraction was increased in the top layer, more electron density is pushed towards the Ni atoms. Projected density of states calculations showed that with increased Co incorporation in the surface layer the Ni 3d states experience a downward shift in energy and redistribution of orbital density. The projected density of states was then decomposed into each Ni 3d orbital, which demonstrated that while each state is lowered in energy with increased Co doping, unique features of the state density were enhanced for 25 and 75% Co incorporation in the surface layer. Finally, a systematic change in the converged local magnetic moment was observed, where increasing Co in the surface layer reduces the local Ni magnetic moments and increases the local Co magnetic moments. The altered Ni 3d states are likely related to changes in the adsorption and may stabilize certain reaction intermediates. To better understand how changes in the local magnetic moment and electronic structure affect specific intermediates, follow-up studies should be focused on elucidating a detailed reaction mechanism both experimentally and theoretically on doped systems.

Chapter 6

Conclusions and Outlook

6.1 Conclusions

In summary, this thesis explored how changing the Co fraction in the modified propylene oxide synthesis of $Ni_{1-x}Co_x(OH)_{2-y}Cl_y$ xerogel catalysts alters both structural and electronic states which allows one to tune the number and intrinsic activity of redox-active surface sites towards UOR.

Extensive characterization of the synthesized catalyst before reactions revealed, for the first time, that the changes in the number and size of crystallite domains, changes in M-OOH surface site population, the appearance of $Co(OH)_2$ electronic transitions, and appearance of Co redox peaks occur at the composition where the change in the number of redox-active sites per surface area experiences an inflection from a semi-linear trend. Hence, in addition to characterizing materials that have been poorly characterized in the literature

(sol-gel derived $Ni(OH)_{2-y}Cl_y$ based xerogels), this thesis develops a novel electrochemical framework that allows the identification of compositions of $Ni(OH)_2$ based catalysts that display systematic changes in structural properties when dopant concentrations are varied. For the $Ni_{1-x}Co_x(OH)_{2-y}Cl_y$ xerogel catalysts studied, the geometric current density for UOR was maximized for $Ni_{90}Co_{10}(OH)_2$ due to the optimization of the number of redox-active surface sites that could participate in the reaction. Interestingly, the current density per the number of redox-active sites was maximized for $Ni_{20}Co_{80}(OH)_2$, demonstrating that intrinsic activity of the redox-active surface sites can be increased through the addition of Co.

To determine a theoretical explanation for the maximization of intrinsic activity at $Ni_{20}Co_{80}(OH)_2$, we performed density functional theory calculations to understand how the electronic structure of β-$Ni(OH)_2$ catalysts changes with increasing Co doping. We first systematically determined the correct Hubbard potentials for Ni and Co for our model to best predict the electronic properties of β-$Co(OH)_2$ and β-$Ni(OH)_2$. The charge density difference between undoped and surface doped (2x2x4) β-$Ni(OH)_2$ supercells were determined, showing that as we increase the Co fraction in the top layer more electron density is pushed towards the Ni atoms. Projected density of states calculations showed that with increased Co incorporation in the surface layer the Ni 3d states experience a downward shift in energy and redistribution of orbital density. The projected density of states was then decomposed into each Ni 3d orbital, which demonstrated that while each state is lowered in energy with increased Co doping, unique features of the state density were enhanced for 25 and 75% Co incorporation in the surface layer. These results coincided with the two peaks in the experimentally observed intrinsic activity towards

UOR for $Ni_{80}Co_{20}(OH)_2$ and $Ni_{20}Co_{80}(OH)_2$, revealing that multiple features in the Ni 3d electronic structure will have a significant influence over UOR performance. Finally, a systematic change in the converged local magnetic moment was observed, where increasing Co in the surface layer reduces the local Ni magnetic moments and increases the local Co magnetic moments. Both changes in Ni 3d states and local magnetic moments have been linked to changes in species adsorption and may stabilize certain reaction intermediates for electrooxidation reactions. However, further experimental and theoretical work is required for UOR to expand on these ideas and validate the hypothesis presented.

6.2 Outlook

While catalyst design for UOR has come a long way since Ni-based electrodes were first proposed as more advantageous electrocatalysts as opposed to platinoid-metal catalysts, there is still a long way to go regarding experimental and theoretical developments. Thus far, the majority of the literature on UOR has explored the effect of various dopants on the UOR performance of Ni-based catalysts. However, a detailed understanding of how dopants affect intrinsic activity is needed to develop catalyst design rules for UOR. This work has aimed to address this gap for Co-doped Ni catalysts although, more work is needed both for understanding this system in particular and for serving the long-term goal of developing catalyst design rules for UOR.

As suggested above, more experiments are required to understand the effect of individual changes observed in Chapter 5. One future direction of research is to conduct more in-depth studies of product formation on Ni-based catalysts. For instance, it is well

known that Pt-based catalysts produce nitrogen oxide and carbon monoxide in addition to the classic products of urea degradation, N_2, CO_2, and H_2O. Future studies to confirm or exclude the possibility of forming CO and nitrogen oxides will be critical in understanding the progress of UOR on Ni and in tuning product selectivity. Hence, the first part of the future direction of this work will explore the product distribution as a function of reaction conditions for UOR to confirm or deny the presence of nitrogen oxides such as nitrite for UOR on Ni and Ni-Co based materials to understand how Co dopants and reaction conditions may affect product selectivity.

In addition to experimental publications which have exclusively focused on N_2, CO_2, and H_2O as degradation products, the few studies that have had a theoretical component have also only considered these species as part of their framework. Thus, the second part of the future direction of this work will be to systematically explore the UOR mechanism from an *ab-Initio* perspective. In doing so, one can determine the influence of different transition metal-doped β-$Ni(OH)_2$ surfaces on the adsorption and stabilization of different reaction intermediates.

Letters of copyright permission

SPRINGER NATURE LICENSE
TERMS AND CONDITIONS

Mar 23, 2021

This Agreement between Mr. Stephen Tatarchuk ("You") and Springer Nature ("Springer Nature") consists of your license details and the terms and conditions provided by Springer Nature and Copyright Clearance Center.

License Number	5034871383504
License date	Mar 23, 2021
Licensed Content Publisher	Springer Nature
Licensed Content Publication	Journal of Solid State Elecrochemistry
Licensed Content Title	Urea oxidation electrocatalysis on nickel hydroxide: the role of disorder
Licensed Content Author	Sankalpita Chakrabarty et al
Licensed Content Date	Jul 18, 2020
Type of Use	Thesis/Dissertation
Requestor type	academic/university or research institute
Format	print and electronic
Portion	figures/tables/illustrations
Number of figures/tables/illustrations	1

Figure 6.1: Urea oxidation electrocatalysis on nickel hydroxide: the role of disorder letter of permission

JOHN WILEY AND SONS LICENSE
TERMS AND CONDITIONS

Mar 23, 2021

This Agreement between Mr. Stephen Tatarchuk ("You") and John Wiley and Sons ("John Wiley and Sons") consists of your license details and the terms and conditions provided by John Wiley and Sons and Copyright Clearance Center.

License Number	5034920815192
License date	Mar 23, 2021
Licensed Content Publisher	John Wiley and Sons
Licensed Content Publication	Angewandte Chemie International Edition
Licensed Content Title	A Lattice-Oxygen-Involved Reaction Pathway to Boost Urea Oxidation
Licensed Content Author	Huisheng Peng, Bo Zhang, Youyong Li, et al
Licensed Content Date	Oct 11, 2019
Licensed Content Volume	58
Licensed Content Issue	47
Licensed Content Pages	6

Figure 6.2: A lattice oxygen involved reaction pathway to boost urea oxidation letter of permission

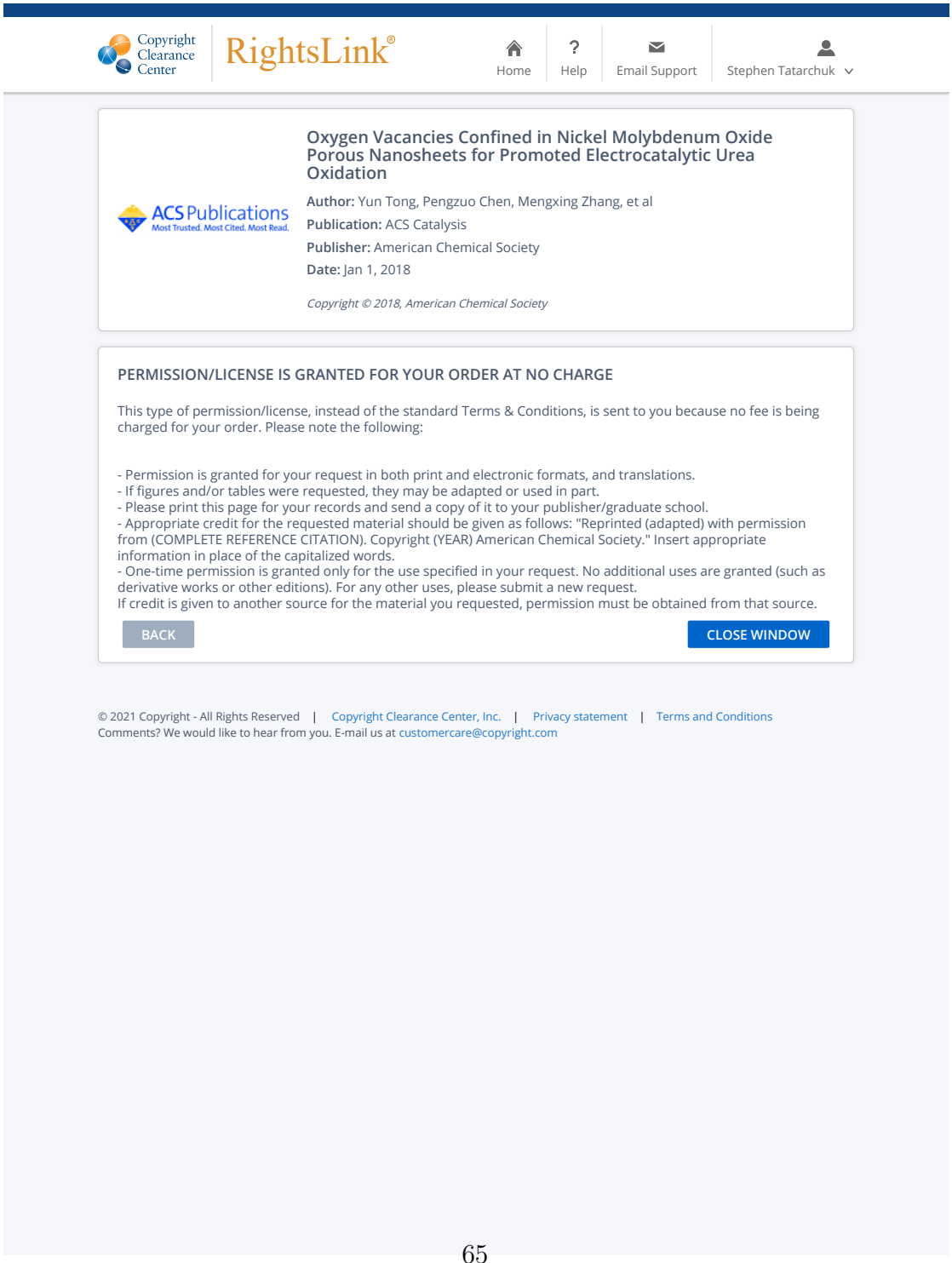

Figure 6.3: Oxygen vacancies confined in nickel molybdenum oxide porous nanosheets for promoted electrocatalytic urea oxidation letter of permission

Bibliography

(1) Glibert, P. M.; Maranger, R.; Sobota, D. J.; Bouwman, L. *Environmental Research Letters* **2014**, *9*, DOI: 10.1088/1748-9326/9/10/105001.

(2) Aspinall, D.; Lovell, B.; Payne, M.; Reid, K.; Fitts, M.; Speranzini, D.; LeBoeuf, J.; McDonald, I.; Tomecek, E.; Janovicek, K.; Van Eerd, L. *Soil Fertility Handbook* **2006**, 183–219.

(3) Meessen, J. H. *Ullmanns Encyclopedia of Industrial Chemistry* **2012**, *37*, 425–474.

(4) McKague, K.; Reid, K.; Simpson, H. *Ontario Ministry of Agriculture, Food and Rural Affairs (OMAFRA)* **2005**, *5*, 70–73.

(5) Division, B.; Ridge, O.; Ridge, O. *Toxicology* **1988**, *48*, 1–20.

(6) Likens, G. E.; Bormann, F. H.; Johnson, N. M. *Environment* **1972**, *14*, 33–40, DOI: 10.1080/00139157.1972.9933001.

(7) Manisalidis, I.; Stavropoulou, E.; Stavropoulos, A.; Bezirtzoglou, E. *Frontiers in Public Health* **2020**, *8*, 1–13, DOI: 10.3389/fpubh.2020.00014.

(8) Zhu, X.; Burger, M.; Doane, T. A.; Horwath, W. R. *Proceedings of the National Academy of Sciences of the United States of America* **2013**, *110*, 6328–6333, DOI: 10.1073/pnas.1219993110.

(9) Boening, D.; Chew, C. *Water, Air, and Soil Pollution* **1997**, *109*, 67–79, DOI: 10.1103/PhysRevA.65.054304.

(10) Shaw, W. H.; Bordeaux, J. J. *Journal of the American Chemical Society* **1955**, *77*, 4729–4733, DOI: 10.1021/ja01623a011.

(11) Cheng, F.; Basu, N. B. *Water Resources Research* **2017**, *53*, 5038–5056, DOI: 10.1002/2016WR020102.Received.

(12) Krausfeldt, L. E.; Farmer, A. T.; Castro Gonzalez, H. F.; Zepernick, B. N.; Campagna, S. R.; Wilhelm, S. W. *Frontiers in Microbiology* **2019**, *10*, 1–12, DOI: 10.3389/fmicb.2019.01064.

(13) Urbańczyk, E.; Sowa, M.; Simka, W. *Journal of Applied Electrochemistry* **2016**, *46*, 1011–1029, DOI: 10.1007/s10800-016-0993-6.

(14) Adli, N. M.; Zhang, H.; Mukherjee, S.; Wu, G. *Journal of The Electrochemical Society* **2018**, *165*, J3130–J3147, DOI: 10.1149/2.0191815jes.

(15) Guo, W.; Zhang, K.; Liang, Z.; Zou, R.; Xu, Q. *Chemical Society Reviews* **2019**, *48*, 5658–5716, DOI: 10.1039/c9cs00159j.

(16) Hu, X.; Zhu, J.; Li, J.; Wu, Q. *ChemElectroChem* **2020**, *7*, 3211–3228, DOI: 10.1002/celc.202000404.

(17) Sayed, E. T.; Eisa, T.; Mohamed, H. O.; Abdelkareem, M. A.; Allagui, A.; Alawadhi, H.; Chae, K. J. *Journal of Power Sources* **2019**, *417*, 159–175, DOI: 10.1016/j.jpowsour.2018.12.024.

(18) Ye, K.; Wang, G.; Cao, D.; Wang, G. *Topics in Current Chemistry* **2018**, *376*, 1–38, DOI: 10.1007/s41061-018-0219-y.

(19) Zhu, B.; Liang, Z.; Zou, R. *Small* **2020**, *16*, 1–19, DOI: 10.1002/smll.201906133.

(20) Medvedeva, X. V.; Medvedev, Jury, J.; Tatarchuk, S. W.; Choueiri, R. M.; Klinkova, A. *Green Chemistry* **2020**, *22*, 4456–4462, DOI: 10.1039/d0gc00964d.

(21) Wang, L.; Sofer, Z.; Pumera, M. *ACS Nano* **2020**, *14*, 21–25, DOI: 10.1021/acsnano.9b00184.

(22) Zhang, L.; Wang, L.; Lin, H.; Liu, Y.; Ye, J.; Wen, Y.; Chen, A.; Wang, L.; Ni, F.; Zhou, Z.; Sun, S.; Li, Y.; Zhang, B.; Peng, H. *Angewandte Chemie* **2019**, *131*, 16976–16981, DOI: 10.1002/ange.201909832.

(23) Wang, S.; Chen, W.; Xu, L.; Zhu, X.; Huang, Y.-C.; Zhou, W.; Wang, D.; Zhou, Y.; Du, S.; Li, Q.; Xie, C.; Tao, L.; Dong, C.-L.; Liu, J.; Wang, Y.; Chen, R.; Su, H.; Chen, C.; Zou, Y.; Li, Y.; Liu, Q. *Angewandte Chemie International Edition* **2020**, *60*, 7297–7307, DOI: 10.1002/anie.202015773.

(24) Cho, K.; Hoffmann, M. R. *Environmental Science and Technology* **2014**, *48*, 11504–11511, DOI: 10.1021/es5025405.

(25) Simka, W.; Piotrowski, J.; Robak, A.; Nawrat, G. *Journal of Applied Electrochemistry* **2009**, *39*, 1137–1143, DOI: 10.1007/s10800-008-9771-4.

(26) Bolzan, A. E.; Iwasita, T. *Electrochimica Acta* **1988**, *33*, 109–112, DOI: 10.1016/0013-4686(88)80040-9.

(27) Bezerra, Â. C.; De Sá, E. L.; Nart, F. C. *Journal of Physical Chemistry B* **1997**, *101*, 6443–6449, DOI: 10.1021/jp9700793.

(28) Vedharathinam, V.; Botte, G. G. *Journal of Physical Chemistry C* **2014**, *118*, 21806–21812, DOI: 10.1021/jp5052529.

(29) Zhang, J. Y.; He, T.; Wang, M.; Qi, R.; Yan, Y.; Dong, Z.; Liu, H.; Wang, H.; Xia, B. Y. *Nano Energy* **2019**, *60*, 894–902, DOI: 10.1016/j.nanoen.2019.04.035.

(30) Chakrabarty, S.; Offen-Polak, I.; Burshtein, T. Y.; Farber, E. M.; Kornblum, L.; Eisenberg, D. *Journal of Solid State Electrochemistry* **2021**, *25*, 159–171, DOI: 10.1007/s10008-020-04744-6.

(31) Forslund, R. P.; Mefford, J. T.; Hardin, W. G.; Alexander, C. T.; Johnston, K. P.; Stevenson, K. J. *ACS Catalysis* **2016**, *6*, 5044–5051, DOI: 10.1021/acscatal.6b00487.

(32) Lu, F.; Botte, G. G. *Electrochimica Acta* **2017**, *246*, 564–571, DOI: 10.1016/j.electacta.2017.06.055.

(33) Wang, L.; Li, M.; Huang, Z.; Li, Y.; Qi, S.; Yi, C.; Yang, B. *Journal of Power Sources* **2014**, *264*, 282–289, DOI: 10.1016/j.jpowsour.2014.04.104.

(34) Bian, L.; Du, T.; Du, Q.; Luo, M.; Li, M. *Journal of Applied Electrochemistry* **2017**, *47*, 905–915, DOI: 10.1007/s10800-017-1087-9.

(35) King, R. L.; Botte, G. G. *Journal of Power Sources* **2011**, *196*, 9579–9584, DOI: 10.1016/j.jpowsour.2011.06.079.

(36) Song, X.; Gao, L.; Li, Y.; Chen, W.; Mao, L.; Yang, J. H. *Electrochimica Acta* **2017**, *251*, 284–292, DOI: 10.1016/j.electacta.2017.08.117.

(37) Khalafallah, D.; Xiaoyu, L.; Zhi, M.; Hong, Z. *ChemElectroChem* **2020**, *7*, 163–174, DOI: 10.1002/celc.201901423.

(38) Tesfaye, R. M.; Das, G.; Park, B. J.; Kim, J.; Yoon, H. H. *Scientific Reports* **2019**, *9*, 1–9, DOI: 10.1038/s41598-018-37011-w.

(39) Ramesh, T. N.; Vishnu Kamath, P. *Journal of Solid State Electrochemistry* **2009**, *13*, 763–771, DOI: 10.1007/s10008-008-0591-6.

(40) Sun, S.; Lv, C.; Hong, W.; Zhou, X.; Wu, F.; Chen, G. *ACS Applied Energy Materials* **2019**, *2*, 312–319, DOI: 10.1021/acsaem.8b01318.

(41) Xu, W.; Zhang, H.; Li, G.; Wu, Z. *Scientific Reports* **2014**, *4*, DOI: 10.1038/srep05863.

(42) Armstrong, R. D.; Briggs, G. W.; Charles, E. A. *Journal of Applied Electrochemistry* **1988**, *18*, 215–219, DOI: 10.1007/BF01009266.

(43) Armstrong, R. D.; Charles, E. A. *Journal of Power Sources* **1989**, *25*, 89–97, DOI: 10.1016/0378-7753(89)85001-3.

(44) Hao, P.; Zhu, W.; Li, L.; Tian, J.; Xie, J.; Lei, F.; Cui, G.; Zhang, Y.; Tang, B. *Electrochimica Acta* **2020**, *338*, 135883, DOI: 10.1016/j.electacta.2020.135883.

(45) Sha, L.; Ye, K.; Wang, G.; Shao, J.; Zhu, K.; Cheng, K.; Yan, J.; Wang, G.; Cao, D. *Journal of Power Sources* **2019**, *412*, 265–271, DOI: 10.1016/j.jpowsour.2018.11.059.

(46) Yan, X.; Hu, Q. T.; Wang, G.; Zhang, W. D.; Liu, J.; Li, T.; Gu, Z. G. *International Journal of Hydrogen Energy* **2020**, *45*, 19206–19213, DOI: 10.1016/j.ijhydene.2020.05.052.

(47) Daramola, D. A.; Singh, D.; Botte, G. G. *Journal of Physical Chemistry A* **2010**, *114*, 11513–11521, DOI: 10.1021/jp105159t.

(48) Tong, Y.; Chen, P.; Zhang, M.; Zhou, T.; Zhang, L.; Chu, W.; Wu, C.; Xie, Y. *ACS Catalysis* **2018**, *8*, 1–7, DOI: 10.1021/acscatal.7b03177.

(49) He, Q.; Wan, Y.; Jiang, H.; Pan, Z.; Wu, C.; Wang, M.; Wu, X.; Ye, B.; Ajayan, P. M.; Song, L. *ACS Energy Letters* **2018**, *3*, 1373–1380, DOI: 10.1021/acsenergylett.8b00515.

(50) Jiang, Y.; Cao, L.; Hu, X.; Ren, Z.; Zhang, C.; Wang, C. *Inorganic Chemistry* **2018**, *57*, 15123–15132, DOI: 10.1021/acs.inorgchem.8b02315.

(51) Gu, H.; Shi, G.; Chen, H. C.; Xie, S.; Li, Y.; Tong, H.; Yang, C.; Zhu, C.; Mefford, J. T.; Xia, H.; Chueh, W. C.; Chen, H. M.; Zhang, L. *ACS Energy Letters* **2020**, *5*, 3185–3194, DOI: 10.1021/acsenergylett.0c01584.

(52) Anantharaj, S.; Kundu, S. *ACS Energy Letters* **2019**, *4*, 1260–1264, DOI: 10.1021/acsenergylett.9b00686.

(53) Kresse, G.; Furthmüller, J. *Physical Review B - Condensed Matter and Materials Physics* **1996**, *54*, 11169–11186, DOI: 10.1103/PhysRevB.54.11169.

(54) Kresse, G.; Furthmüller, J. *Computational Materials Science* **1996**, *6*, 15–50, DOI: 10.1016/0927-0256(96)00008-0.

(55) Larsen, A. H.; Mortensen, J. J.; Blomqvist, J.; Castelli, I. E.; Christensen, R.; Dułak, M.; Friis, J.; Groves, M. N.; Hammer, B.; Hargus, C.; Hermes, E. D.; Jennines, P. C.; Jensen, P. B.; Kermode, J.; Kitchin, J. R.; Kolsbjerg, E. L.; Kubal, J.; Kaasbjerg, K.; Lysgaard, S.; Maronsson, J. B.; Maxson, T.; Olsen, T.; Pastewka, L.; Peterson, A.; Rostgaard, C.; Schiøtz, J.; Schütt, O.; Strange, M.; Thygesen, K. S.; Vegge, T.; Vilhelmsen, L.; Walter, M.; Zeng, Z. *J. Phys.: Condens. Matter* **2017**, *29*, 0–30, DOI: 10.1088/1361-648X/aa680e.

(56) Kresse, G.; Hafner, J. *Phys. Rev. B* **1993**, *47*, 558–561, DOI: 10.1103/PhysRevB.47.558.

(57) Kresse, G.; Hafner, J. *Phys. Rev. B* **1994**, *49*, 251–269, DOI: 10.1103/PhysRevB.49.14251.

(58) Majewski, J.; Vogl, P. *Physical Review B - Condensed Matter and Materials Physics* **1992**, *46*, 219–234, DOI: 10.1103/PhysRevB.46.12219.

(59) Szotek, Z.; Temmerman, W. *Physical Review B - Condensed Matter and Materials Physics* **1993**, *47*, 4029–4032, DOI: 10.1103/PhysRevB.47.4029.

(60) Wellendorff, J.; Lundgaard, K. T.; Møgelhøj, A.; Petzold, V.; Landis, D. D.; Nørskov, J. K.; Bligaard, T.; Jacobsen, K. W. *Physical Review B - Condensed Matter and Materials Physics* **2012**, *85*, 32–34, DOI: 10.1103/PhysRevB.85.235149.

(61) Yu, L.; Ranjan, V.; Lu, W.; Bernholc, J.; Nardelli, M. B. *Physical Review B - Condensed Matter and Materials Physics* **2008**, *77*, 1–6, DOI: 10.1103/PhysRevB.77.245102.

(62) Cococcioni, M.; De Gironcoli, S. *Physical Review B - Condensed Matter and Materials Physics* **2005**, *71*, 1–16, DOI: 10.1103/PhysRevB.71.035105.

(63) Calculate U for LSDA+U, 2019.

(64) Li, Y. F.; Selloni, A. *ACS Catalysis* **2014**, *4*, 1148–1153, DOI: 10.1021/cs401245q.

(65) Alidoust, N.; Toroker, M. C.; Keith, J. A.; Carter, E. A. *ChemSusChem* **2014**, *7*, 195–201, DOI: 10.1002/cssc.201300595.

(66) Wang, L.; Maxisch, T.; Ceder, G. *Physical Review B - Condensed Matter and Materials Physics* **2006**, *73*, 1–6, DOI: 10.1103/PhysRevB.73.195107.

(67) Zaffran, J.; Toroker, M. C. *ChemPhysChem* **2016**, *17*, 1630–1636, DOI: 10.1002/cphc.201600049.

(68) Wang, H.; Song, C. *European Physical Journal B* **2019**, *92*, 1–8, DOI: 10.1140/epjb/e2019-90369-6.

(69) Chen, W.; Xu, L.; Zhu, X.; Huang, Y.-C.; Zhou, W.; Wang, D.; Zhou, Y.; Du, S.; Li, Q.; Xie, C.; Tao, L.; Dong, C.-L.; Liu, J.; Wang, Y.; Chen, R.; Su, H.; Chen, C.; Zou, Y.; Li, Y.; Liu, Q.; Wang, S. *Computer Physics Communications* **2020**, 1–26.

(70) Momma, K.; Izumi, F. *Journal of Applied Crystallography* **2011**, *44*, 1272–1276, DOI: 10.1107/S0021889811038970.

(71) Zhang, W.; Yin, S.; Li, X.; Xu, G.; Xie, T. *Electrochemistry Communications* **2016**, *63*, 1–4, DOI: 10.1016/j.elecom.2015.12.004.

(72) Bette, S.; Dinnebier, R. E.; Röder, C.; Freyer, D. *Journal of Solid State Chemistry* **2015**, *228*, 131–140, DOI: 10.1016/j.jssc.2015.04.015.

(73) Cui, H.; Zayat, M.; Levy, D. *Journal of Nanoparticle Research* **2009**, *11*, 1331–1338, DOI: 10.1007/s11051-008-9518-5.

(74) Hall, D. S.; Lockwood, D. J.; Bock, C.; MacDougall, B. R. *Proceedings of the Royal Society A: Mathematical, Physical and Engineering Sciences* **2015**, *471*, DOI: 10.1098/rspa.2014.0792.

(75) Davidson, A.; Tempere, J. F.; Che, M.; Roulet, H.; Dufour, G. *Journal of Physical Chemistry* **1996**, *100*, 4919–4929, DOI: 10.1021/jp952268w.

(76) Poul, L.; Jouini, N.; Fievet, F. *Chemistry of Materials* **2000**, *12*, 3123–3132, DOI: 10.1021/cm991179j.

(77) Kimura, E.; Sakonaka, A.; Machida, R.; Kodama, M. *Journal of the American Chemical Society* **1982**, *104*, 4257–4258, DOI: 10.1021/ja00379a039.

(78) Frolova, Y. V.; Avdeev, V. I.; Ruzankin, S. P.; Zhidomirov, G. M.; Fedotov, M. A.; Sadykov, V. A. *Journal of Physical Chemistry B* **2004**, *108*, 6969–6980, DOI: 10.1021/jp0363500.

(79) Jayashree, R. S.; Kamath, P. V. *Journal of Materials Chemistry* **1999**, *9*, 961–963, DOI: 10.1039/A807000H.

(80) Khassin, A. A.; Anufrienko, V. F.; Ikorskii, V. N.; Plyasova, L. M.; Kustova, G. N.; Larina, T. V.; Molina, I. Y.; Parmon, V. N. *Physical Chemistry Chemical Physics* **2002**, *4*, 4236–4243, DOI: 10.1039/b201967a.

(81) Ma, R.; Liu, Z.; Takada, K.; Fukuda, K.; Ebina, Y.; Bando, Y.; Sasaki, T. *Inorganic Chemistry* **2006**, *45*, 3964–3969, DOI: 10.1021/ic052108r.

(82) Klaus, S.; Cai, Y.; Louie, M. W.; Trotochaud, L.; Bell, A. T. *Journal of Physical Chemistry C* **2015**, *119*, 7243–7254, DOI: 10.1021/acs.jpcc.5b00105.

(83) Audemer, A.; Delahaye, A.; Farhi, R.; Sac-Epée, N.; Tarascon, J.-M. *Journal of The Electrochemical Society* **1997**, *144*, 2614–2620, DOI: 10.1149/1.1837873.

(84) Bernard, M.; Cortes, R.; Keddam, M.; Takenouti, H.; Bernard, P.; Senyarich, S. *Journal of Power Sources* **1996**, *2*, 247–254, DOI: 10.1016/S0378-7753(96)02482-2.

(85) Nesbitt, H. W.; Legrand, D.; Bancroft, G. *Phys Chem Minerals* **2000**, 357–366, DOI: 10.1007/s002690050265.

(86) Ismail, K. M.; Badawy, W. A. *Journal of Applied Electrochemistry* **2000**, *30*, 1303–1311, DOI: 10.1023/A:1026560422090.

(87) Zheng, X.; Zhang, B.; De Luna, P.; Liang, Y.; Comin, R.; Voznyy, O.; Han, L.; García De Arquer, F. P.; Liu, M.; Dinh, C. T.; Regier, T.; Dynes, J. J.; He, S.; Xin, H. L.; Peng, H.; Prendergast, D.; Du, X.; Sargent, E. H. *Nature Chemistry* **2018**, *10*, 149–154, DOI: 10.1038/nchem.2886.

(88) Kuznetsov, D. A.; Han, B.; Yu, Y.; Rao, R. R.; Hwang, J.; Román-Leshkov, Y.; Shao-Horn, Y. *Joule* **2018**, *2*, 225–244, DOI: 10.1016/j.joule.2017.11.014.

(89) Huang, Z. F.; Song, J.; Du, Y.; Xi, S.; Dou, S.; Nsanzimana, J. M. V.; Wang, C.; Xu, Z. J.; Wang, X. *Nature Energy* **2019**, *4*, 329–338, DOI: 10.1038/s41560-019-0355-9.

(90) Hall, D. S.; Lockwood, D. J.; Poirier, S.; Bock, C.; MacDougall, B. R. *ACS Applied Materials and Interfaces* **2014**, *6*, 3141–3149, DOI: 10.1021/am405419k.

(91) Liu, Z.; Ma, R.; Osada, M.; Takada, K.; Sasaki, T. *Journal of the American Chemical Society* **2005**, *127*, 13869–13874, DOI: 10.1021/ja0523338.

(92) Hermet, P.; Gourrier, L.; Bantignies, J. L.; Ravot, D.; Michel, T.; Deabate, S.; Boulet, P.; Henn, F. *Physical Review B - Condensed Matter and Materials Physics* **2011**, *84*, 1–10, DOI: 10.1103/PhysRevB.84.235211.

(93) Szytula, A.; Murasik, A.; Balanda, M. *Physica Status Solidi b* **1971**, *125*, 125–128.

(94) Perdew, J. P.; Burke, K.; Ernzerhof, M. *Physical Review Letters* **1996**, *77*, 3865–3868, DOI: 10.1103/PhysRevLett.77.3865.

(95) Alidoust, N.; Toroker, M. C.; Keith, J. A.; Carter, E. A. *ChemSusChem* **2014**, *7*, 195–201, DOI: 10.1002/cssc.201300595.

(96) Doyle, A. D.; Bajdich, M.; Vojvodic, A. *Catalysis Letters* **2017**, *147*, 1533–1539, DOI: 10.1007/s10562-017-2010-z.

(97) Li, Y. F.; Selloni, A. *ACS Catalysis* **2014**, *4*, 1148–1153, DOI: 10.1021/cs401245q.

(98) Kalasina, S.; Pattanasattayavong, P.; Suksomboon, M.; Phattharasupakun, N.; Wutthiprom, J.; Sawangphruk, M. *Chemical Communications* **2017**, *53*, 709–712, DOI: 10.1039/C6CC08131B.

(99) Chen, J.; Selloni, A. *Journal of Physical Chemistry C* **2013**, *117*, 20002–20006, DOI: 10.1021/jp406331h.

(100) Dalverny, A. L.; Filhol, J. S.; Lemoigno, F.; Doublet, M. L. *Journal of Physical Chemistry C* **2010**, *114*, 21750–21756, DOI: 10.1021/jp108599m.

(101) Hunt, D.; Garbarino, G.; Rodríguez-Velamazán, J. A.; Ferrari, V.; Jobbagy, M.; Scherlis, D. A. *Physical Chemistry Chemical Physics* **2016**, *18*, 30407–30414, DOI: 10.1039/c6cp06006d.

(102) Biz, C.; Fianchini, M.; Gracia, J. *ACS Applied Nano Materials* **2020**, *3*, 506–515, DOI: 10.1021/acsanm.9b02067.

(103) Gracia, J. *Journal of Physical Chemistry C* **2019**, *123*, 9967–9972, DOI: 10.1021/acs.jpcc.9b01635.

(104) Munarriz, J.; Polo, V.; Gracia, J. *ChemPhysChem* **2018**, *19*, 2843–2847, DOI: 10.1002/cphc.201800633.

(105) Xie, J.; Liu, W.; Lei, F.; Zhang, X.; Qu, H.; Gao, L.; Hao, P.; Tang, B.; Xie, Y. *Chemistry - A European Journal* **2018**, *24*, 18408–18412, DOI: 10.1002/chem.201803718.

(106) Xie, J.; Gao, L.; Cao, S.; Liu, W.; Lei, F.; Hao, P.; Xia, X.; Tang, B. *Journal of Materials Chemistry A* **2019**, *7*, 13577–13584, DOI: 10.1039/c9ta02891a.

(107) Babar, P.; Lokhande, A.; Karade, V.; Pawar, B.; Gang, M. G.; Pawar, S.; Kim, J. H. *ACS Sustainable Chemistry and Engineering* **2019**, *7*, 10035–10043, DOI: 10.1021/acssuschemeng.9b01260.

(108) Liu, M.; Jiao, Y.; Zhan, S.; Wang, H. *Catalysis Today* **2019**, DOI: 10.1016/j.cattod.2019.05.032.

(109) Xie, L.; Liu, Q.; Luo, Y.; Liu, Z.; Xu, Y.; Asiri, A. M.; Sun, X.; Xie, F. *ChemistrySelect* **2017**, *2*, 10285–10289, DOI: 10.1002/slct.201702071.

(110) Zeng, M.; Wu, J.; Li, Z.; Wu, H.; Wang, J.; Wang, H.; He, L.; Yang, X. *ACS Sustainable Chemistry and Engineering* **2019**, *7*, 4777–4783, DOI: 10.1021/acssuschemeng.8b04953.

(111) Zhu, W.; Yue, Z.; Zhang, W.; Hu, N.; Luo, Z.; Ren, M.; Xu, Z.; Wei, Z.; Suo, Y.; Wang, J. *Journal of Materials Chemistry A* **2018**, *6*, 4346–4353, DOI: 10.1039/c7ta10584c.

(112) Periyasamy, S.; Subramanian, P.; Levi, E.; Aurbach, D.; Gedanken, A.; Schechter, A. *ACS Applied Materials and Interfaces* **2016**, *8*, 12176–12185, DOI: 10.1021/acsami.6b02491.

(113) Wu, M. S.; Sie, Y. J.; Yang, S. B. *Electrochimica Acta* **2019**, *304*, 131–137, DOI: 10.1016/j.electacta.2019.02.100.

Appendices

Appendix A

Experimental

A.1 EDX-SEM of $Ni_{1-x}Co_x(OH)_{2-y}Cl_y$

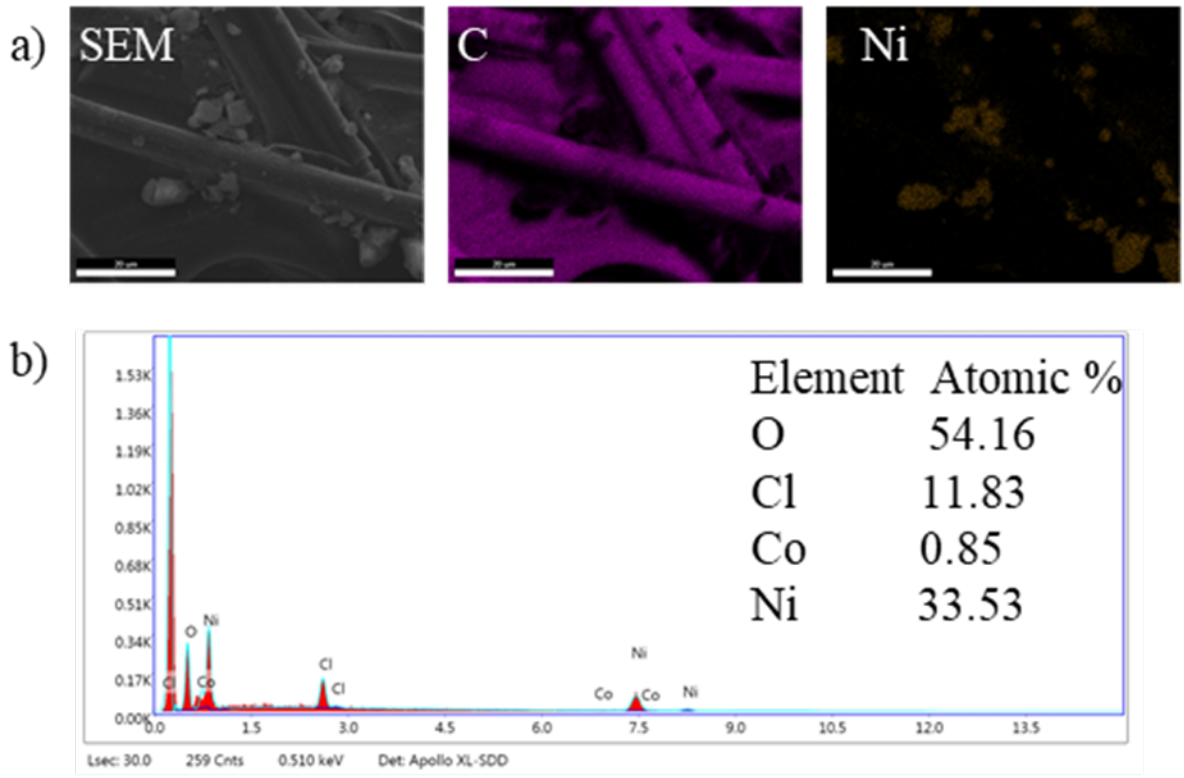

Figure A.1: a)EDX-SEM Mapping and b)Selected area EDX spectrum for $Ni(OH)_{2-y}Cl_y$.

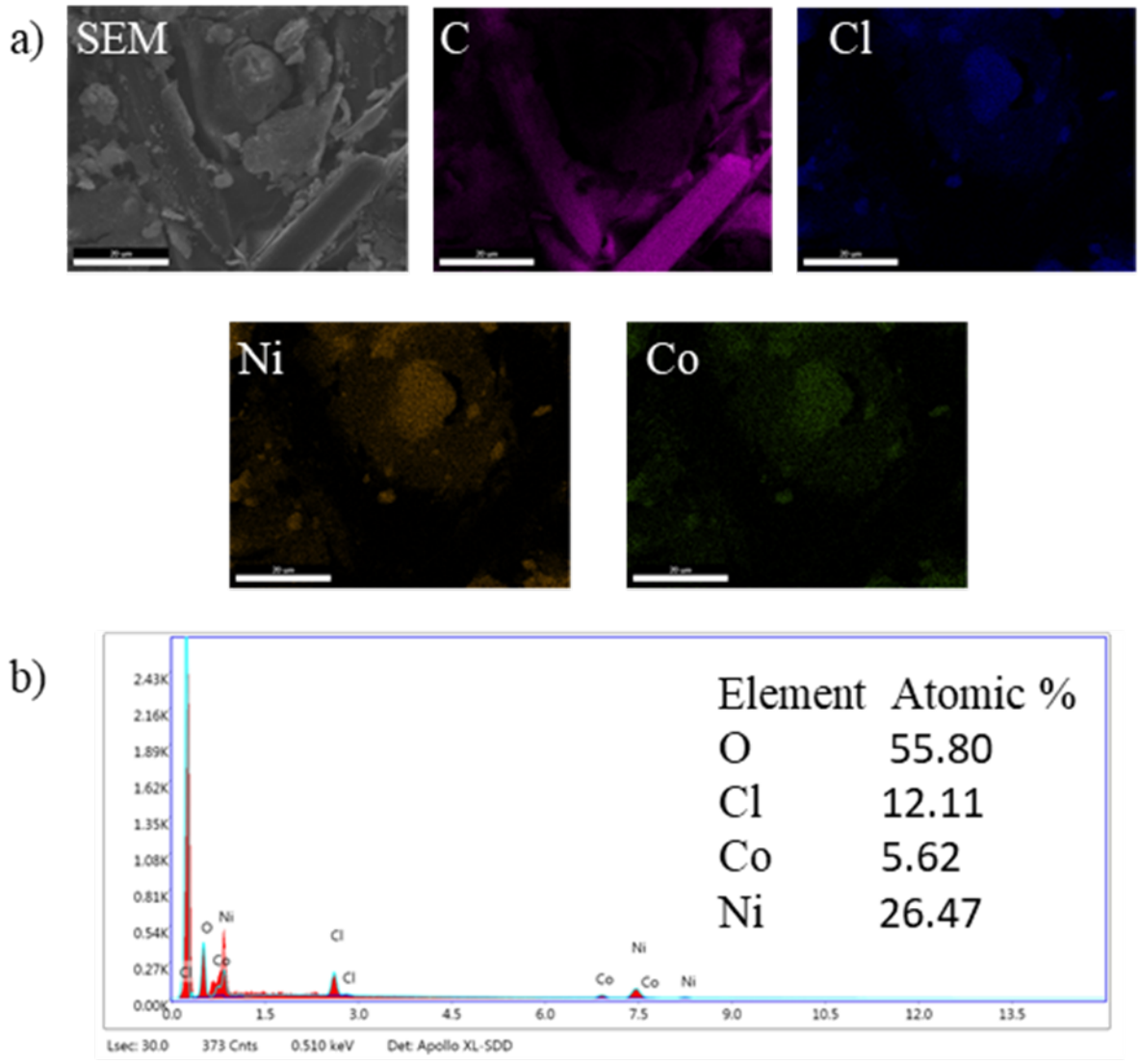

Figure A.2: a)EDX-SEM Mapping and b)Selected area EDX spectrum for $Ni_{80}Co_{20}(OH)_{2-y}Cl_y$.

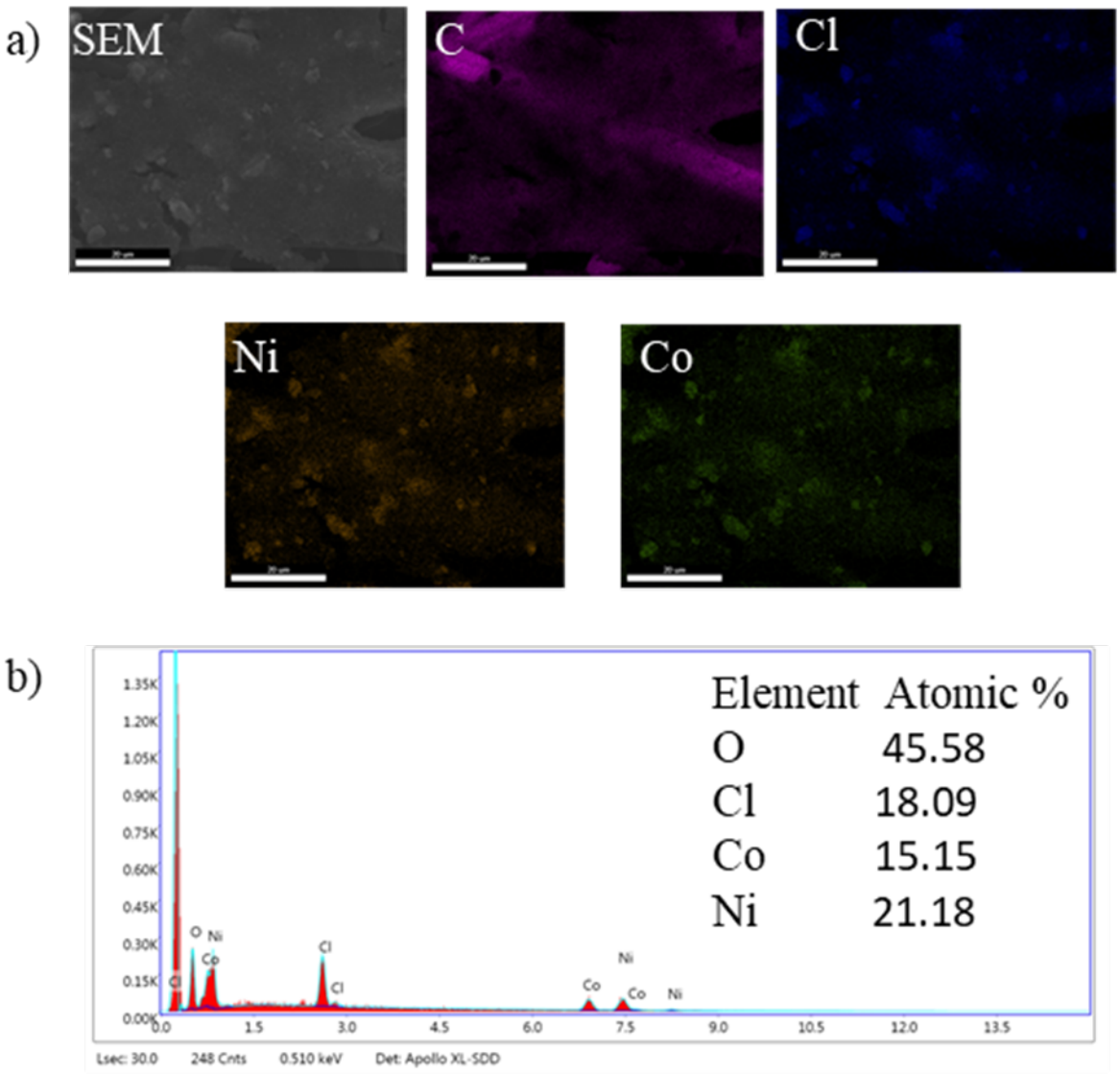

Figure A.3: a)EDX-SEM Mapping and b)Selected area EDX spectrum for $Ni_{60}Co_{40}(OH)_{2-y}Cl_y$.

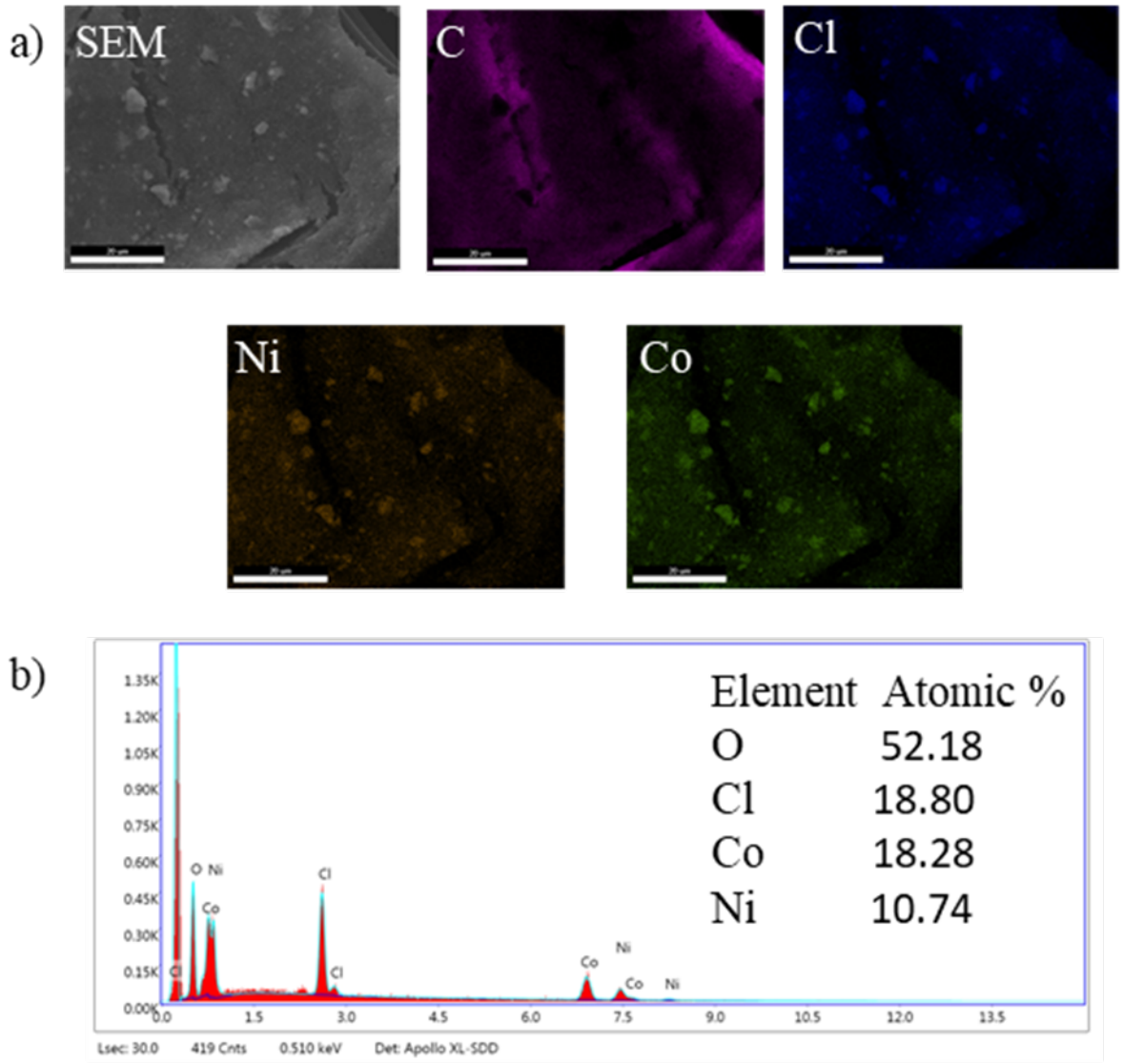

Figure A.4: a)EDX-SEM Mapping and b)Selected area EDX spectrum for $Ni_{40}Co_{60}(OH)_{2-y}Cl_y$.

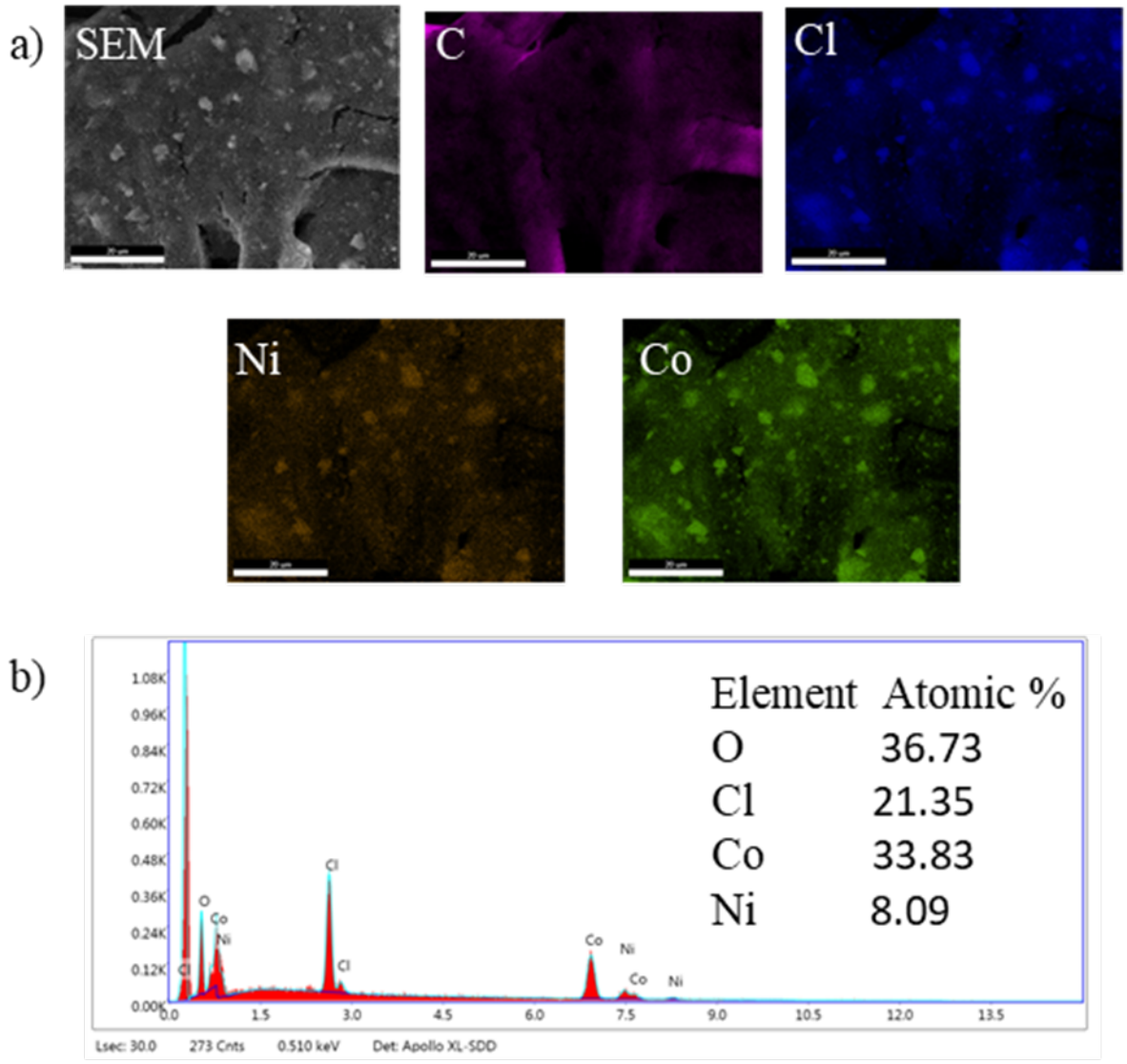

Figure A.5: a)EDX-SEM Mapping and b)Selected area EDX spectrum for $Ni_{20}Co_{80}(OH)_{2-y}Cl_y$.

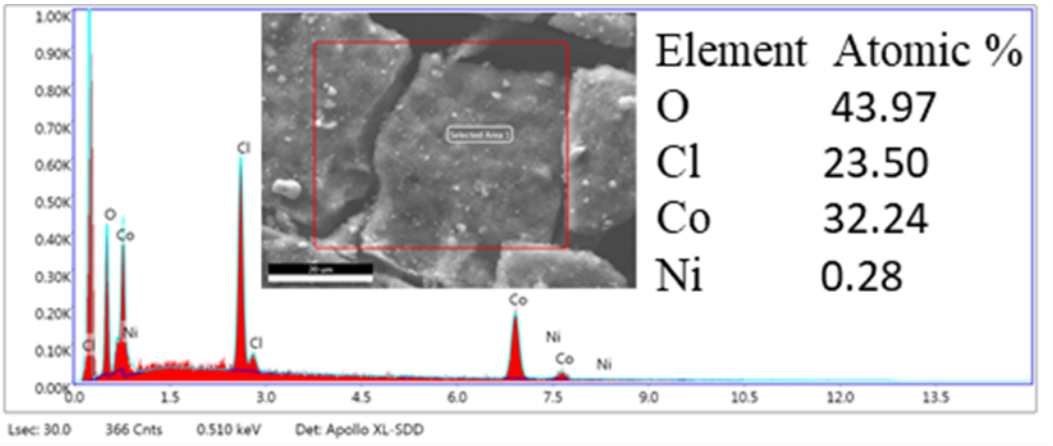

Figure A.6: a)EDX-SEM Mapping and b)Selected area EDX spectrum for $Co(OH)_{2-y}Cl_y$.

A.2 PXRD of $Ni_{1-x}Co_x(OH)_{2-y}Cl_y$

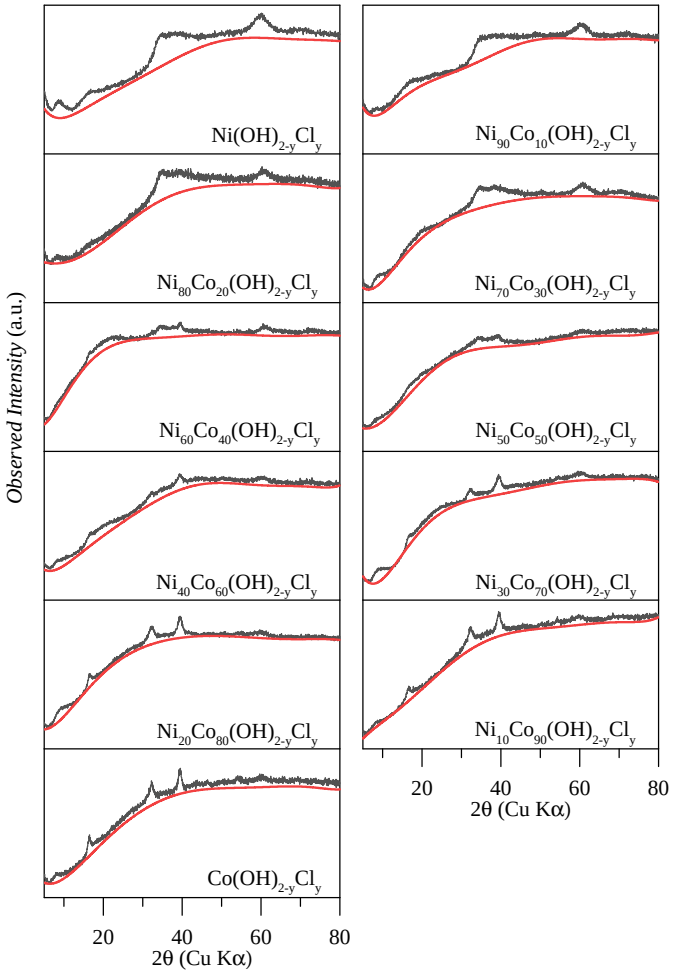

Figure A.7: Raw PXRD Intensity with backgrounds for all $Ni_{1-x}Co_x(OH)_{2-y}Cl_y$ compositions.

A.3 UV-Vis Spectroscopy of $Ni_{1-x}Co_x(OH)_{2-y}Cl_y$

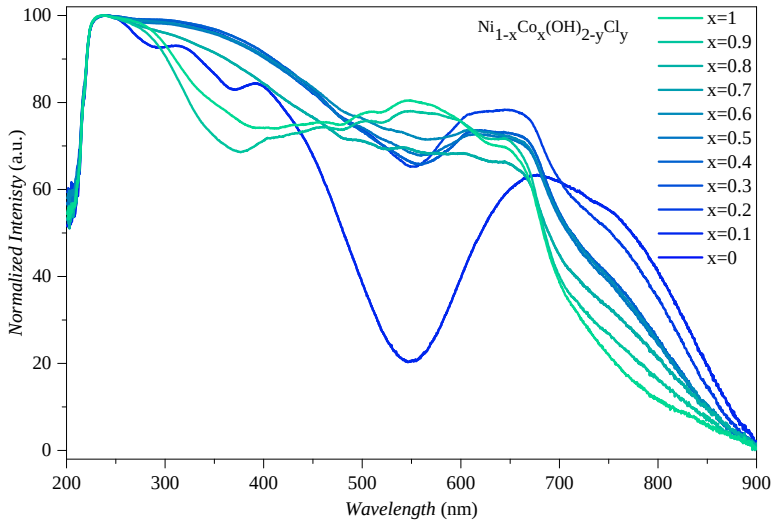

Figure A.8: Normalized UV-Vis Absorbance for all $Ni_{1-x}Co_x(OH)_{2-y}Cl_y$ compositions.

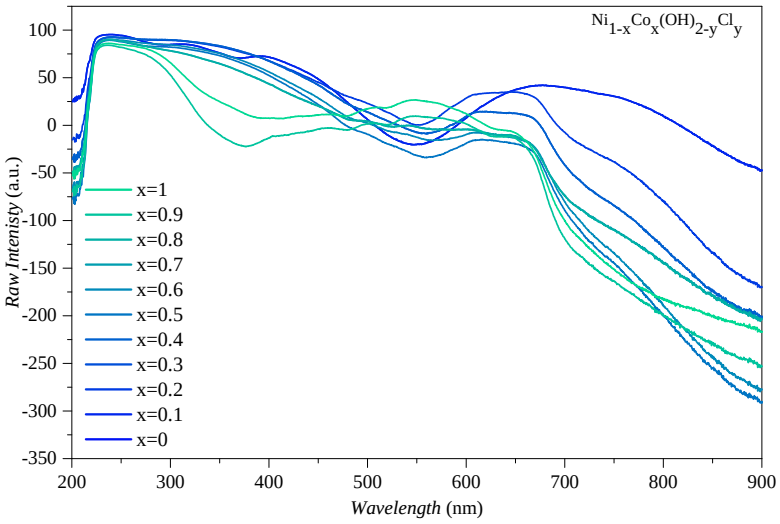

Figure A.9: Raw UV-Vis Absorbance for all $Ni_{1-x}Co_x(OH)_{2-y}Cl_y$ compositions.

A.4 Raman Spectroscopy of $Ni_{1-x}Co_x(OH)_{2-y}Cl_y$

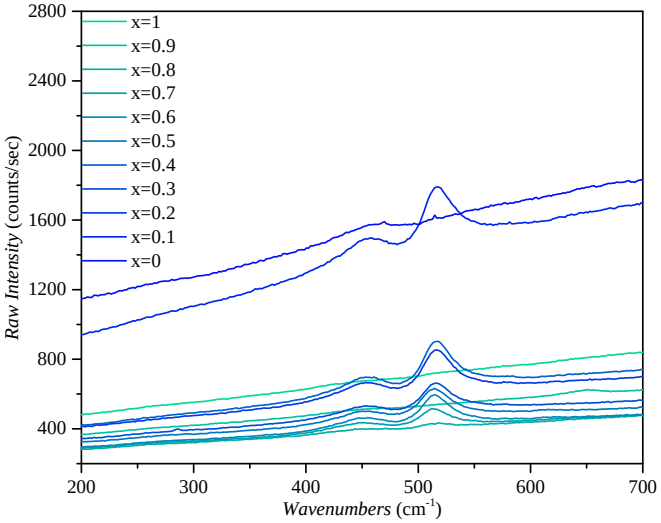

Figure A.10: Raw Raman Spectra with backgrounds for all $Ni_{1-x}Co_x(OH)_{2-y}Cl_y$ compositions.

A.5 Electrochemistry of $Ni_{1-x}Co_x(OH)_{2-y}Cl_y$

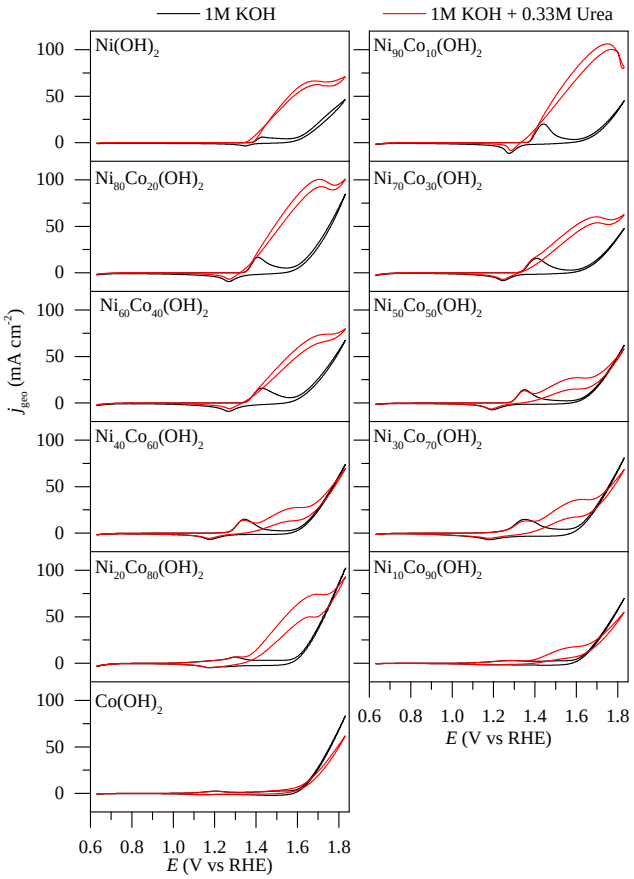

Figure A.11: CV of all $Ni_{1-x}Co_x(OH)_{2-y}Cl_y$ compositions at 20 mV/s under OER and UOR conditions.

Table A.1: Performance of Ni-based catalysts for UOR reported in the literature

Material Composition	Onset (V vs RHE)	Peak current density (mA cm^{-2} @ V vs RHE)	CA (mA cm^{-2} @ V vs RHE)	Tafel Slope (mV/dec)	Electrolyte	Reference
NiClOH xerogel/GCE	1.34	∼250 @ 1.60	-	41	1 M KOH, 0.33 M Urea	[22]
$\alpha-Ni(OH)_2$ xerogel/GCE	1.32	∼90 @1.58	∼40 @1.46	29.7	1 M KOH, 0.33 M Urea	[49]
β-$Ni(OH)_2$/NF	1.49	100 @1.74	-	38	1 M KOH, 0.33 M Urea	[105]
NF	1.35	∼75 @ 1.6	84.0 @ 1.60	45.7	1 M KOH, 0.33 M Urea	[106]
α-$Ni(OH)_2$/NF	1.33	∼200 @ 1.6	216 @ 1.60	35.3	1 M KOH, 0.33 M Urea	[106]
NF	1.4	∼40 @1.57	-	64	1 M KOH, 0.33 M Urea	[107]
Ni_2P/CB/GCE	1.32	∼90 @ 1.50	Unstable over 2 hr	75	1 M KOH, 0.33 M Urea	[108]
NiF_2/CB/GCE	-	-	Unstable over 2 hr	-	1 M KOH, 0.33 M Urea	[108]
NiF_2/Ni_2P/CB/GCE	1.32	∼140 @ 1.50	∼11 @ 1.38	48	1 M KOH, 0.33 M Urea	[108]
Ni_2P NS/CC	1.42	∼80 @ 1.57		117	1 M KOH, 0.33 M Urea	[109]

Table A.2: Performance of Ni-Co based catalysts for UOR reported in the literature

Material Composition	Onset (V vs RHE)	Peak current density (mA cm^{-2} @ V vs RHE)	CA (mA cm^{-2} @ V vs RHE)	Tafel Slope (mV/dec)	Electrolyte	Reference
$NiCo_{25}$ aerogel/MWCNT/CPE	1.33	∼100 @ 1.57	∼180 @ 1.57	-	1 M KOH, 1 M Urea	38
$NiCo_{50}$ aerogel/MWCNT/CPE	1.39	∼50 @ 1.57	∼45 @ 1.57	-	1 M KOH, 1 M Urea	38
$NiCo_{100}$ aerogel/MWCNT/CPE	1.43	∼55 @ 1.57	-	-	1 M KOH, 1 M Urea	38
$NiCo_{200}$ aerogel/MWCNT/CPE	1.45	∼20 @ 1.57	∼50 @ 1.57	-	1 M KOH, 1 M Urea	38
NiCo LDH-NO3 /Rotation ring disk electrode	1.34	∼110 @ 1.67	∼7 @ 1.37	91	1 M KOH, 0.33 M Urea	110
Ni_2P NS/CC	1.42	∼80 @ 1.57	-	117	1 M KOH, 0.33M Urea	109
NiCoP NS/CC	1.32	∼140 @ 1.57	∼50 @ 1.42 ∼20 @1.35	64	1 M KOH, 0.33 M Urea	109
Ni/CC	1.41	∼21 @ 1.57	-	-	1 M KOH, 0.33 M Urea	41
Ni_4Co/CC	1.35	∼18 @ 1.57	-	-	1 M KOH, 0.33 M Urea	41
Ni_3Co_2/CC	1.28	∼15 @ 1.57	-	-	1 M KOH, 0.33 M Urea	41
Ni_2Co_3/CC	1.35	∼11 @ 1.57	-	-	1 M KOH, 0.33 M Urea	41
$NiCo_4$/CC	1.38	∼8 @ 1.57	-	-	1 M KOH, 0.33 M Urea	41
Mesoporous $NiCo_2O_4$	1.42	136 mg-1 @ 1.67	∼100 @ 1.67	-	1 M KOH, 0.33 M Urea	**Ding2014a**

Table A.3: Performance of Ni-M (excluding Co) catalysts for UOR reported in the literature

Material Composition	Onset (V vs RHE)	Peak current density (mA cm^{-2} @ V vs RHE)	CA (mA cm^{-2} @ V vs RHE)	Tafel Slope (mV/dec)	Electrolyte	Reference
NiFe LDH/NF	1.36	100 @ 1.48	-	-	1 M KOH, 0.33 M Urea	[111]
$Fe_{11.1\%}Ni_3S_2$/NF	1.36	100 @ 1.45	-	-	1 M KOH, 0.33 M Urea	[111]
$Ni(OH)_2$/NF	1.49	100 @ 1.74	-	38	1 M KOH, 0.33 M Urea	[111]
NiFe LDH/Ni-Fe alloy foam	1.36	100 @ 1.46	-	33	1 M KOH, 0.33 M Urea	[111]
Bare NF	1.4	∼40 @ 1.57	-	64	1 M KOH, 0.33 M Urea	[107]
NiFe LDH/NF	1.37	∼200 @ 1.57	-	42	1 M KOH, 0.33 M Urea	[107]
NiFeCo LDH/NF	1.32	∼270 @ 1.57	-	31	1 M KOH, 0.33 M Urea	[107]
$Ni_{1.5}Mn_{1.5}O_4$/CB/GCE	1.32	6.9 @ 1.53	-	-	1 M KOH, 0.33 M Urea	[112]
$NiMn_2O_4$/CB/GCE	1.37	1.81 @ 1.53	-	-	1 M KOH, 0.33 M Urea	[112]
$MnNi_2O_4$/CB/GCE	1.37	1.79 @ 1.53	-	-	1 M KOH, 0.33 M Urea	[112]
EC-Dep CuNi/NF	1.36	∼85 @ 1.57	∼80 @ 1.57	-	1 M KOH, 0.33 M Urea	[113]
EC-Dep Ni/NF	1.36	∼60 @ 1.57	∼60 @ 1.57	-	1 M KOH, 0.33 M Urea	[113]

Appendix B

Theoretical

B.1 Local magnetic moment of optimized supercell structures

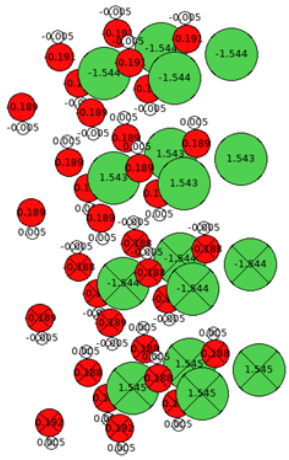

Figure B.1: Local magnetic moment of optimized supercell structure for $Ni(OH)_2$ surface layer. The net magnetic moment of the supercell was 0.0000 μB.

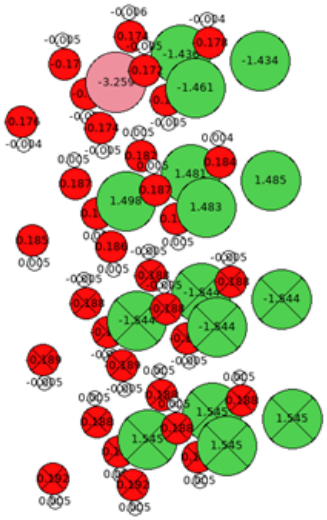

Figure B.2: Local magnetic moment of optimized supercell structure for $Ni_{75}Co_{25}(OH)_2$ surface layer. The net magnetic moment of the supercell was -0.9976 μB.

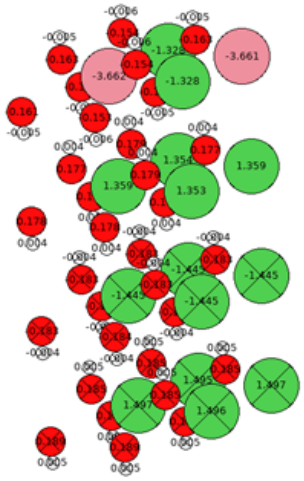

Figure B.3: Local magnetic moment of optimized supercell structure for $Ni_{50}Co_{50}(OH)_2$ surface layer. The net magnetic moment of the supercell was -1.9944 μB.

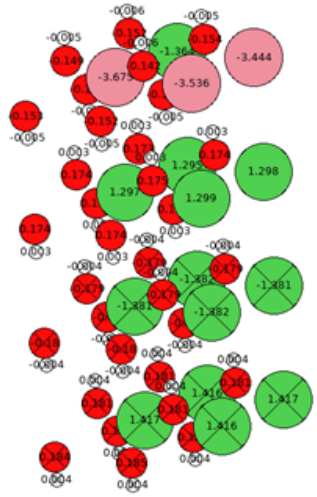

Figure B.4: Local magnetic moment of optimized supercell structure for $Ni_{25}Co_{75}(OH)_2$ surface layer. The net magnetic moment of the supercell was -2.9942 μB.

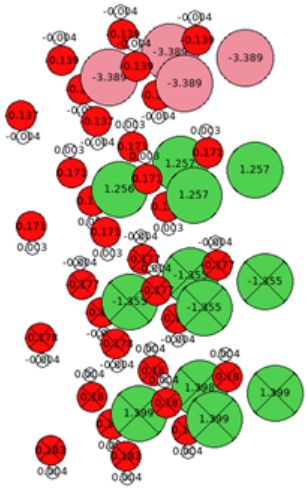

Figure B.5: Local magnetic moment of optimized supercell structure for $Co(OH)_2$ surface layer. The net magnetic moment of the supercell was -3.9980 μB.

B.2 POSCAR Files of Optimized Structures

Optimized 2x2x4 Supercell β-Ni$(OH)_2$

Total Free Energy: -274.8217765eV

Ni H O

1.00000000000000

6.3506889969999998 -0.0001849620000000 0.0000076420000000

-3.1755045220000002 5.5010339200000002 0.0001355020000000

0.0000767550000000 0.0012980790000000 35.6450547760000021

Ni H O

16 32 32

Selective dynamics

Direct

0.0832709983956406 0.4169261037169747 0.2933282873326348 F F F

0.0830915718456211 0.4169862823127133 0.4311645180269679 F F F

0.0828147780017900 0.4170501264148001 0.5688604768158712 T T T

0.0826600951353598 0.4168448813290411 0.7067808716613087 T T T

0.0832716307480439 0.9169266563467389 0.2933283504247086 F F F

0.0830922041980244 0.9169868349424704 0.4311645811190417 F F F

0.0828138356954256 0.9170506789916146 0.5688605399082789 T T T

0.0826607274877631 0.9168454339587981 0.7067809347533824 T T T

0.5832720902263233 0.4169265547851069 0.2933281801348926 F F F

0.5830926636763039 0.4169867333808455 0.4311644108292256 F F F

0.5828142951737050 0.4170505774299826 0.5688603696184629 T T T

0.5826611869295562 0.4168453323309720 0.7067810450073893 T T T

0.5832711479199588 0.9169271073619214 0.2933282432273003 F F F

0.5830923870475715 0.9169854681399485 0.4311644739283977 F F F

0.5828149275261083 0.9170511300597468 0.5688604327105367 T T T

0.5826618193184530 0.9168458850269303 0.7067808275556331 T T T

0.4169075361928378 0.0839766857310451 0.2376707088324608 F F F

0.4160274018754180 0.0830134106967648 0.3754480293644065 F F F

0.2493265147581241 0.2500081263314300 0.3489253781823294 F F F

0.4166248660463197 0.0839880206902421 0.5131498759239861 T T T

0.2496389458473232 0.2501355808864005 0.4867644139537148 F F F

0.4158554688957281 0.0831265433270758 0.6509487979197175 T T T

0.2491463147831254 0.2500921334561426 0.6245947536888039 T T T

0.2494009643958464 0.2501796079516723 0.7623729116145910 T T T

0.4169081685452483 0.5839772383608093 0.2376707719245275 F F F

0.4160280342278284 0.5830139633265290 0.3754480924564731 F F F

0.2493271471105345 0.7500086789611871 0.3489254412743961 F F F

0.4166239237399552 0.5839885732670567 0.5131499390163938 T T T

0.2496395781997265 0.7501361335161647 0.4867644770457815 F F F

0.4158561012481314 0.5831270959568329 0.6509488610117842 T T T

0.2491460381543931 0.7500908682152456 0.6245948167879760 T T T

0.2494015967482497 0.7501801605814293 0.7623729747066577 T T T

0.9169086280235277 0.0839771367991773 0.2376706016347114 F F F

0.9160284937061078 0.0830138617648970 0.3754479221666571 F F F

0.7493276065888139 0.2500085773995622 0.3489252709845871 F F F

0.9166243832182346 0.0839884717054318 0.5131497687265778 T T T

0.7496400376780059 0.2501360319545327 0.4867643067559726 F F F

0.9158549860676430 0.0831269943422583 0.6509486907223092 T T T

0.7491449229739047 0.2500907666006711 0.6245946464985010 T T T

0.7494020561900356 0.2501800589536032 0.7623730849606716 T T T

0.9169076857171632 0.5839776893759918 0.2376706647271192 F F F

0.9160275513997433 0.5830144143417115 0.3754479852590649 F F F

0.7493266642824494 0.7500091299763767 0.3489253340769949 F F F

0.9166250155706450 0.5839890243351888 0.5131498318186445 T T T

0.7496397610492807 0.7501347667136429 0.4867643698551447 F F F

0.9158556184200464 0.5831275469720225 0.6509487538143759 T T T

0.7491455553263080 0.7500913192304353 0.6245947095905677 T T T

0.7494002049025426 0.7501787936597637 0.7623731480601847 T T T

0.4162824989211416 0.0837066994726783 0.2647013880505185 F F F

0.2494804986155543 0.2503217235234914 0.3219005903197925 F F F

0.4163188275459930 0.0834142379158678 0.4024801085550607 F F F

0.2491290415962339 0.2498583593814274 0.4597326148838476 F F F

0.4165948265854951 0.0833617589711011 0.5401755065799918 T T T

0.2498653134829709 0.2500367289014633 0.5975666005819704 T T T

0.4166245264947293 0.0834055919814958 0.6779780720326514 T T T

0.2498301726130236 0.2501587277824697 0.7353652381378453 T T T

0.4162831312735449 0.5837072521024425 0.2647014511425851 F F F

0.2494811309679577 0.7503222761532555 0.3219006534118662 F F F

0.4163194598984035 0.5834147905456319 0.4024801716471273 F F F

0.2491296739486444 0.7498589120111916 0.4597326779759143 F F F

0.4165938843156169 0.5833623116141240 0.5401752891285696 T T T

0.2498650368907320 0.7500354637267677 0.5975663831373197 T T T

0.4166251588471326 0.5834061446112599 0.6779781351247252 T T T

0.2498308049654341 0.7501592804122339 0.7353653012299191 T T T

0.9162835907518243 0.0837071505408176 0.2647012808527762 F F F

0.7494815904462442 0.2503221745916235 0.3219004831220502 F F F

0.9163199193766829 0.0834146889840000 0.4024800013573113 F F F

0.7491301334269238 0.2498588104495596 0.4597325076861054 F F F

0.9165943437574100 0.0833622099862907 0.5401753993825835 T T T

0.7498654963325251 0.2500353620989415 0.5975664933913336 T T T

0.9166256183254191 0.0834060430496280 0.6779779648349091 T T T

0.7498312644072200 0.2501591787844077 0.7353654114839259 T T T

0.9162826484454598 0.5837077031176321 0.2647013439451840 F F F

0.7494806481398726 0.7503227271684452 0.3219005462144580 F F F

0.9163189770703184 0.5834152415608216 0.4024800644497191 F F F

0.7491298567981914 0.7498575452086698 0.4597325707852775 F F F

0.9165940671286776 0.5833609447454009 0.5401754624817556 T T T

0.7498661286849284 0.7500359147287057 0.5975665564834003 T T T

0.9166246760190475 0.5834065956264496 0.6779780279273169 T T T

0.7498303221373490 0.7501597314274235 0.7353651940325108 T T T

Optimized 2x2x4 Supercell 25% Co Surface Doped β-Ni(OH)$_2$

Total Free Energy: -277.4713081eV

Ni Co H O

1.00000000000000

6.3506889969999998 -0.0001849620000000 0.0000076420000000

-3.1755045220000002 5.5010339200000002 0.0001355020000000

0.0000767550000000 0.0012980790000000 35.6450547760000021

Ni Co H O

15 1 32 32

Selective dynamics

Direct

0.0832709983956406 0.4169261037169747 0.2933282873326348 F F F

0.0830915718456211 0.4169862823127133 0.4311645180269679 F F F

0.0828454044765152 0.4165665810532033 0.5688644062610138 T T T

0.0822475428374787 0.4168921216349233 0.7068218309685932 T T T

0.0832716307480439 0.9169266563467389 0.2933283504247086 F F F

0.0830922041980244 0.9169868349424704 0.4311645811190417 F F F

0.0828565279963200 0.9168179993446444 0.5688501606621230 T T T

0.0823929023010237 0.9166436184882443 0.7068920309325861 T T T

0.5832720902263233 0.4169265547851069 0.2933281801348926 F F F

0.5830926636763039 0.4169867333808455 0.4311644108292256 F F F

0.5829236437345315 0.4167433631520296 0.5688729952349902 T T T

0.5832711479199588 0.9169271073619214 0.2933282432273003 F F F

0.5830923870475715 0.9169854681399485 0.4311644739283977 F F F

0.5830670473633717 0.9168184536810031 0.5688660444174829 T T T

0.5827445843601282 0.9169767671328088 0.7068027094586853 T T T

0.5817699905536102 0.4166816723300286 0.7068845664919294 T T T

0.4169075361928378 0.0839766857310451 0.2376707088324608 F F F

0.4160274018754180 0.0830134106967648 0.3754480293644065 F F F

0.2493265147581241 0.2500081263314300 0.3489253781823294 F F F

0.4155968654910822 0.0837680496513968 0.5130558947992938 T T T

0.2496389458473232 0.2501355808864005 0.4867644139537148 F F F

0.4135430303196443 0.0765840905282431 0.6508155649693776 T T T

0.2493228361713022 0.2502593630044672 0.6246696582164546 T T T

0.2384513699133564 0.2476359416880385 0.7629654321895032 T T T

0.4169081685452483 0.5839772383608093 0.2376707719245275 F F F

0.4160280342278284 0.5830139633265290 0.3754480924564731 F F F

0.2493271471105345 0.7500086789611871 0.3489254412743961 F F F

0.4155770782858283 0.5837340633610282 0.5130528720449661 T T T

0.2496395781997265 0.7501361335161647 0.4867644770457815 F F F

0.4130760214763072 0.5869735918370012 0.6507805206908017 T T T

0.2482015502501298 0.7505543711843146 0.6246562543261120 T T T

0.2486019763336103 0.7504673182710704 0.7625177344000491 T T T

0.9169086280235277 0.0839771367991773 0.2376706016347114 F F F

0.9160284937061078 0.0830138617648970 0.3754479221666571 F F F

0.7493276065888139 0.2500085773995622 0.3489252709845871 F F F

0.9155676688605681 0.0837394175696531 0.5130417605273649 T T T

0.7496400376780059 0.2501360319545327 0.4867643067559726 F F F

0.9150905927233737 0.0837050370238828 0.6509688878441864 T T T

0.7482793096294387 0.2508505722128120 0.6246897481523277 T T T

0.7509679078449096 0.2468370483958111 0.7626073514268299 T T T

0.9169076857171632 0.5839776893759918 0.2376706647271192 F F F

0.9160275513997433 0.5830144143417115 0.3754479852590649 F F F

0.7493266642824494 0.7500091299763767 0.3489253340769949 F F F

0.9155481234261060 0.5837090641872038 0.5130505205998119 T T T

0.7496397610492807 0.7501347667136429 0.4867643698551447 F F F

0.9233838619083770 0.5862890949824049 0.6506479972018795 T T T

0.7488064983587179 0.7496368280134007 0.6246785939945738 T T T

0.7501872153252478 0.7588571246407483 0.7626446813237777 T T T

0.4162824989211416 0.0837066994726783 0.2647013880505185 F F F

0.2494804986155543 0.2503217235234914 0.3219005903197925 F F F

0.4163188275459930 0.0834142379158678 0.4024801085550607 F F F

0.2491290415962339 0.2498583593814274 0.4597326148838476 F F F

0.4165733450845579 0.0833817778584205 0.5400764745383597 T T T

0.2497823060661872 0.2499494519120802 0.5976423477642214 T T T

0.4151325850881022 0.0809823967225825 0.6778265878987497 T T T

0.2428466275572561 0.2475133919190853 0.7359743103346190 T T T

0.4162831312735449 0.5837072521024425 0.2647014511425851 F F F

0.2494811309679577 0.7503222761532555 0.3219006534118662 F F F

0.4163194598984035 0.5834147905456319 0.4024801716471273 F F F

0.2491296739486444 0.7498589120111916 0.4597326779759143 F F F

0.4164795996315007 0.5833132503181844 0.5400726102997240 T T T

0.2499407535186222 0.7501081633925182 0.5976362382570883 T T T

0.4152599124389980 0.5847349825137655 0.6777971795989828 T T T

0.2496687880314852 0.7501974137262835 0.7355173558727017 T T T

0.9162835907518243 0.0837071505408176 0.2647012808527762 F F F

0.7494815904462442 0.2503221745916235 0.3219004831220502 F F F

0.9163199193766829 0.0834146889840000 0.4024800013573113 F F F

0.7491301334269238 0.2498588104495596 0.4597325076861054 F F F

0.9165905573157644 0.0834113186172445 0.5400606567723898 T T T

0.7497183468499600 0.2499426232098259 0.5976686117276273 T T T

0.9164278858067973 0.0832278864171911 0.6779849791501675 T T T

0.7499397076438257 0.2495446961432677 0.7356041565914424 T T T

0.9162826484454598 0.5837077031176321 0.2647013439451840 F F F

0.7494806481398726 0.7503227271684452 0.3219005462144580 F F F

0.9163189770703184 0.5834152415608216 0.4024800644497191 F F F

0.7491298567981914 0.7498575452086698 0.4597325707852775 F F F

0.9165408866002451 0.5832955249431464 0.5400727837019943 T T T

0.7498073963033534 0.7501231497479850 0.5976484749611970 T T T

0.9198371042476694 0.5851609963843174 0.6776514675573750 T T T

0.7503954232584604 0.7525337806081609 0.7356575115519703 T T T

Optimized 2x2x4 Supercell 50% Co Surface Doped β-Ni(OH)$_2$

Total Free Energy: -279.736962eV

Ni Co H O

1.00000000000000

6.3506889969999998 -0.0001849620000000 0.0000076420000000

-3.1755045220000002 5.5010339200000002 0.0001355020000000

0.0000767550000000 0.0012980790000000 35.6450547760000021

Ni Co H O

14 2 32 32

Selective dynamics

Direct

0.0832709983956406 0.4169261037169747 0.2933282873326348 F F F

0.0830915718456211 0.4169862823127133 0.4311645180269679 F F F

0.0830269172803426 0.4165611421095505 0.5688284966332091 T T T

0.0816695918454755 0.4171502272866903 0.7068566175455970 T T T

0.0832716307480439 0.9169266563467389 0.2933283504247086 F F F

0.0830922041980244 0.9169868349424704 0.4311645811190417 F F F

0.0829164507868754 0.9167016562835357 0.5688641882827881 T T T

0.5832720902263233 0.4169265547851069 0.2933281801348926 F F F

0.5830926636763039 0.4169867333808455 0.4311644108292256 F F F

0.5829169102651548 0.4167015547219037 0.5688640179929720 T T T

0.5832711479199588 0.9169271073619214 0.2933282432273003 F F F

0.5830923870475715 0.9169854681399485 0.4311644739283977 F F F

0.5830270668046680 0.9165621457545043 0.5688284525278675 T T T

0.5816713160285687 0.9171512309845866 0.7068565734399215 T T T

0.0818722394013136 0.9175107040197403 0.7069203626743459 T T T

0.5818726988430996 0.4175106023919142 0.7069204729283598 T T T

0.4169075361928378 0.0839766857310451 0.2376707088324608 F F F

0.4160274018754180 0.0830134106967648 0.3754480293644065 F F F

0.2493265147581241 0.2500081263314300 0.3489253781823294 F F F

0.4158051839601100 0.0836808078780891 0.5130239130902510 T T T

0.2496389458473232 0.2501355808864005 0.4867644139537148 F F F

0.4173430315286453 0.0827540113940586 0.6506298206882164 T T T

0.2489255108183599 0.2503811424157121 0.6246803185040406 T T T

0.2460332989818426 0.2514591061881859 0.7629999229209687 T T T

0.4169081685452483 0.5839772383608093 0.2376707719245275 F F F

0.4160280342278284 0.5830139633265290 0.3754480924564731 F F F

0.2493271471105345 0.7500086789611871 0.3489254412743961 F F F

0.4158701844410686 0.5836431876991739 0.5130253790327615 T T T

0.2496395781997265 0.7501361335161647 0.4867644770457815 F F F

0.4109082489174014 0.5887695716393608 0.6506674551668965 T T T

0.2486847816258333 0.7505162197411437 0.6246267972659467 T T T

0.2528676168224564 0.7447484718229305 0.7627929687173705 T T T

0.9169086280235277 0.0839771367991773 0.2376706016347114 F F F

0.9160284937061078 0.0830138617648970 0.3754479221666571 F F F

0.7493276065888139 0.2500085773995622 0.3489252709845871 F F F

0.9158706439193480 0.0836430861375419 0.5130252087429454 T T T

0.7496400376780059 0.2501360319545327 0.4867643067559726 F F F

0.9109071337369130 0.0887694700247863 0.6506672848774215 T T T

0.7486836664453449 0.2505161181265692 0.6246266269764718 T T T

0.7528680762642423 0.2447483701950972 0.7627930789713773 T T T

0.9169076857171632 0.5839776893759918 0.2376706647271192 F F F

0.9160275513997433 0.5830144143417115 0.3754479852590649 F F F

0.7493266642824494 0.7500091299763767 0.3489253340769949 F F F

0.9158053334844283 0.5836818115230358 0.5130238689849165 T T T

0.7496397610492807 0.7501347667136429 0.4867643698551447 F F F

0.9173431810529635 0.5827550150390053 0.6506297765828819 T T T

0.7489247513615496 0.7503803281900048 0.6246802744058115 T T T

0.7460325394885317 0.7514582918962773 0.7630001593665625 T T T

0.4162824989211416 0.0837066994726783 0.2647013880505185 F F F

0.2494804986155543 0.2503217235234914 0.3219005903197925 F F F

0.4163188275459930 0.0834142379158678 0.4024801085550607 F F F

0.2491290415962339 0.2498583593814274 0.4597326148838476 F F F

0.4165474245019922 0.0833708769635209 0.5400467369399351 T T T

0.2498009209610785 0.2500276183379384 0.5976479583395857 T T T

0.4165928394047711 0.0832256967062577 0.6776731215858121 T T T

0.2476835893586582 0.2516255071869651 0.7359813072613406 T T T

0.4162831312735449 0.5837072521024425 0.2647014511425851 F F F

0.2494811309679577 0.7503222761532555 0.3219006534118662 F F F

0.4163194598984035 0.5834147905456319 0.4024801716471273 F F F

0.2491296739486444 0.7498589120111916 0.4597326779759143 F F F

0.4165677195011597 0.5833005342260051 0.5400479224725885 T T T

0.2498431526950213 0.7499791019379032 0.5976003291590644 T T T

0.4123003248204995 0.5863109750556177 0.6776925313958486 T T T

0.2511361098516502 0.7483704680992105 0.7357956619772636 T T T

0.9162835907518243 0.0837071505408176 0.2647012808527762 F F F

0.7494815904462442 0.2503221745916235 0.3219004831220502 F F F

0.9163199193766829 0.0834146889840000 0.4024800013573113 F F F

0.7491301334269238 0.2498588104495596 0.4597325076861054 F F F

0.9165681789429456 0.0833004325981790 0.5400480327266024 T T T

0.7498436121368073 0.2499790003100699 0.5976004394130712 T T T

0.9123007842987860 0.0863108734939857 0.6776923611060326 T T T

0.7511365692934362 0.2483703664713843 0.7357957722312705 T T T

0.9162826484454598 0.5837077031176321 0.2647013439451840 F F F

0.7494806481398726 0.7503227271684452 0.3219005462144580 F F F

0.9163189770703184 0.5834152415608216 0.4024800644497191 F F F

0.7491298567981914 0.7498575452086698 0.4597325707852775 F F F

0.9165466650451748 0.5833700627378207 0.5400466928417060 T T T

0.7498017361630360 0.7500268041651807 0.5976479142410156 T T T

0.9165929889290965 0.5832267003512115 0.6776730774804776 T T T

0.7476837388829836 0.7516265108319189 0.7359812631560061 T T T

Optimized 2x2x4 Supercell 75% Co Surface Doped β-Ni(OH)$_2$

Total Free Energy: -282.5324345eV

Ni Co H O

1.00000000000000

6.3506889969999998 -0.0001849620000000 0.0000076420000000

-3.1755045220000002 5.5010339200000002 0.0001355020000000

0.0000767550000000 0.0012980790000000 35.6450547760000021

Ni Co H O

13 3 32 32

Selective dynamics

Direct

0.0832709983956406 0.4169261037169747 0.2933282873326348 F F F

0.0830915718456211 0.4169862823127133 0.4311645180269679 F F F

0.0830551702418276 0.4168065878157279 0.5686744771343228 T T T

0.0815362845762380 0.4173937843150810 0.7069797753873743 T T T

0.0832716307480439 0.9169266563467389 0.2933283504247086 F F F

0.0830922041980244 0.9169868349424704 0.4311645811190417 F F F

0.0828573650285165 0.9167598392142224 0.5688047127834324 T T T

0.5832720902263233 0.4169265547851069 0.2933281801348926 F F F

0.5830926636763039 0.4169867333808455 0.4311644108292256 F F F

0.5831071601420419 0.4169560699194221 0.5688166050782826 T T T

0.5832711479199588 0.9169271073619214 0.2933282432273003 F F F

0.5830923870475715 0.9169854681399485 0.4311644739283977 F F F

0.5830746719731934 0.9167675693759634 0.5688026417048846 T T T

0.0802899643470454 0.9170325061129958 0.7071439582597279 T T T

0.5810163984001946 0.4169979013855780 0.7070955344075784 T T T

0.5808189540735782 0.9172856756227432 0.7070551981394999 T T T

0.4169075361928378 0.0839766857310451 0.2376707088324608 F F F

0.4160274018754180 0.0830134106967648 0.3754480293644065 F F F

0.2493265147581241 0.2500081263314300 0.3489253781823294 F F F

0.4154097518371813 0.0836426198080602 0.5130244744078496 T T T

0.2496389458473232 0.2501355808864005 0.4867644139537148 F F F

0.4165237946663680 0.0875712847859234 0.6505251597047206 T T T

0.2480278885768072 0.2507210790488230 0.6245501450695627 T T T

0.2418960729366475 0.2516152344012852 0.7632835530212603 T T T

0.4169081685452483 0.5839772383608093 0.2376707719245275 F F F

0.4160280342278284 0.5830139633265290 0.3754480924564731 F F F

0.2493271471105345 0.7500086789611871 0.3489254412743961 F F F

0.4155860993231144 0.5836922698260025 0.5129830167895477 T T T

0.2496395781997265 0.7501361335161647 0.4867644770457815 F F F

0.4096102976531952 0.5834687168809012 0.6506225885840138 T T T

0.2483424201729250 0.7500708609744180 0.6245269254307360 T T T

0.2419434899419670 0.7388799041330287 0.7636938195895766 T T T

0.9169086280235277 0.0839771367991773 0.2376706016347114 F F F

0.9160284937061078 0.0830138617648970 0.3754479221666571 F F F

0.7493276065888139 0.2500085773995622 0.3489252709845871 F F F

0.9152851802886985 0.0834358432076527 0.5129806031881472 T T T

0.7496400376780059 0.2501360319545327 0.4867643067559726 F F F

0.9193553156354000 0.0940416193047469 0.6501207636539235 T T T

0.7494139640253508 0.2507579338173613 0.6245486347173781 T T T

0.7542997224188781 0.2519415455755691 0.7630727535133985 T T T

0.9169076857171632 0.5839776893759918 0.2376706647271192 F F F

0.9160275513997433 0.5830144143417115 0.3754479852590649 F F F

0.7493266642824494 0.7500091299763767 0.3489253340769949 F F F

0.9152840109727904 0.5837036160196121 0.5129902037548248 T T T

0.7496397610492807 0.7501347667136429 0.4867643698551447 F F F

0.9194762829010728 0.5839821177014102 0.6506769028233776 T T T

0.7487990652437517 0.7509256908867172 0.6246171499990325 T T T

0.7446666443992740 0.7466608389292517 0.7635385414962386 T T T

0.4162824989211416 0.0837066994726783 0.2647013880505185 F F F

0.2494804986155543 0.2503217235234914 0.3219005903197925 F F F

0.4163188275459930 0.0834142379158678 0.4024801085550607 F F F

0.2491290415962339 0.2498583593814274 0.4597326148838476 F F F

0.4165843075138085 0.0833690606945581 0.5400453342198048 T T T

0.2498597636412896 0.2500949091306026 0.5975262020512275 T T T

0.4158227253856523 0.0844945463669831 0.6775749265888180 T T T

0.2428164543577509 0.2499219551477694 0.7362873880935297 T T T

0.4162831312735449 0.5837072521024425 0.2647014511425851 F F F

0.2494811309679577 0.7503222761532555 0.3219006534118662 F F F

0.4163194598984035 0.5834147905456319 0.4024801716471273 F F F

0.2491296739486444 0.7498589120111916 0.4597326779759143 F F F

0.4165612102923788 0.5833914359417491 0.5400058405547199 T T T

0.2497667234703584 0.7499427657362361 0.5975021389749173 T T T

0.4119467174821168 0.5830152298694316 0.6776468153567521 T T T

0.2443299421021479 0.7439290373164908 0.7367220360295121 T T T

0.9162835907518243 0.0837071505408176 0.2647012808527762 F F F

0.7494815904462442 0.2503221745916235 0.3219004831220502 F F F

0.9163199193766829 0.0834146889840000 0.4024800013573113 F F F

0.7491301334269238 0.2498588104495596 0.4597325076861054 F F F

0.9164807469546901 0.0833586102727750 0.5400067925819485 T T T

0.7499679966836865 0.2501080890128122 0.5975246920630042 T T T

0.9176067341036145 0.0903122513991619 0.6771267684068647 T T T

0.7521856595326071 0.2516588098610058 0.7360695702785307 T T T

0.9162826484454598 0.5837077031176321 0.2647013439451840 F F F

0.7494806481398726 0.7503227271684452 0.3219005462144580 F F F

0.9163189770703184 0.5834152415608216 0.4024800644497191 F F F

0.7491298567981914 0.7498575452086698 0.4597325707852775 F F F

0.9164561335049655 0.5833936998238514 0.5400119053369892 T T T

0.7498425707006788 0.7500486345804589 0.5975845112448823 T T T

0.9180076586776096 0.5839302509072368 0.6776778437477091 T T T

0.7456464502645659 0.7483614723699219 0.7365286170066483 T T T

Optimized 2x2x4 Supercell 100% Co Surface Doped β-Ni(OH)$_2$

Total Free Energy: -285.0990895eV

Ni H O Co

1.00000000000000

6.3506889969999998 -0.0001849620000000 0.0000076420000000

-3.1755045220000002 5.5010339200000002 0.0001355020000000

0.0000767550000000 0.0012980790000000 35.6450547760000021

Ni H O Co

12 32 32 4

Selective dynamics

Direct

0.0832709983956406 0.4169261037169747 0.2933282873326348 F F F

0.0830915718456211 0.4169862823127133 0.4311645180269679 F F F

0.0829016238498284 0.4168301710808606 0.5688587943704491 T T T

0.0832716307480439 0.9169266563467389 0.2933283504247086 F F F

0.0830922041980244 0.9169868349424704 0.4311645811190417 F F F

0.0829022562387252 0.9168307237768261 0.5688585769186929 T T T

0.5832720902263233 0.4169265547851069 0.2933281801348926 F F F

0.5830926636763039 0.4169867333808455 0.4311644108292256 F F F

0.5829027156805182 0.4168306221489928 0.5688586871727068 T T T

0.5832711479199588 0.9169271073619214 0.2933282432273003 F F F

0.5830923870475715 0.9169854681399485 0.4311644739283977 F F F

0.5829033480329215 0.9168311747787570 0.5688587502647735 T T T

0.4169075361928378 0.0839766857310451 0.2376707088324608 F F F

0.4160274018754180 0.0830134106967648 0.3754480293644065 F F F

0.2493265147581241 0.2500081263314300 0.3489253781823294 F F F

0.4163441406575714 0.0838989615808075 0.5130460751075674 T T T

0.2496389458473232 0.2501355808864005 0.4867644139537148 F F F

0.4152273175563153 0.0847737522483740 0.6498176390912818 T T T

0.2490442089683995 0.2501430115392225 0.6246710614376170 T T T

0.2496399300753325 0.2487523345334921 0.7635467123517472 T T T

0.4169081685452483 0.5839772383608093 0.2376707719245275 F F F

0.4160280342278284 0.5830139633265290 0.3754480924564731 F F F

0.2493271471105345 0.7500086789611871 0.3489254412743961 F F F

0.4163447730099819 0.5838995142105716 0.5130461381996341 T T T

0.2496395781997265 0.7501361335161647 0.4867644770457815 F F F

0.4152254662688151 0.5847724869545345 0.6498177021907949 T T T

0.2490448413572963 0.7501435642351879 0.6246708439858608 T T T

0.2496405624277358 0.7487528871632563 0.7635467754438210 T T T

0.9169086280235277 0.0839771367991773 0.2376706016347114 F F F

0.9160284937061078 0.0830138617648970 0.3754479221666571 F F F

0.7493276065888139 0.2500085773995622 0.3489252709845871 F F F

0.9163452324517678 0.0838994125827455 0.5130462484536480 T T T

0.7496400376780059 0.2501360319545327 0.4867643067559726 F F F

0.9152259257106081 0.0847723853267013 0.6498178124448089 T T T

0.7490453007990823 0.2501434626073546 0.6246709542398676 T T T

0.7496394472472474 0.2487527855486817 0.7635466051543460 T T T

0.9169076857171632 0.5839776893759918 0.2376706647271192 F F F

0.9160275513997433 0.5830144143417115 0.3754479852590649 F F F

0.7493266642824494 0.7500091299763767 0.3489253340769949 F F F

0.9163442901818968 0.5838999652257613 0.5130460310022258 T T T

0.7496397610492807 0.7501347667136429 0.4867643698551447 F F F

0.9152265580995049 0.5847729380226667 0.6498175949930527 T T T

0.7490443584927178 0.7501440151841692 0.6246710173322754 T T T

0.7496400795996507 0.7487533381784388 0.7635466682464127 T T T

0.4162824989211416 0.0837066994726783 0.2647013880505185 F F F

0.2494804986155543 0.2503217235234914 0.3219005903197925 F F F

0.4163188275459930 0.0834142379158678 0.4024801085550607 F F F

0.2491290415962339 0.2498583593814274 0.4597326148838476 F F F

0.4164936550414993 0.0834145008022418 0.5400573974509726 T T T

0.2498043769391458 0.2500439774261736 0.5976546913284508 T T T

0.4146736560833020 0.0854526814476770 0.6768460703362109 T T T

0.2513612725133783 0.2483333894395443 0.7365449315315189 T T T

0.4162831312735449 0.5837072521024425 0.2647014511425851 F F F

0.2494811309679577 0.7503222761532555 0.3219006534118662 F F F

0.4163194598984035 0.5834147905456319 0.4024801716471273 F F F

0.2491296739486444 0.7498589120111916 0.4597326779759143 F F F

0.4164942873939026 0.5834150534320059 0.5400574605430393 T T T

0.2498050093280426 0.7500445301221390 0.5976544738766947 T T T

0.4146718047958089 0.5854514161538376 0.6768461334357241 T T T

0.2513619048657887 0.7483339420693085 0.7365449946235927 T T T

0.9162835907518243 0.0837071505408176 0.2647012808527762 F F F

0.7494815904462442 0.2503221745916235 0.3219004831220502 F F F

0.9163199193766829 0.0834146889840000 0.4024800013573113 F F F

0.7491301334269238 0.2498588104495596 0.4597325076861054 F F F

0.9164931722134142 0.0834149518174314 0.5400572902535643 T T T

0.7498054687698286 0.2500444284943057 0.5976545841307015 T T T

0.9146722642740883 0.0854513145922127 0.6768459631459152 T T T

0.7513607896852932 0.2483338404547339 0.7365448243341106 T T T

0.9162826484454598 0.5837077031176321 0.2647013439451840 F F F

0.7494806481398726 0.7503227271684452 0.3219005462144580 F F F

0.9163189770703184 0.5834152415608216 0.4024800644497191 F F F

0.7491298567981914 0.7498575452086698 0.4597325707852775 F F F

0.9164938045658175 0.5834155044471885 0.5400573533456310 T T T

0.7498061011222319 0.7500449811240699 0.5976546472227753 T T T

0.9146728966264916 0.5854518672219768 0.6768460262379818 T T T

0.7513614220377036 0.7483343930844910 0.7365448874261844 T T T

0.0829079456278805 0.4169248752886219 0.7067780658658336 T T T

0.0829070033580095 0.9169254279316377 0.7067778484144185 T T T

0.5829074627997954 0.4169253263038115 0.7067779586684253 T T T

0.5829080951521988 0.9169258789335686 0.7067780217604991 T T T